

Structural health stability and stress monitoring by ultrasound

Von der Fakultät für Physik und Geowissenschaften
der Universität Leipzig
genehmigte

DISSERTATION

zur Erlangung des akademischen Grades
Doctor rerum naturalium,
Dr. rer. nat.,

vorgelegt von

Herrn Khurram Shahzad Tarar, M.Sc.,
geboren am 15 Dezember 1977 in M. B. Din (Punjab, Pakistan).

Gutachter: Prof. Dr. Jan Meijer
Prof. Dr. Muhammad Maqbool

Tag der Verleihung: 23 Oktober 2017

ACKNOWLEDGEMENTS

Praise be to Allah (God, Almighty); Most Gracious, Most Merciful.

This PhD dissertation arose during my studentship and employment as a scientific researcher and co-worker at the faculty of Physics and Geosciences, University of Leipzig, Germany.

Professor Dr. Wolfgang Grill gave me the opportunity to work intensely on the subject of this dissertation. I am grateful to him and his research group for the technical support and scientific freedom which made this research possible.

Special thanks are extended to Professor Dr. T. Kundu, Dr. R. Wannemacher, Dr. E. Twerdowski and Dr. Mietek Pluta for their active support, fruitful discussions and kind help during my research period.

Thanks to all of my colleagues, Mr. U. Amjad, Mr. D. Jha, Mr. A. Shelke, Ms. K. Hahn, Mr. H. Klinghammer, Mr. R. Meier and Mr. Essam for their constant support.

I cannot forget the constant moral and emotional support from my parents, family and specially my sisters.

Lastly, I wish to thank my wife and son for their constant love for me.

Khurram Shahzad Tarar

RESEARCH FUNDING ACKNOWLEDGEMENT

The research presented within this dissertation was partially funded by the European Union under the 7th framework program within AISHA II (Aircraft Integrated Structural Health Assessment-II, Grant agreement no. 212912) for which the author is thoroughly grateful.

Khurram Shahzad Tarar

**DEDICATED TO MY PARENTS
FOR THEIR ENDLESS LOVE AND SUPPORT
DURING MY WHOLE LIFE**

ABSTRACT

The goal of this dissertation is to demonstrate the established ultrasound based monitoring schemes for solid structures with the developed theoretical modeling which can predict the same physical behaviors that were later found in the experimental results. It is mainly focused on the stress effects for isotropic solid media analyzed by two fundamental modes of acoustic waves. The subject is also covered by an analytical comparison of microscopic and macroscopic approaches for the stress dependence of the time-of-flight of bulk and guided acoustic waves propagating in solid materials.

The theoretical description of these effects is studied by developing mass spring lattice dynamic models where corrections have been done accordingly for different modes, including anharmonicity, normally present in the (actual) material. These models are helpful in understanding the different phenomena of wave propagation with stress effects and their results are later compared with the experimentally achieved results. The models are initially drawn for ideal (material) conditions and are later amended with anharmonicity parameters to represent the generalized propagation behaviors of acoustic waves.

The dissertation further includes two signal processing and detection schemes, and an ultrasonic application used for structural health monitoring (SHM). The developed pulse compression scheme has been effectively demonstrated for data and signal processing of ultrasonic waves propagating through solid materials. The developed detection scheme has been applied and demonstrated successfully for high sensitivity of flaw detection in the aero plane slat tracks. The ultrasonic application is employed for ablation monitoring of aluminum plates by mode selective excitation and detection method and achieved result is the determination of appropriate mode and frequency range of acoustic waves for optimum sensitivity of plate thickness.

LIST OF IMPORTANT SYMBOLS AND ABBREVIATIONS

Most of the symbols and abbreviations are defined in the text in each chapter distinctively. Here in the following a general tabular overview is presented.

Symbols and their abbreviations	Definition	Units
SHM	Structural health monitoring	N/A
TOF / t_{of}	Time-of-flight	seconds
MSLD	Mass spring lattice dynamic	N/A
NDT	Non-destructive testing	N/A
NDE	Non-destructive evaluation	N/A
MHz	Frequency	Mega hertz
kHz	Frequency	Kilo hertz
$V_{(ph)}$	Phase velocity	Lattice unit per TOF, Meter per second
$V_{(gr)}$	Group velocity	Lattice unit per TOF, Meter per second
m	Mass	kg
A0	Lowest order (frequency) anti-symmetric acoustic wave mode	N/A
S0	Lowest order (frequency) symmetric acoustic wave mode	N/A
G	Torsional coefficient	N/A
α	Angle of twist	Radian, degree
y	Vertical displacement	Lattice distance, meter
ω	Angular frequency	N/A
k	Wave number	N/A
L-mode	Longitudinally polarized mode	N/A
T-mode	Transversely polarized mode	N/A
Al	Aluminum	N/A

S	Cross-sectional area	N/A
h	Thickness	Meter ²
I	Moment of inertia	N/A
P	Extensional pulling force	N/A
E _{CF}	Elastic coupling function	nsm ⁻¹ MPa ⁻¹
MPa	Pressure	Mega Pascal
FFT	Fast Fourier Transformation	N/A
us	Time	Micro seconds
mm	Length	Milli meter
ns	Time	Neno seconds
ps	Time	Peco seconds
ΔTOF	Differential time-of-flight	Seconds
PZT	Lead Zirconate Titanate transducer	N/A
SAW	Surface acoustic waves	N/A
STFT	Short time Fourier transformation	N/A
AISHA-II	Aircraft Integrated Structural Health Assessment-II	N/A

TABLE OF CONTENTS

1. Introduction	1
1.1 Motivation	1
1.2 Objectives	2
1.3 Organization of the dissertation	3
1.4 References	4
2. Analytical comparison of microscopic and macroscopic approaches for the stress dependence of the time-of-flight of free (bulk) and guided acoustic waves in solid materials	5
2.1 Microscopic approach	5
2.2 Macroscopic approach	7
2.3 Stress dependence of TOF in macroscopic approach	8
2.4 Stress dependence of TOF in microscopic approach	10
2.5 Difference in the stress dependence of TOF between micro- and macroscopic approaches	11
2.6 Summary	13
2.7 References	13
3. Developed theory for bulk acoustic waves	15
3.1 L-mode vibrations	15
3.1.1 Lattice dynamic modeling	16
3.1.2 Harmonic vibrations	17
3.1.3 Generalized vibrations	20
3.2 T-mode vibrations	24
3.2.1 Lattice dynamic modeling	24
3.2.2 Harmonic vibrations	26
3.2.3 Generalized vibrations	29
3.3 Combined (L + T)-mode vibrations	34
3.3.1 Lattice dynamic modeling	34
3.3.2 Harmonic vibrations	36
3.3.3 Generalized vibrations	36
3.4 Comparison of L-mode and T-mode vibrations	41

3.5	Summary	42
3.6	References	42
4.	Developed theory for guided acoustic waves	44
4.1	Derivation of the model	44
4.1.1	Lattice dynamic modeling	44
4.1.2	Sideways force and dynamics	45
4.1.3	Perpendicular force and dynamics	45
4.1.4	Dispersion relation	46
4.1.5	Respective physical parameters derived from the model	46
4.1.6	Lennard-Jones potential and respective coefficients for aluminum	47
4.2	Comparison of the frequency dependent physical parameters between continuum and discrete models	48
4.2.1	Velocity	50
4.2.2	Time-of-flight (TOF)	53
4.2.3	Momentum	55
4.2.4	Energy	57
4.2.5	Elasticity	60
4.2.6	Viscoelasticity	61
4.2.7	Resonance	62
4.2.8	Impedance	64
4.3	Analytical treatment of modeling results (in comparison with the experimental results)	66
4.3.1	Zero crossing (i.e. frequency value at zero E_{CF})	68
4.3.2	Horizontal asymptote (i.e. elastic coupling function for $f \rightarrow \infty$)	69
4.3.3	Vertical asymptote (i.e. elastic coupling function for $f \rightarrow 0$)	70
4.4	Conclusive statement of the analytical treatment	71
4.5	Summary	72
4.6	References	72
5.	Signal processing scheme (pulse compression)	75
5.1	The compression scheme	75
5.2	Example with an artificial chirped signal	76
5.3	Instrumentation	78
5.4	Application	78

5.5	Results	81
5.6	Summary	83
5.7	References	84
6.	Flaw detection scheme (for aero plane slat tracks)	85
6.1	The detection scheme	85
6.2	Improved EMAT design and instrumentation	86
6.3	Application	89
6.4	Results	91
6.5	Comparison with literature	92
6.6	Summary	93
6.7	References	94
7.	Ultrasonic application (for ablation monitoring of aluminum plate)	95
7.1	The ablation scheme	95
7.2	Instrumentation	96
7.3	Application	99
7.4	Results	99
7.5	Comparison with literature	106
7.6	Summary	106
7.7	References	107
8.	Conclusions	109
8.1	Structural health stability and stress monitoring by ultrasound	109
8.2	Summary of the performed work	109
8.3	Contributions to the advancement of the state of the art	111
9.	Appendices	112
(Chapter 2)	Appendix 2.1	112
(Chapter 2)	Appendix 2.2	112
(Chapter 2)	Appendix 2.3	113
(Chapter 3)	Appendix 3.1	114
(Chapter 3)	Appendix 3.2	115
(Chapter 3)	Appendix 3.3	117

(Chapter 3)	Appendix 3.4	118
(Chapter 4)	Appendix 4.1	119
(Chapter 4)	Appendix 4.2	120
(Chapter 4)	Appendix 4.3	121
(Chapter 4)	Appendix 4.4	122
(Chapter 4)	Appendix 4.5	123
(Chapter 4)	Appendix 4.6	125
(Chapter 4)	Appendix 4.7	127
(Chapter 4)	Appendix 4.8	130
(Chapter 4)	Appendix 4.9	131
(Chapter 4)	Appendix 4.10	135
10.	Miscellaneous	138
10	Publications and results used in the dissertation	138
10	Author's statement of independence	139
10	Author's Curriculum Vitae	140

1. Introduction:

The introduction chapter comprises of the following parts:

1.1 Motivation

Monitoring of the stability of manufactured solid structures of medium and large size over the entire lifetime is currently gaining an increasing attention. This is especially important for parts where degradation would lead to safety hazards. In the past and still today respective safety inspections are in many cases even regulated by law and are performed at certain intervals of time with the aid of external components for monitoring.

Particularly in aerospace and civil engineering, failures of the primary structure may put human life at risk, as numerous aircraft and bridge accidents have shown dramatic way in the past. For example the two aircraft crashes of the Comet in 1954 due to metal fatigue and damage tolerance design faults [1], the crash of the Aloha Airlines Boeing 737-200 in 1988, which was also caused by metal fatigue exacerbated by crevice corrosion (the plane operated in a salt water environment), the more recent crash of the China Airlines Boeing 747-200B in 2002 (also the result of metal fatigue, in that case due to inadequate maintenance after a previous incident in 1980). All of these accidents have demonstrated the very importance of inspection and maintenance as a human safety issue.

Many different inspection and nondestructive testing (NDT) techniques are available and applied in the aerospace industry for many decades, most of them being developed in the 1960s. These conventional NDT techniques range from basic visual inspection, ultrasonic inspection and thermography to radiography, shearography [2] and eddy-current. Most of the conventional NDT- techniques are time- consuming processes that require meticulous scans over large areas of the structure. Moreover, the results of such inspections and their reliability are often strongly influenced by the human factor (e.g. the experience and attention of the inspector). Despite all the accidents, the economic factor which is related to high maintenance and inspection costs but also to time the structure (aircraft) is out of service, represents a significant crucial factor for the end-user who has to decrease his direct operational costs. For commercial and military aircraft, it is estimated that up to 27% of the average life cycle costs are related to inspection and repair [3].

Motivated by these aspects, the last two decades has shown a range of novel NDT techniques [4] for which the term “Structural Health Monitoring” (SHM) has been introduced. The main difference between SHM and the conventional NDT techniques is that SHM utilizes (permanently) integrated sensors which provides a continuous or on demand information about the state at critical high-stress locations of safety-critical structures. The potential of SHM arose from a number of elements such as: reduced inspection and maintenance costs, improved performance and safety, reduced out of service times, and last but not least, reduction of the influence of the human factor. The concept of Structural Health Monitoring can be compared to that of the human nervous system which also benefits from many different “sensors”, which transmit signals (e.g.

pain) to the main “computer”, the brain. The main components of an SHM-system can be classified into the following categories:

- Sensors/actuators
- Data acquisition
- Signal processing
- Materials and structures
- Computation

SHM is a multidisciplinary field in which researchers and engineers from different disciplines such as materials science, physics, computer science, mechanical engineering, etc. have to contribute and be involved. The development of structural health monitoring systems covered the following purposes:

- Load history monitoring
- Impact detection and localization
- Damage identification / quantification

For the identification of damages, different SHM approaches have been proposed in the past which can be classified as either global or local. Global approaches are based upon vibration measurements of the structure in the lower frequency range (< 50 kHz), for which active excitation is not required. Such global methods are typically only sensitive to fairly large levels of damages and may be used therefore to monitor large areas for locating suspect positions that may then be covered in detail by a further inspection technique. Since last few years, local diagnostic methods have generated considerable interest in the SHM community. These methods typically consider high frequencies; mainly within the range of 10 kHz to 1 MHz. In this context the most widely discussed approach is to utilize ultrasonic Lamb waves which interact with damages. The development of small, inexpensive and lightweight piezoelectric elements which can be utilized both as actuators and as sensors is a further key point in the development of Lamb wave based SHM techniques.

The dissertation is based on the development of theoretical description of bulk and guided acoustic waves propagation through solid isotropic media with and without stressed conditions. The modeling based theory has been developed with the aid of lattice dynamics, a favorite approach used within solid state physics. The physics has been used here as an explaining tool of the physical phenomena going on within the solid structures during wave propagations. Also presented and discussed are the ultrasonic signal processing and detection schemes and their applications.

1.2 Objectives

The main objective of this dissertation is to make a contribution to enhance the scientific understanding of acoustic wave's propagation phenomenon through isotropic solids under pre-defined stressed conditions. The study has increasingly gained its interest due to human safety and the inter-field knowledge of physics and engineering.

As part of physics, the main portion of this research is dedicated to develop theoretical models for the prediction of acoustic wave's behavior during propagation through solid

media under defined conditions (stressed, non-stressed). The developed models are demonstrated by dispersion relations, and their respective acousto-elastic coefficients are compared to the experimental results. Based on this approach, further objectives of this research are to develop and demonstrate ultrasonic applications. The existing and new signal processing and detection schemes are used here to demonstrate the determination and prediction of remaining health and stability of the solid structures.

1.3 Organization of the dissertation

After the introduction part in chapter 1, chapter 2 provides a brief analytical comparison of microscopic (discrete model) and macroscopic (continuum model) approaches for the stress dependence of the TOF of bulk and guided acoustic waves in solid materials.

Chapter 3 provides a modeling theory for two fundamental lowest A0 and S0 modes of bulk acoustic waves and their reaction on time-of-flight upon the application of extensional stress. The chapter can be divided into three major parts with the theory consisting of mass-spring modeling treatment for longitudinal and transversal polarized (resembling symmetric and anti-symmetric) modes each, and a unified modeling treatment for longitudinally and transversely polarized modes, showing their resultant effects on TOF of propagating acoustic waves due to lengthwise stress.

The chapter 4 presents a further developed shape of theoretical modeling (from the previous one) to demonstrate the effects of extensional stress on TOF for the lowest order fundamental (S0 and A0) modes for guided acoustic waves. This chapter can be divided into three major parts where the first part consists of description of theoretical model, second part with the model derived physical parameters and their respective comparison to a continuum model, and the third part consists of analytical treatment of theoretical modeling results in comparison with experimental results.

In chapter 5, a pulse compression scheme for the determination of time-of-flight of ultrasound is presented and discussed. The results of developed scheme are compared with the traditional correlation scheme. The chapter generally consists of the scheme idea, scheme application, and a comparison with correlation scheme.

In chapter 6, a movable EMAT based flaw detection scheme is developed. The specific wedge shaped design of EMAT is developed and fabricated with permendur alloy material to enhance its capability of flaw detection. The scanning results of DC9 (aero plane) slat track with decreasing magnitude of flaws are presented in 2D and 3D (waterfall representation) graphs. The conducted investigation is a development part of online structural health assessment technology for slat tracks. The chapter also consists of a comparative study of the presented scheme with the literature.

In chapter 7, an ablation monitoring investigation of aluminum plate is presented based on the Lamb wave mode selective excitation and detection. Results are presented in the form of suitable mode and frequency range. In addition the relevance of theoretically and experimentally derived dispersion graphs and TOF assures the reliability of the given results. The conducted investigation is also a development part of online structural health assessment technology for wing and respective surface parts of aero

planes. The chapter also consists of a comparative study of the presented scheme with the literature.

Chapter 8 summarizes the main results of these above mentioned chapters and makes a final conclusion of this research.

1.4 References

- [1] Wikipedia: http://en.wikipedia.org/wiki/List_of_aircraft_structural_failures
- [2] Y. Y. Hung, "Shearography: A new optical method for strain measurement and non-destructive testing", *Optical Engineering* 21, pp. 391–395, (1982)
- [3] S. R. Hall, T. J. Conquest, "The total data initiative-structural health monitoring: the next generation", *Proc. of the USAF ASIP*, (1999)
- [4] H. Sohn, C. Farrar, "A Review of Structural Health Monitoring Literature: 1996-2001", *Los Alamos National Laboratory Report: LA-13976-MS*, (2003)

2. Analytical comparison of microscopic and macroscopic approaches for the stress dependence of the time-of-flight of free (bulk) and guided acoustic waves in solid materials

To explain the actual expected stress dependence of the time-of-flight (TOF) for acoustic waves, it is suitable to consider two basic models. This is demonstrated here for a microscopic model approach, the linear chain, generally employed for lattice dynamics, and for the continuum model approach, applied to isotropic media.

The need to model the wave propagations in materials is due to the required theoretical explanation of their physical parameters (e.g. density, velocity, time-of-flight, etc.) under different subjected conditions (e.g. stress, heat, compression etc.). Continuum theories or (macroscopic) models explain quantitative variations in the material's elastic properties without any abrupt changes or discontinuities. Modeling an object as a continuum assumes that the substance of the object completely fills the space it occupies. The continuum modeling approach deals with the physical properties of solids and fluids which are independent of any particular co-ordinate system in which they are observed. These physical properties are then represented by tensors, which are mathematical objects that have the required property of being independent of coordinate system. In contrast, the discrete theories or (microscopic) models explain these variations using small discontinued sets of physical properties. Modeling objects in this way properly addresses the fact that matter is made of atoms, discontinued with empty space and so is not continuous; and at the same time the properties can vary greatly over inter-atomic distances due to the nonlinear forces acting between the atoms.

The purpose of the study in this chapter is to compare analytically the resulted physical parameters from both of the above mentioned models (or approaches) for bulk and guided acoustic waves. The comparison would provide us the most suitable modeling approach which will be used to proceed further to our development and investigation of theoretical modeling of acoustic wave propagations in solid materials under variable conditions.

2.1 Microscopic approach

In the microscopic approach, a linear chain is treated, consisting of mass-free ideal springs with spring constant C . These springs are idealized according to Hooke's original definition [1]. The idealized springs connect point masses with mass m positioned in a linear (chain) arrangement at distance a (shown in figure 1).

The properties of waves, in the examples given here for guided acoustic waves or from a quantum mechanical point of view, phonons in one dimensional atomic chain, can be demonstrated by the dispersion relation, equating the dependence of (angular) frequency ω on wave number k (k -vector) respectively in the microscopic model the dependence of quantum energy on the also quantized (linear) momentum. In this scheme the phase velocity for a wave (excitation) of a given k -vector is derived from the quotient and the group velocity from the respective gradient (in lower dimensions: derivative) of the dispersion relation at position k .

Analytical comparison

For simplification it is assumed that the forces act along the springs instantaneously (the speed of light as limit velocity would such need to be infinite). For acoustic waves, traveling at only about 1/100 000 of the speed of light, this assumption leads only to small, even though in some cases not negligible deviations.

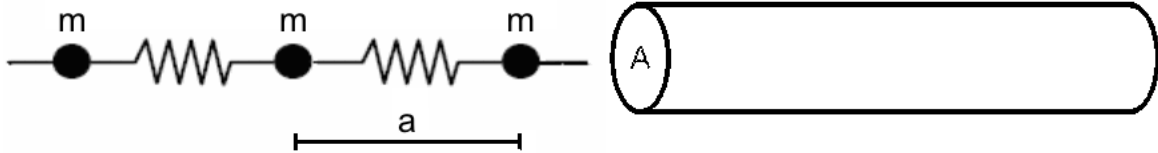


Figure 1: Linear mass-spring chain (left) and isotropic homogeneous rod with cross-sectional area A (right).

As pointed out in the literature [2] concerning acoustic excitations with longitudinal (along the chain) particle velocity, the linear chain obeys the following dispersion relation:

$$\omega = \sqrt{C/m} \sin(ka/2)$$

The technically relevant applications on which this article is concentrating relate to the microscopic model with representing atomic distances to the large wavelength limit ($k \rightarrow 0$). In that case group and phase velocities are equal and both are represented by

$$v = a\sqrt{C/m}$$

The result demonstrates that for any applied stress leading to an increase of the velocity, this velocity will increase exactly such that the time-of-flight (T_a) to travel the distance 'a' is

$$T_a = 1/\sqrt{C/m}$$

and will therefore be independent of any variation of 'a' due to external stress. It should be kept in mind that ideal springs relating to parabolic potentials for the respective binding forces are assumed here together with a non-relativistic simplification. Realistic interaction between mass points with "only" the speed of light would lead to a correction in time-of-flight of about 1 ps for any 0.3 mm elongation – normally too small to be relevant in experiments.

Based on the experimental findings, the usually observed substantially larger rise of the time-of-flight under dilatational stress can therefore on the basis of this model only be due to nonlinear springs as introduced by potentials deviating from parabolic shape leading to the binding forces modeled by springs.

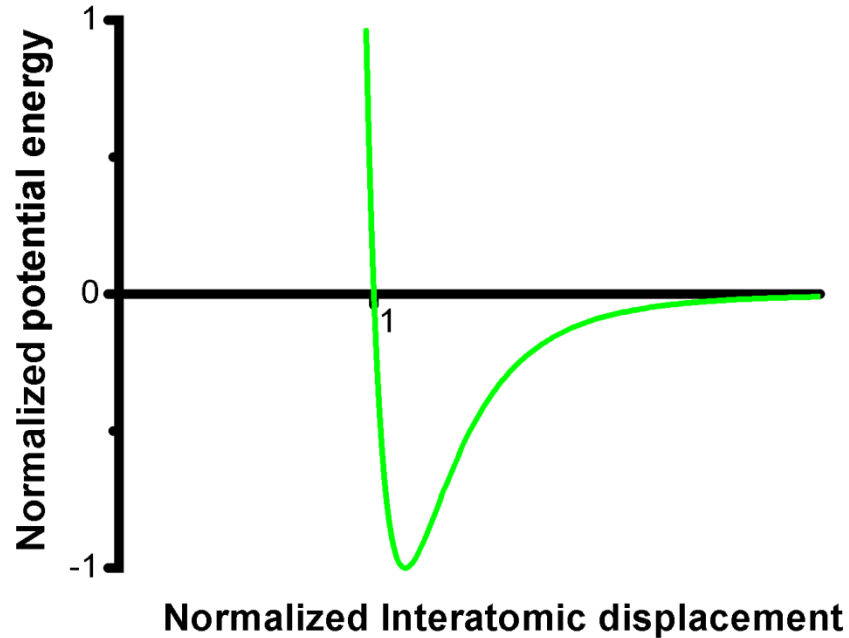


Figure 2: Lennard-Jones potential with inter-atomic distance 1 for equilibrium position.

The well-known Lennard-Jones potential [3] (figure 2) used for modeling of inter-atomic forces can serve here to demonstrate the main features as observed in experiments for longitudinal polarized bulk acoustic waves, for which the linear chain model is a simplifying example. This will lead to a reduced spring constant under dilatation and an increased one for compression. As a result, the time-of-flight of acoustic waves traveling along the direction of the applied stress will increase for dilatational stress.

2.2 Macroscopic approach

Macroscopic modeling suitable for comparison with the linear chain model has been treated extensively in the literature [4]. A choice from basic models of guided acoustic waves travelling on rods assuming the validity of a continuum model is well suited for this purpose. In this approximation the involved masses are introduced as (mass) densities ρ together with respective volumes. The elastic properties of rod shaped materials relevant for guided waves of the lowest branch of the axial-radial mode serving here as relevant example (figure 3) are expressed by Young's modulus E .

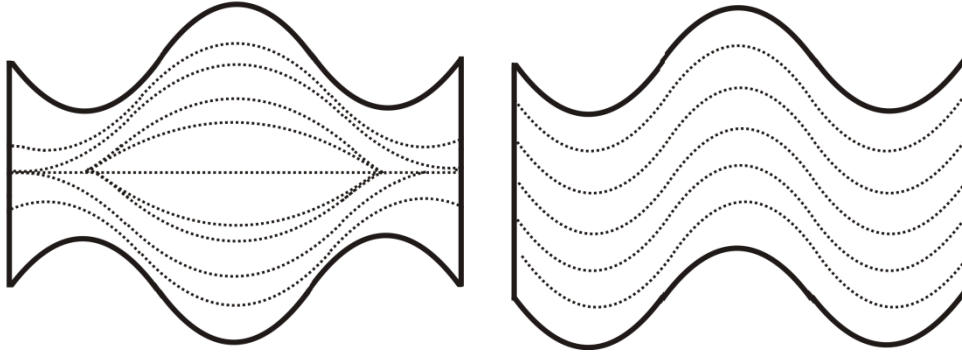


Figure 3: Deformation for the lowest branch of the different modes for guided acoustic waves traveling in a rod. Where left is axial-radial and right is flexural mode.

The velocity of the axial-radial mode in the long wavelength limit is independent of the actual cross-sectional sizes of the rod and exhibits vanishing dispersion [5]. Therefore it can be expressed equally for phase and group velocity in that limit by:

$$v = \sqrt{E/\rho}$$

In this model, the velocity depends exclusively on E and ρ . If E , as assumed in the original definition, is not depending on stress, corresponding to linear elastic behavior (similar as for Hooke's idealized spring), a variation of the speed can only be introduced by a variation of the density.

2.3 Stress dependence of TOF in macroscopic approach

It is evident that E will vanish when the shear modulus is zero, which is the case for a liquid. Even though it should be kept in mind that viscosity will lead to dynamic shear stiffness, here only the static case is considered, on which the original definitions of the mechanical properties used here are based. It is therefore implicitly implied that the Poisson ratio [6] (or Poisson number) ν cannot have the value 0.5 for the example modeled here. Therefore a relative variation of the volume dV/V will be inevitably introduced by any applied stress. The range of the Poisson ratio of stable materials is -1 to 0.5 with typical values for metallic alloys in the range of 0.2 to 0.3. Depending on the actual Poisson ratio, the density will be reduced if the solid rod is elongated by stress. This will lead to an increase of the velocity since the density will exhibit a relative decrease if the volume increases

$$d\rho/\rho = -dV/V$$

Following the definition of the Poisson ratio, the relative variation of the volume can be related to the respective length variation (for sufficiently small variations) by

$$dV/V = (1 - 2\nu) dL/L$$

Analytical comparison

leading to $d\rho/\rho = -(1 - 2\nu) d/l = (2\nu - 1) d/l$

The time-of-flight (t_{of}) will therefore under dilatational stress exhibit a relative change dt_{of}/t_{of} that on one hand could be >1 since the length will increase by d and on the other hand could be <1 since the velocity of acoustic waves will increase. Therefore relevant changes are related (for small variations with higher order terms neglected) by

$$dt_{of}/t_{of} = d/l - dv/v \quad [\text{Appendix 2.1}]$$

Simply expressing that if length and velocity vary just by the same, sufficiently small amount in opposite direction, TOF will (approximately) not change.

From $v = \sqrt{E/\rho}$, it can be derived that for E independent of the stress, as assumed here

$$(v + dv)/v = \sqrt{\rho/(\rho + d\rho)}$$

and $dv/v = 1/\sqrt{1 + d\rho/\rho} - 1 \quad [\text{Appendix 2.2}]$

which is, as to be expected, zero for vanishing density variation. Inserting the expression for the density variation leads to

$$dv/v = 1/\sqrt{1 + (2\nu - 1)d/l} - 1$$

which is, also as to be expected, zero for $\nu = 0.5$. With this result follows:

$$dt_{of}/t_{of} = d/l + 1 - 1/\sqrt{1 + (2\nu - 1)d/l}$$

This holds, under the given assumptions, for homogeneous materials with any Poisson ratio ν . For a Poisson ratio of 0.5 (even though not realistic for a solid rod but introduced here as a limit value) the relative variation of the time-of-flight would be determined by

$$dt_{of}/t_{of} = d/l$$

dt_{of}/t_{of} is proportional to the respective variation of the length d/l as to be expected for bulk waves in a liquid. Furthermore, for any practically relevant Poisson ratio between 0.5 and 0 it is evident that dt_{of}/t_{of} has the same sign as d/l since for small enough variation (higher order terms neglected) the following holds:

$$dt_{of}/t_{of} = d/l + (\nu - 1/2) d/l = d/l (1/2 + \nu) \quad [\text{Appendix 2.3}]$$

For the macroscopic model shown here (under the given conditions), the time-of-flight for acoustic waves traveling along the direction of elongation should therefore always rise under extensional stress for any practically relevant Poisson ratio $0.5 > \nu > -0.5$. It should be pointed out here, that a further simplification with respect to the one treated above such that E and ρ are both not dependent on deformation under stress would lead to a further increase of the time-of-flight with elongation.

The just treated already detailed but not yet fully realistic modeling is mainly performed here to point out, that simple so called “common sense” arguments like the sample is getting longer under stress and the ultrasound signals should therefore arrive later, are not only not necessarily true, they can even be opposed by well-known and easily accessible results if sound generated by string instruments is taken as an example. Therefore we turn in the next paragraphs to respectively refined modeling.

2.4 Stress dependence of TOF in microscopic approach

The basic features concerning the dispersion relations [7] for the microscopic approach discussed here are presented in figure 4.

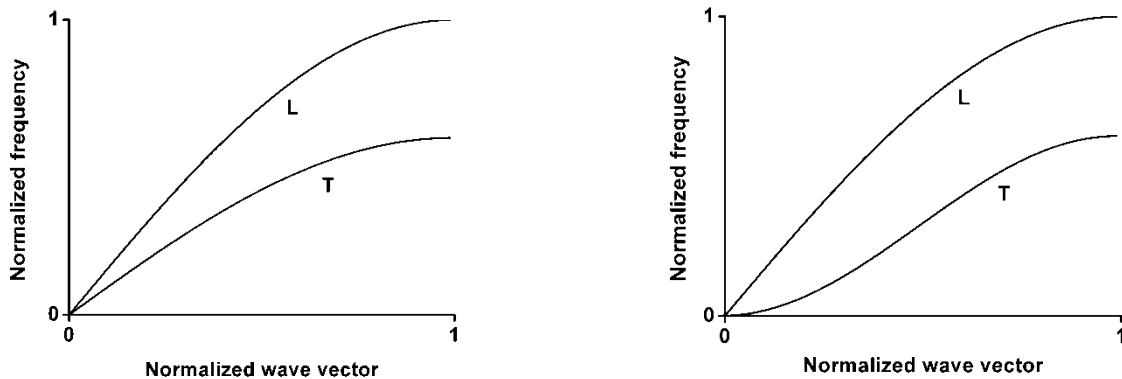


Figure 4: The graphs display the typical features of the dispersion relations [7] for longitudinal and transversal polarized acoustic waves (phonons) traveling on a linear chain (left) as also commonly treated in lattice dynamics, and dispersion relations for stretching phonons (right), relating to waves traveling on soft strings where restoring forces are provided by pull (extensional stress) only.

The longitudinal phonon branches have in both cases demonstrated the shape well known from lattice dynamics [2], the transversal (or T-) mode exhibits an unusual relation with diminishing group velocity in the long wavelength limit and subsequently rising group velocity for diminishing wavelength. This can easily be understood by the relative softening of a bar supported at two positions at (axial) distance d and a central load with respect to this support. The bar will turn soft under lateral loads (forces) if d increases.

2.5 Difference in the stress dependence of TOF between micro- and macroscopic approaches

The differences for the demonstrated results and accompanying artifacts arise on one hand from the inadequate definition of velocity, which is defined in s/m (units of time per units of length) but should be defined for the purpose of this discussion in a normalized way, namely in units of time per unit of the lattice or crystal respectively per distance between point masses (in the above microscopic linear chain model in s/a). We have therefore restrained here from expressing results as variations of the velocity and discuss the variation of the time-of-flight instead, which is also the actually observed variable. On the other hand the simplifying assumption that Young's modulus E is supposed to not depend on deformation to allow comparison with a microscopic model based on springs according to Hooke's law, is a not valid simplification for any available material. It serves here only the purpose to demonstrate which properties are needed to explain the experimentally observed results. A softening of the material under extensional stress, as to be expected from common models for the binding potentials as the Lenard-Jones potential, would lead to a reduced E (Young's modulus). This would even enhance the already demonstrated feature that TOF rises proportional to elongation.

By comparison of the first two different models, based on a microscopic approach generally used as a basis for lattice dynamics, and a macroscopic approach based on a continuum model, which is well established for modeling on macroscopic scales, the valid equations (see sections 2.1 and 2.2) allow to identify the relations between the respective terms used to describe the material properties. This leads to the following:

$$a^2 \cdot C / m = E/\rho$$

and therefore

$$C / m \propto E/\rho$$

This again seems to indicate that the result concerning the variation of the time-of-flight under stress should be identical, which they are not, as demonstrated above, due to implied additional conditions in the definition of the parameters used to describe the mechanical properties in the macroscopic model.

Also the guided mode traveling on a rod is a mixed mode including longitudinal and transverse components. Propagating transverse vibrations traveling on a linear chain can exist even in the absence of bending stiffness and are usually described by stretching phonons [8]. If a bending force constant f is present on the chain, the dispersion relation [7] for transverse polarized acoustic waves is represented by

$$\omega = 2\sqrt{f/m} [1 - \cos(ka)]$$

and in the case of acoustic limit ($k \rightarrow 0$) the dispersion relation gets the shape to

$$\omega = a^2 k^2 \sqrt{f/m}$$

The group velocity for transverse polarized acoustic waves traveling under the presence of a bending force (but not including stretching forces) is given by

Analytical comparison

$$v = 2a^2k\sqrt{f/m}$$

Group and phase velocities are zero for $k = 0$ corresponding to $\lambda \rightarrow \infty$ since restoring lateral forces approach zero. The group velocity is also zero at the boundary of the Brillion zone $k = \pi/a$ where standing waves are established. This case is nevertheless not of relevance for the applications treated here.

If for simplicity stiff solid connections relating to an infinite spring constant are assumed (similar to an idealized regular chain), the length of the chain will not vary under stress and the relative change of the time-of-flight for transversal polarized acoustic waves traveling only under the influence of the bending forces, which should not depend on stress if defined in the here generally selected simplified way, should be zero. The argument is thereby similar if not even simpler, since elongation is in a perfectly rigid chain absent, as for the longitudinal polarized acoustic waves traveling on a chain. Nevertheless a non-realistic assumption has been made since (longitudinal) stress will lead to stiffening by providing restoring force for any lateral deformation. As known from the “stretching” phonons this will lead to a reduction of TOF for increasing extensional stress, which in the idealized case assuming also ideal bending springs (not depending on elongation) will alone determine the dependence of TOF on (longitudinal respectively extensional) stress. These to be expected effects can most easily be studied by turning to a macroscopic description presented here.

For transverse polarized waves traveling on a non-stiff string a well-established macroscopic model is available. The dispersion relation for that case, relevant to any string instrument, leads to a phase and group velocity for propagating transverse vibrations [9] given by

$$v = \sqrt{T/\mu}$$

with T representing the tension (axial stress) and μ representing the mass per unit length of the string. Since in this model the string is treated as totally stiff concerning tensional stress even though totally soft concerning bending, the length would not change under stress and conditions concerning the variation of the time-of-flight under tensional stress are similar as for the already discussed microscopic model for the transversal polarized stretching mode in the long wavelength approximation.

Respectively for the microscopic modeling of transversal polarized acoustic waves traveling in shear stiff materials, the forces are normally chosen such, that they do not depend on distance and, as pointed out already for longitudinal polarization, the time-of-flight will under such idealized conditions not depend on stress (at least if the just treated stretching modes are not included in the modeling).

Macroscopic modeling based on a continuum approach for isotropic media leads to identical group and phase velocities for transversal polarization as for example also valid for the torsional guided mode (figure 3) and respective dispersion relations as given by literature [10]. The velocity of acoustic shear waves in that case is:

$$v = \sqrt{G/\rho}$$

where G is the shear modulus. For an idealized case with infinite stiffness concerning dilatation (and compression) the time-of-flight could not be influenced since variations of the density are not possible, if G is assumed to be independent of stress. For realistic and therefore finite extensional stiffness, the effects caused by deformation will also be influenced by a variation of the density in a similar way as already discussed above in the macroscopic approach for the axial-radial guided mode. It has to be stated here that geometric stiffening, not contained in simple modeling may influence the result and would contribute by a reduction of TOF under tensional stress. Furthermore anharmonic behavior has to be included (higher order elastic constants) which would normally lead, due to softening on extension, to an increase of the time-of-flight under dilatational stress.

2.6 Summary

The results of microscopic and macroscopic modeling (approaches) for the stress dependence of propagating acoustic modes in isotropic solids are compared. The comparison has revealed the limitations of both modeling approaches and their respective advantages especially at long wavelengths. The essential achievements of this task in addition to the already well-known anharmonic effects, contributing to the variations of the time-of-flight of ultrasonic waves, general principles are identified and highlighted. The two most important ones are that harmonic materials will not show stress dependencies for the time-of-flight for longitudinally polarized bulk modes and, even more important, geometric effects can lead to substantial stiffening for guided modes which is most pronounced for the anti-symmetric Lamb waves. This is introduced here for the first time as “geometrical stiffening”. The on first view rather academic result is on one hand well known for string instruments and on the other hand most valuable for applications, since the different dependencies allow to differentiate against thermal effects, which are dominantly of the anharmonic type. Since even changes of the sign are involved if the here identified geometrical stiffening is implied, rather rugged detection schemes can be based on the elementary treatment provided here also with respect to the literature [11].

2.7 References

- [1] Robert Hooke, “Ut tension, sic vis, (meaning: as the extension, so the force)”, (1678)
- [2] Charles Kittel, “Introduction to solid state physics”, Published by John Wiley and Sons, 8th edition, (2008)
- [3] Lennard-Jones, “Cohesion”, Proceedings of the Physical Society 43”, pp. 461-482, (1931)
- [4] G. F. Swain, “Structural Engineering: Fundamental Properties of Materials”, Published by McGraw-Hill Company, (2008)
- [5] T. D. Rossing, N. H. Fletcher, “Principles of vibration and sound”, Published by Springer Science and Business Media LLC, 2nd edition, (2003)

- [6] H. Gercek, "Poisson's ratio values for rocks", *International Journal of Rock Mechanics and Mining Sciences*, Elsevier 44, pp. 1–13, (2007)
- [7] G. Hartwig, "Polymer properties at room and cryogenic temperatures", Published by Springer, (1994)
- [8] G. P. Srivastav, "The Physics of Phonons", Published by CRC Press, (1990)
- [9] T. C. A. Molteno, N. B. Tuffaro, "An experimental investigation into the dynamics of a string", *American Journal of Physics* 72 (9), pp. 1157–1169, (2004)
- [10] C. M. R. Fowler, "The Solid Earth", Published by Cambridge University Press UK, (1990)
- [11] K. S. Tarar, R. Meier, U. Amjad, W. Grill, "Stress detection with guided acoustic ultrasonic waves by nonlinear elastic and geometric effects", *SPIE Proc.* 729518, (2009)

3. Developed theory for bulk acoustic waves

The basic features of the dependence of the time-of-flight (TOF) of bulk acoustic waves on elongation under stress are treated and exemplified for a linear chain using lattice dynamics approach. The chains are constructed from point masses connected by mass-free (lateral and torsional) springs acting instantaneously. The results achieved from this modeling simulating the lowest symmetric (L) and anti-symmetric (T) modes demonstrated analytically the expected variations in TOF due to external stress in the acoustic waves.

Lattice dynamics extends the concept of crystal lattice to an array of atoms with finite masses that are capable of motion. This motion is not random but is a superposition of vibrations of atoms around their equilibrium positions due to the interaction with neighboring atoms. The problem of lattice dynamics is to find the normal modes of vibration of a crystal which in the simplest approach is represented by a linear chain. This is achieved by calculating the energies (or frequencies) of the phonons as a function of their wave vector k . The relationship between ω and k is called phonon dispersion relation. Dispersion relations describe the ways that wave propagation varies with the wavelength or frequency of a wave. The wave nature [1-2] of all traveling objects is the key to understand how energy and objects are transported from point to point in any medium. This was first observed [3] in the dispersion of waves on water for example by Pierre-Simon Laplace in 1776. Continuum mechanics [4] cannot provide a microscopic approach that can fully identify the origin of effects related to the transport of acoustic waves under applied stress. Therefore the lattice dynamics (modeling) approach is employed here to illustrate the dependencies of velocity and time-of-flight (TOF) on external forces causing anharmonicity. A comparison with conventional continuum mechanics has already been given in a preceding chapter (chapter 2) and publication [5].

The here presented models have been used to demonstrate the dependence of the TOF on extensional stress for low frequency symmetric and anti-symmetric (represented by L- or longitudinal, and T- or transversal) modes respectively under idealized and generalized elastic conditions. This kind of modeling can support the understanding of the expected behavior of solid materials under variable elastic conditions depending on applied stress and temperature.

3.1 L-mode vibrations

The microscopic approach is used here to develop a lengthwise flexible linear chain mass-spring model to investigate the extensional stress effects on longitudinally polarized modes of bulk acoustic waves.

The model [6] has used the TOF as a parameter to monitor the variations due to stress in the ultrasonic waves. The effects caused by anharmonicity (in the chain) lead to an increase in the monitored time-of-flight, whereas the TOF in a harmonic (or idealized) chain with forces transferred instantly is independent of tension.

3.1.1 Lattice dynamic modeling

Consider a chain of mass-free springs connected to mass points as shown for equilibrium positions in figure 1. The equation of motion of total force F_n acting on the mass m_n for this system is; as known from the literature [7]:

$$\begin{aligned}
 F_n &= C \cdot (a_{n+1} + a_{n-1} - 2a_n) \\
 m \cdot d^2 a_n / dt^2 &= C \cdot (a_{n+1} + a_{n-1} - 2a_n) \\
 d^2 a_n / dt^2 &= C/m \cdot (a_{n+1} + a_{n-1} - 2a_n)
 \end{aligned} \tag{1}$$

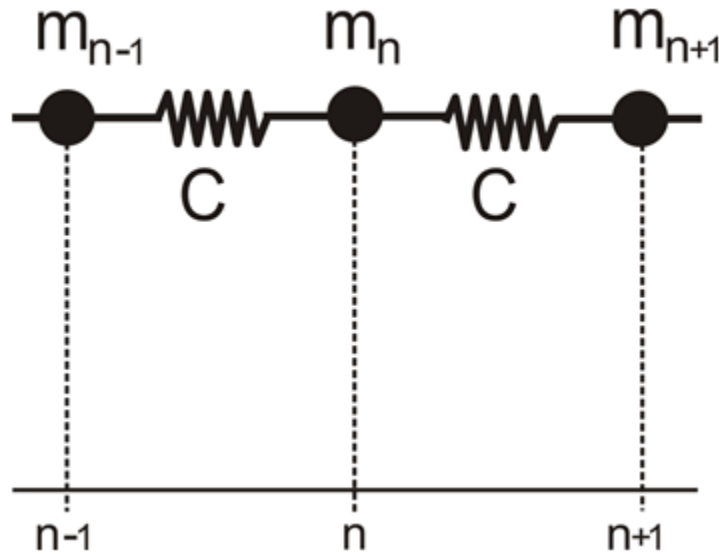


Figure 1: Linear chain of masses and mass-free springs with the masses m_{n-1} , m_n , m_{n+1} at (static) equilibrium positions $n-1$, n , and $n+1$ (in the absence of external forces).

With t denoting the time, equation (1) is the wave equation of the system displayed in figure 1, in which C is the spring coefficient of any of the individual idealized mass-free springs, m is the mass of any of the individual point masses, a is the lattice distance under equilibrium condition and m_n , m_{n+1} and m_{n-1} are three point masses of the chain at respective positions n , $n + 1$, and $n - 1$. The actual mass of any of the point masses is m .

A solution [appendix 3.1] of the wave equation (1) for longitudinally polarized acoustic waves with particle velocities oriented along the chain, under the above given conditions will be:

$$\omega = 2 \cdot (C/m)^{1/2} \cdot \sin(k \cdot a/2) \tag{2}$$

Here ω is the angular frequency and k is the wave number (related to the respective wave vector).

If the mass-spring system is now stretched by an external pair of forces acting on the (assumed to be far away) ends of the chain or simply by a respectively defined stress, the chain will expand. New equilibrium positions for the neighboring masses m_{n+1} and m_{n-1} with respect to the mass m_n as shown in figure 2 will result.

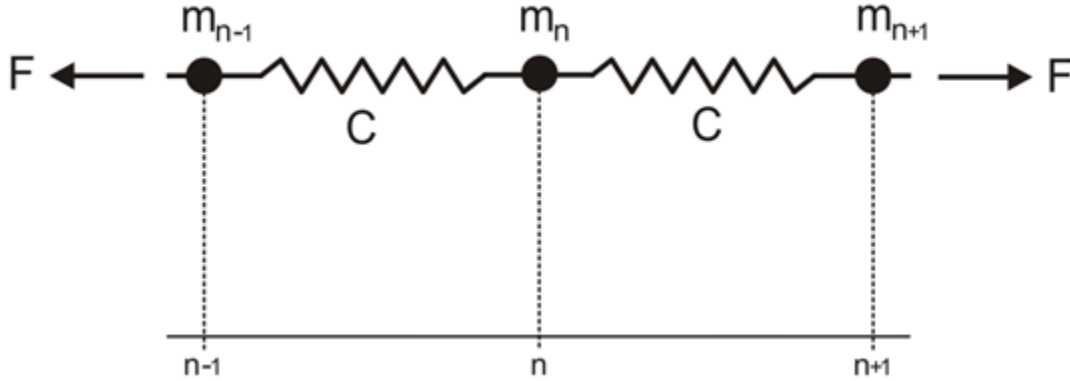


Figure 2: Linear chain of masses and mass-free springs as in figure 1 but under externally applied stress in (static) equilibrium condition.

Since in figures 1 and 2 the (static) equilibrium condition is observed, which actually would take an infinite time to establish if no friction is assumed, inertial forces have vanished. The stress will only affect the lattice parameter a , which will adjust for idealized springs according to Hooke's law [8] with the spring coefficient C . The dynamics under stress for this case are treated in the following text.

3.1.2 Harmonic vibrations

The extension under stress can be determined by use of the inverse Hooke's law. This involves not only an exactly linear relation of force and dilatation but in the idealized case treated here also a mass-free spring that acts concerning the transfer of forces instantly and therefore not only beyond the speed of light but with infinite speed. To emphasize the linear character of the spring we denote the spring coefficient now as C_1 since the linear relation will later be replaced by more complicated functions, where a linear approximation would at best be a first order term. Otherwise the conditions are as illustrated in figures 1 and 2. A stress induced externally by two opposing pulling forces, with F as the amount of each, acting at the far ends of the chain (along its extension) leads to a lattice parameter a_F that will establish under static equilibrium and is given by

$$a_F = a_0 + F/C_1 \quad (3)$$

since according to Hooke's law

$$C_1 = F/(a_F - a_0)$$

with the lattice distance a_0 for no pull or push applied (i.e. zero stress).

Modeling of bulk acoustic waves

The dispersion relation (equation 2) for harmonic vibrations in a linear chain is modified under extensional stress to:

$$\omega_F = 2 \cdot (C_l/m)^{1/2} \cdot \sin(k \cdot a_F/2) \quad (4)$$

A graphical representation of the stress affected dispersion relation (equation 4) is given in figure 3 for extensional stress.

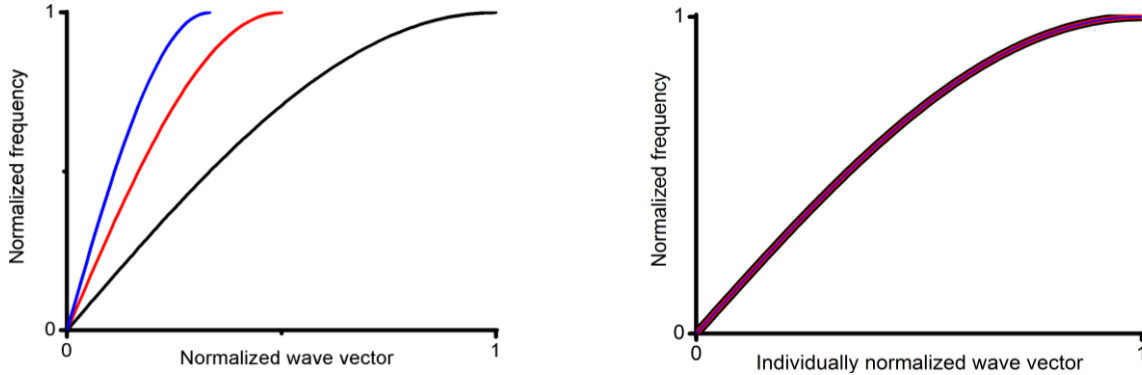


Figure 3: Graphical representation of the dispersion relation (equation 4) for springs following Hooke's law. In the left graph the wave vector is normalized to the dispersion relation valid in the absence of tension for the range to the zone boundary including the results for forces leading to a **doubling and **tripling** of the distances between point masses. In the right graph the dispersion relations are normalized individually to the wave vector at the zone boundary. The different dispersion relations under stress coincide in that representation, demonstrating that TOF per unit cell is constant under stress in the harmonic approximation.**

The phase and group velocities for dispersion relation (equation 4) are generally defined as:

$$\begin{aligned} \omega_F/k &= V_{(ph)} && \text{(phase velocity)} \\ d\omega_F/dk &= V_{(gr)} && \text{(group velocity)} \end{aligned}$$

The phase velocity for a linear chain under stress is therefore

$$\begin{aligned} \omega_F/k &= 2/k \cdot (C_l/m)^{1/2} \cdot \sin(k \cdot a_F/2) \\ V_{(ph)} &= 2/k \cdot (C_l/m)^{1/2} \cdot \sin(k \cdot a_F/2) \end{aligned} \quad (5)$$

According to the definition, the group velocity is obtained from the derivative of equation (4) with respect to wave vector

$$\begin{aligned} d\omega_F/dk &= 2 \cdot (C_l/m)^{1/2} \cdot \cos(k \cdot a_F/2) \cdot (a_F/2) \\ V_{(gr)} &= a_F \cdot (C_l/m)^{1/2} \cdot \cos(k \cdot a_F/2) \end{aligned} \quad (6)$$

As we are interested here only in the long wavelength limit ($k \rightarrow 0$), the equation (6) can be written as

$$V_{(gr)} = a_F \cdot (C_l/m)^{1/2} \quad (7)$$

In the limit of $k \rightarrow 0$, the group velocity is also represented by

$$V_{(gr)} = a_F/TOF \quad (8)$$

with

a_F = Total lattice distance (including extended due to pulling force)

TOF = Total time-of-flight taken to complete the lattice distance a_F

In the long wavelength limit phase and group velocities are identical. In this limit a linear dispersion is valid. Equations (7) and (8) lead concerning the TOF needed to pass a single unit cell of the chain to

$$\begin{aligned} a_F/TOF &= a_F \cdot (C_l/m)^{1/2} \\ TOF &= (m/C_l)^{1/2} \end{aligned} \quad (9)$$

which means the TOF will remain constant. This fact (equation 9) has also been proved by one of our own experimental results (figure 4) in the form of non-variations of TOF (at low frequencies).

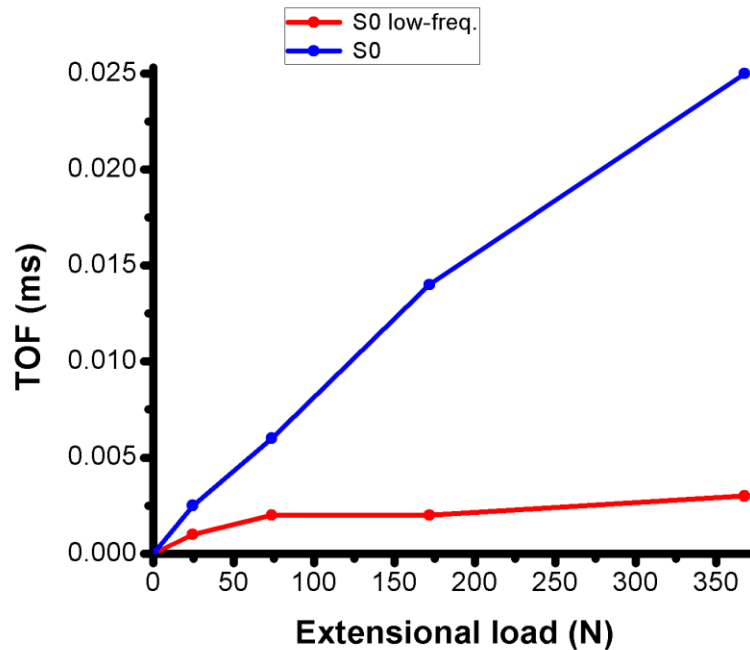


Figure 4: The plotted graph shows the experimental results [9] for two separate symmetric modes of an aluminum (1 mm thick) strip being loaded with blue line showing S0 mode at frequency range of 0.002 MHz to 1.5 MHz, and red line showing S0 mode at lower frequency range of 100 kHz to 220 kHz with circular dots as measured data points.

Despite the initial jump (which is due to the sudden start of loading of the material) in the measured data (red) line for low frequency S0 mode having a frequency range between 100 kHz to 220 kHz, the rest of the line shows an almost constant feature in TOF with increasing load on aluminum strip. The second set of data (blue) line is not generated in the lower frequency range (0.002 MHz to 1.5 MHz), and has shown respectively the different behavior upon stress, and so is not the subject of our discussion. The time-of-flight (TOF) to pass any fixed number of unit cells therefore remains constant under variable stress. This is to be expected if, as assumed, the springs act instantly (no relativistic correction), are free of mass and point masses are involved. The chain resembles a wave machine as often used to exemplify waves. In these devices a rather low speed can be adjusted by employing large masses and soft springs. In the case of wave machines the speed is usually adjusted such that the traveling waves can be followed by eyesight. Since the springs are here idealized as acting instantaneously, the lengthening of the spring cannot change the time needed to transfer the energy to a neighboring mass in the chain.

If, on the other hand, one argues as usually addressed, than even for harmonic springs the wave speed gets faster under stress, since to determine the speed, any observed travel time has to be related by definition to unit length. But the speed increases for harmonic springs to the same degree as the lattice constant increases by the applied stress. Therefore for any given sample (part of the infinitely long chain observed here) TOF will remain constant under strain induced by stress if idealized point masses and instantly acting springs are involved. The argument that the arrival time will increase under stress since the sample (represented here by the chain) is elongated is misleading and not valid for the idealized conditions assumed here for a simple representation of harmonic behaving materials.

Different to the modeling employed here, in reality the springs can only transfer energy with the speed of light. This will lead to a relativistic correction, which remains rather small, since the speed of acoustic waves and the speed of light (in vacuum) are typically 5 orders of magnitude apart.

3.1.3 Generalized vibrations

Anharmonicity in materials as modeled here is represented by a nonlinear mass-spring system. For a nonlinear spring the conventional Hooke's law can be amended to 2nd, 3rd, and nth order corrections with respect to the displacement. This is visualized here by splitting the acting spring into two parts, one linear (harmonic) and the other nonlinear as exemplified in figure 5. For simplicity only the second order correction is employed here in the Taylor expansion describing anharmonic springs by a modification of Hooke's law. Higher order terms can be used to describe the Lennard-Jones potential, usually employed to model inter-atomic forces. To identify the basic features, higher order corrections are left out of consideration in the presented approach, only generalized features are addressed.

The modified Hooke's law is used here to determine the variation of the distance between the mass points under applied stress. Near the respective modified equilibrium position (under stress), the springs are treated as being locally harmonic. In that way an

effective spring coefficient can be derived from the derivative of the modified Hooke's law with respect to displacement. This is justified only for vanishing respectively sufficiently small amplitudes of the mechanical waves involved. Since the aim of this chapter is to illustrate the variations of the TOF of acoustic waves and not to demonstrate the shape of sizeable anharmonic waves deviation from the harmonic case, this approximation is suitable. It allows to identify the essential effects independent of the actually chosen degree of correction concerning the approximative treatment of a Lenard-Jones potential or any other law for the dependence of forces on elongation. It may be worth noting here that ideal gases, if used as a spring in connection with a piston moving in a cylinder, also do not represent a spring following Hooke's law. The force function employed here as an example for any generalized force function F_g is a Hooke's law corrected with a second order term:

$$F_g = C_1 \cdot (a_F - a_0) - C_2/2 \cdot (a_F - a_0)^2 \quad (10)$$

C_1 represents the linear elasticity and C_2 the nonlinear one (of first order with respect to nonlinearity). They are replaced and assigned here by C_l and C_{nl} respectively (for linear and nonlinear terms).

$$F_g = (a_F - a_0) \cdot C_l - (a_F - a_0)^2 \cdot C_{nl}/2$$

With $\Delta = (a_F - a_0)$, this can be represented by:

$$\begin{aligned} dF_g / d\Delta &= C_l - C_{nl} \cdot \Delta \\ dF_g / d\Delta &= C_g \end{aligned} \quad (11)$$

Here $dF_g / d\Delta$ is denoted by C_g symbolizing the local effective spring coefficient of the generalized anharmonic spring. This is emphasized here to demonstrate that in the limit of diminishing amplitudes of the mechanical waves, the approach employed for harmonic springs can still be used with a modified spring coefficient, if Δ is kept approximately constant. Since the extension is derived from the actual spring function, it does not relate concerning the stress to this modified parameter of the spring as in the case of harmonic springs.

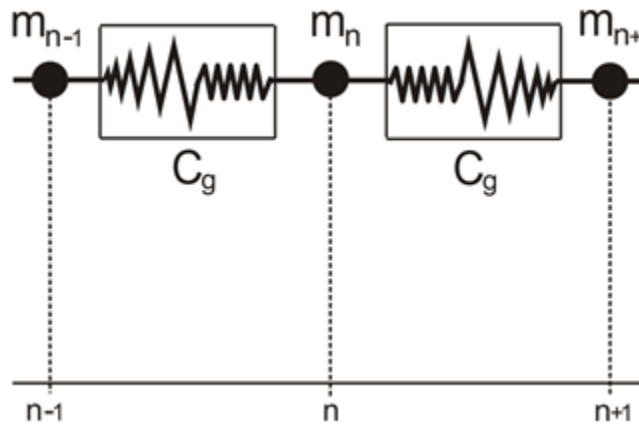


Figure 5: A combined mass-spring system including both harmonic and anharmonic modeled effects in the equilibrium state (without extensional stress).

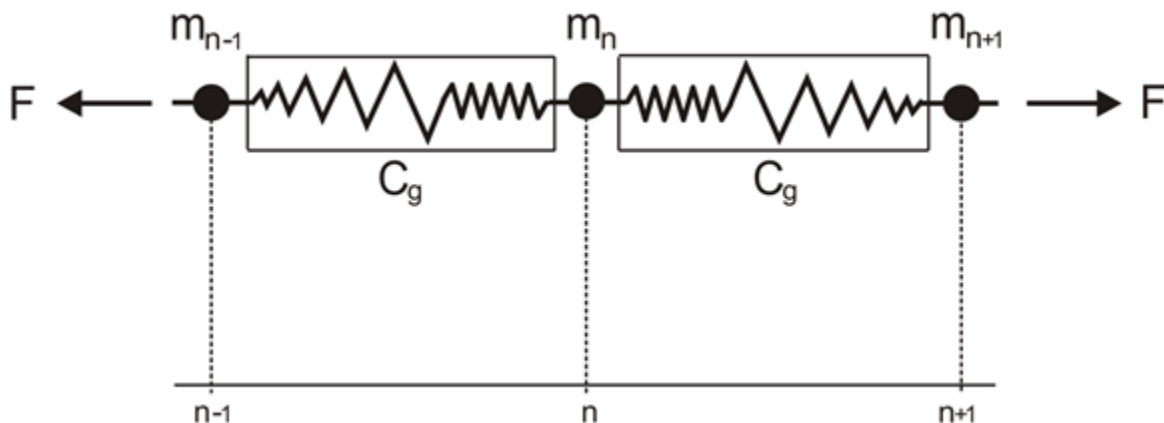


Figure 6: A combined mass-spring system including both harmonic and anharmonic modeled effects in the stretched state.

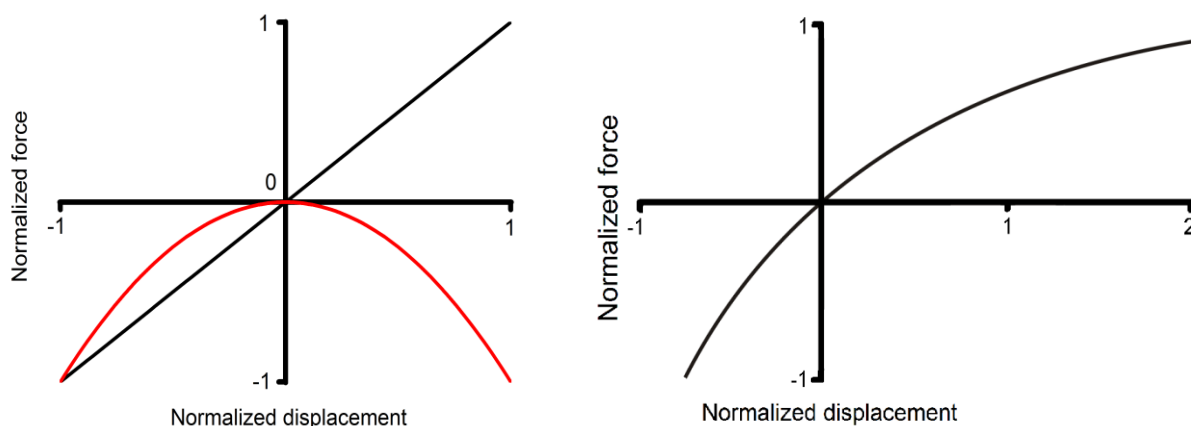


Figure 7: The normalized linear (1st) and 2nd order (**parabolic**) force coefficients (left side) and a force function resulting from a first order term of unity and a second order term of only 20% of the normalized anharmonic contribution (right side). The anharmonic term is here represented by an upside-down parabola to approximate the usual softening observed in materials under extension which can be identified by the slope in the right graph.

The anharmonic spring as displayed in figure⁷ concerning the dependence of force on elongation can locally be represented by a spring coefficient derived from the actual slope. For zero elongation and oscillations with negligible small amplitudes the spring coefficient is given by the linear term C_l only (same as for the harmonic case). For elongated springs as caused by extensional stress the effective (local) spring coefficient C_g (derivative of the function describing the spring as displayed in figure⁷) will be reduced for the spring assumed here which turns soft on elongation.

Modeling of bulk acoustic waves

Under the given assumptions, the linear mass-spring chain can be treated for small deviations as caused by oscillations with diminishing amplitude by

$$a_F = a_0 + F_g/C_g \quad (12)$$

Here F_g and C_g are the functions already defined in equations (10) and (11). The dispersion relation listed in equation (2) can be amended to:

$$\omega_F = 2 \cdot (C_g/m)^{1/2} \cdot \sin(k \cdot a_F/2) \quad (13)$$

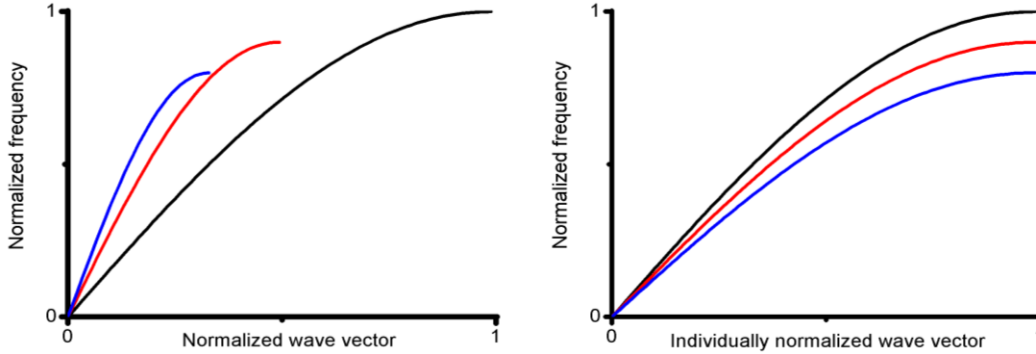


Figure 8: Graphical representation of the dispersion relation (equation 13) for anharmonic springs under variable stress. In the left graph, the wave vector is normalized to the dispersion relation valid in the absence of tension for the range to the zone boundary. Extension by external forces leads to steeper dispersion relations and an increase of the distance between neighboring point masses resulting in a decrease of the periodicity of the dispersion relation. In the right graph, the wave vectors are individually normalized, to show the variation in the time-of-flight needed to pass a single unit cell with length a_F which **doubles and **triples** with respect to the length for the unstressed chain.**

Respective results (in figure 8) are given for forces leading to a doubling and tripling of the distance between point masses. The rise of velocity present for doubling is reduced in the next step to tripling of the distance due to progressive softening. The anharmonicity affects the curves such that the velocity does not increase linearly with pulling forces (as can be observed in figure 3). The phase and group velocities under external stress can be written as

$$V_{(ph)} = 2/k \cdot (C_g/m)^{1/2} \cdot \sin(k \cdot a_F/2) \quad (14)$$

$$V_{(gr)} = a_F \cdot (C_g/m)^{1/2} \cdot \cos(k \cdot a_F/2) \quad (15)$$

For long wavelengths ($k \rightarrow 0$), the group velocity is

$$V_{(gr)} = a_F \cdot (C_g/m)^{1/2} \quad (16)$$

and the time-of-flight in this case is

$$TOF = (m/C_g)^{1/2} \quad (17)$$

The generalized model treated here in the lowest order approximation can already provide a valuable picture of the discussed problem. The dependence of the TOF of

longitudinal polarized acoustic waves in the limit of large wavelengths if treated even on a simple theoretical approach, can explain the TOF variations due to external pull, where variations can only be present if anharmonic effects are included. For springs softening on extension, an increase of TOF for propagation over any fixed number of unit cells is to be expected from the derived relations (equation 17). This is due to the fact that even though the velocity is at least for small enough extensions still increasing (figure 8, left), the lattice distance will increase to a higher degree resulting in an increase of the time-of-flight needed to pass one unit cell (figure 8, right). The same applies for any sample that is modeled in a sufficient approximation by the approach presented here.

The examples employed here involve elongations beyond any feasible limit for actual materials other than rubber and similar materials. The force function if derived from Morse [10] or Lennard-Jones potential [11] would exhibit similar features concerning the TOF under stress but would not allow stretching on the scales used here for demonstration. Extensions of only 2% lead usually to breakage for materials with such potentials concerning the binding forces. If these more realistic cases are used for demonstration, such small variations would arise that the differences could not easily be observed in respective graphs as employed here for illustration.

3.2 T-mode vibrations

The microscopic approach is used here to develop a transversally flexible mass-spring model to investigate the extensional stress effects on transversally polarized modes of bulk acoustic waves.

The model [9] has used the TOF as a parameter to monitor the variations due to stress in the ultrasonic waves. The effects caused by anharmonicity lead to an increase in the monitored TOF, which is modeled here in the form of force-arm's elongation. In the absence of any anharmonicity in an idealized (or harmonic) case, for transversely polarized acoustic waves, the TOF of the chain with forces transferred instantly will decrease with the increase of lengthwise tension.

3.2.1 Lattice dynamic modeling

The basic theoretical unit for transversely polarized acoustic mode can be visualized by three point masses and an extremely small torsional spring connected by two mass-free force-arms as shown in the figure 9. The equation of motion of total force applied on mass m_n for this system is equal to the restoring [12] rotating force (torque). The general equation of rotational force in this case would be

$$\vec{a} \times \vec{F}_n = -G \cdot \alpha$$

Here G is the torsional stiffness coefficient and α is the angle of twist from the equilibrium position of the spring. The direction of vector F_n (force acting on the n th

Modeling of bulk acoustic waves

point mass) is perpendicular to the force-arm a , so we can write it in scalar multiplication form as following:

$$\begin{aligned} F_n \cdot a \cdot \sin(90^\circ) &= -G \cdot \alpha \\ F_n \cdot a &= -G \cdot \alpha \end{aligned} \quad (18)$$

An important assumption taken here to develop this model is the small amplitude oscillations.

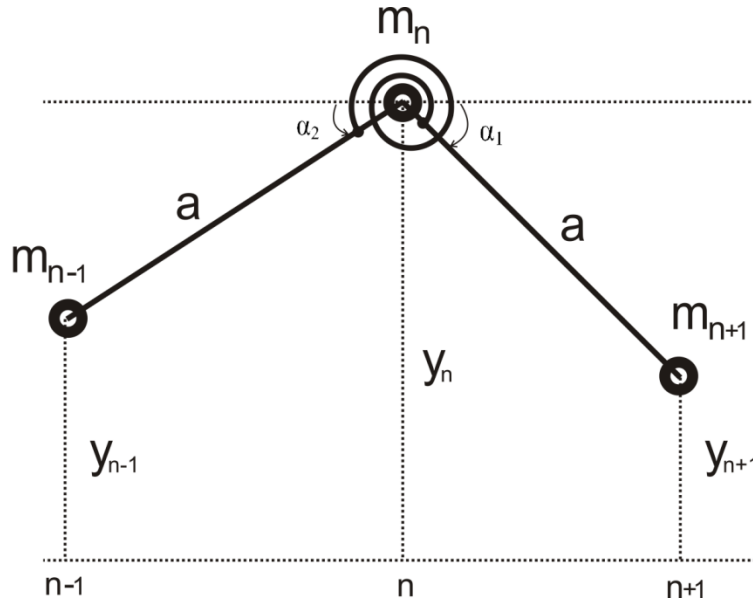


Figure 9: A mass-spring coupling system used for the demonstration of lowest anti-symmetric or (named here) T-mode vibrations.

Here α is the total angle of deflection of spring from equilibrium (figure 9). In this case the equation of motion can be written as

$$F_n \cdot a = -G \cdot (\alpha_1 + \alpha_2) \quad (19)$$

And for small amplitude (or angle) approximations; we can write

$$\sin(\alpha_1) \approx \alpha_1 \quad \text{and} \quad \sin(\alpha_2) \approx \alpha_2$$

Where

$$\sin(\alpha_1) = (y_n - y_{n+1}) / a \quad \text{and} \quad \sin(\alpha_2) = (y_n - y_{n-1}) / a$$

So in the above case; we can write

$$\alpha_1 = (y_n - y_{n+1}) / a \quad \text{and} \quad \alpha_2 = (y_n - y_{n-1}) / a$$

Thus equation (19) can such be reformulated as:

$$F_n = G/a^2 \cdot (y_{n+1} + y_{n-1} - 2y_n) \quad (20)$$

Modeling of bulk acoustic waves

The force F_n (acting on mass m_n) can be represented by Newton's 2nd law [13] of motion. Thus the wave equation (20) can be written as according to the following second order differential equation.

$$\begin{aligned} m \cdot d^2 y_n / dt^2 &= G/a^2 \cdot (y_{n+1} + y_{n-1} - 2y_n) \\ d^2 y_n / dt^2 &= G/(m \cdot a^2) \cdot (y_{n+1} + y_{n-1} - 2y_n) \end{aligned} \quad (21)$$

A frequency dependent solution [appendix 3.2] of the above wave equation (21) can be given as:

$$\omega = (2/a) \cdot (G/m)^{1/2} \cdot \sin(ka/2) \quad (22)$$

Here ω is the angular frequency and k is the wave number (related to the respective wave vector). This is the required dispersion relation representing the basic transversely polarized acoustic mode.

3.2.2 Harmonic vibrations

Suppose the initial position of the torsional mass-spring model is such that the angles α_1 and α_2 are equal (if taken from the given central vertical line). Here a_0 is the primary (constant) length of force-arms connecting to masses m_{n-1} and m_{n+1} . The sideways external pull in this case will affect such that the angles α_1 and α_2 will increase equally on both sides to become α_3 and α_4 respectively, also shown in figure 10.

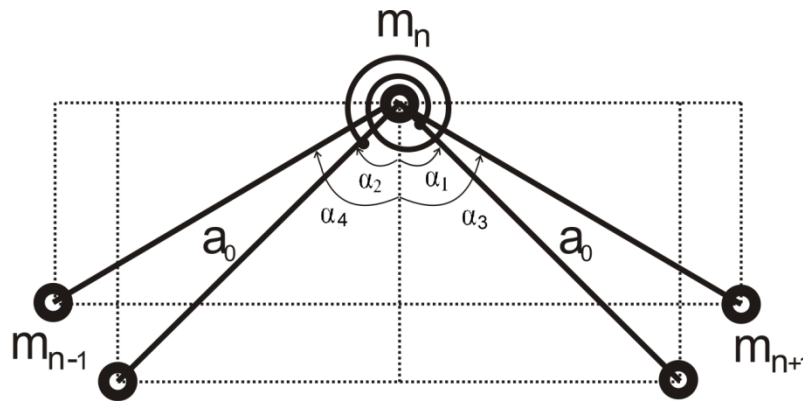


Figure 10: The mass-spring coupling system (as in figure 9) for T-mode vibrations before and after sideways applied pull.

A stress induced externally by two opposing pulling forces with F as the amount of each acting at the far ends of the chain (along its direction of extension) leads to a change in

Modeling of bulk acoustic waves

the effective lattice (transversely polarized) displacement function a_F [appendix 3.3] that will establish under static equilibrium and is here denoted by

$$a_F = a_0 \cdot \cos(\alpha_3) \quad (23)$$

Thus the dispersion relation (equation 22) for generalized vibrations of a mass-spring chain for transversal mode due to external pull can now be modified (by replacing a with a_F) as following

$$\omega_F = 2/a_F \cdot (G/m)^{1/2} \cdot \sin(k \cdot a_F/2) \quad (24)$$

A graphical representation of the stress affected dispersion relation (equation 24) is shown (in figure 11) as following.

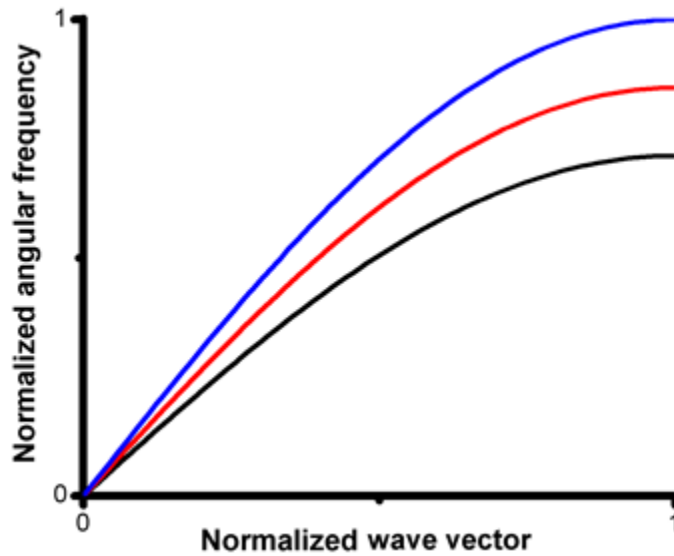


Figure 11: Sideways extensional force dependent dispersion relation (equation 24) of normalized angular frequency where the black, red, and blue color lines represent the effects of single, double and triple units of extensional pulling forces applied to the mass-spring chain.

The phase and group velocities for dispersion relation (equation 24) would become

$$V_{(ph)} = (2/ka_F) \cdot (G/m)^{1/2} \cdot \sin(ka_F/2) \quad (25)$$

$$V_{(gr)} = (G/m)^{1/2} \cdot \cos(ka_F/2) \quad (26)$$

As we are interested here only in the long wavelengths limit ($k \rightarrow 0$), the equation (26) can be written as

$$V_{(gr)} = (G/m)^{1/2} \quad (27)$$

In the above graph (figure 11), it's evident that the group velocity remains almost constant at lower frequencies even with the application of extensional force, and it changes only at higher frequencies with the extensional force. In the limit of $k \rightarrow 0$, the group velocity can also be represented by

$$V_{(gr)} = a_F/TOF \quad (28)$$

In the long wavelengths limit phase and group velocities are identical. In this limit a linear dispersion is valid. Thus by comparing equations (27) and (28)

$$\begin{aligned} a_F/TOF &= (G/m)^{1/2} \\ TOF &= a_F \cdot (m/G)^{1/2} \end{aligned} \quad (29)$$

As (m/G) is a constant term supposed in the model, the TOF becomes directly proportional to a_F

$$TOF \approx a_F \quad (30)$$

As lattice displacement a_0 is a constant value in this model, so by applying equation (23) in (30), the resultant TOF can be denoted as following:

$$TOF \approx \cos(\alpha_3) \quad (31)$$

Here α_3 is the extended angle (figure 10) due to extensional force F from its equilibrium position. When the angle increases due to extensional force, the resulting function value (equation 31) decreases which is directly proportional to the TOF. Thus equation (30) demonstrates that the transversely polarized acoustic modes are affected due to lengthwise external force such that they get faster at low frequencies.

That result only corresponds to the lowest order mode of transversely polarized bulk acoustic waves resembling to the A0 mode and shows the features of variations in TOF due to extensional stress. The results shown here are only applicable under limitations given at the start of this modeling and are verified by the following experimental results (figure 12).

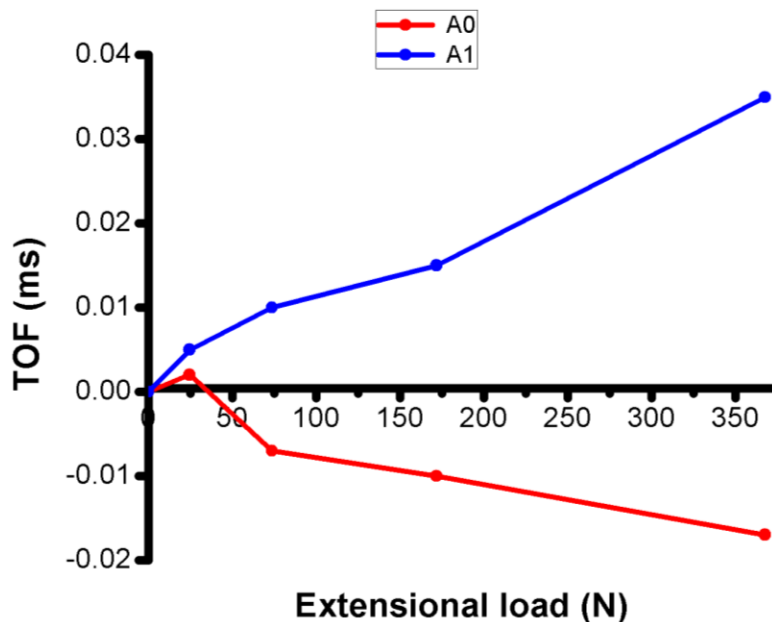


Figure 12: The plotted graph shows the experimental results [9] for two separate anti-symmetric modes of an aluminum (1 mm thick) strip being loaded with blue line showing A1 mode at frequency range of 1 MHz to 3 MHz, and red line showing A0 mode at lower frequency range of 10 kHz to 220 kHz with circular dots as measured data points.

After the initial jump in the measured data (red) line for A0 mode having a frequency range between 10 kHz to 220 kHz, the rest of the line shows an almost consistent declining feature in TOF with increasing load on aluminum strip. The second measured data (blue) line is not generated in the lower frequency range (between 1 MHz to 3 MHz), shows a different behavior upon extensional stress and so is not the subject of our discussion. The extension of the rotational springs will effectively not change the linear displacement (assuming very small angles of deviations), but the velocity will increase at low frequencies (refer to figure 11) with the increase of extensional stress, which will ultimately result in the decrease of TOF. The argument presented here is restricted to the idealized (or harmonic) conditions assumed here for a simple representation of the solid materials.

In reality there are factors involved which can force the material to deviate from its harmonic behavior, collectively called anharmonicity in the material. The next step in the development of this modeling is the incorporation of relativistic effects for the representation of anharmonicity in the material and its due reaction during the passage of bulk acoustic waves under variable stressed conditions.

3.2.3 Generalized vibrations

The harmonic vibrations occur when the force-arm's length connected to the torsional spring remains constant, but theoretically we can imagine the effects of anharmonicity due to variations in the force-arm's length (an extension or lengthening of the force-arm). Here we can contribute three limited cases of force-arm's length variations due to

extensional sideways force in which the effects of anharmonicity can be studied, starting from the position with no extension in the force-arm's length, with 1st and 2nd- step extensions, also shown in the figure 13.

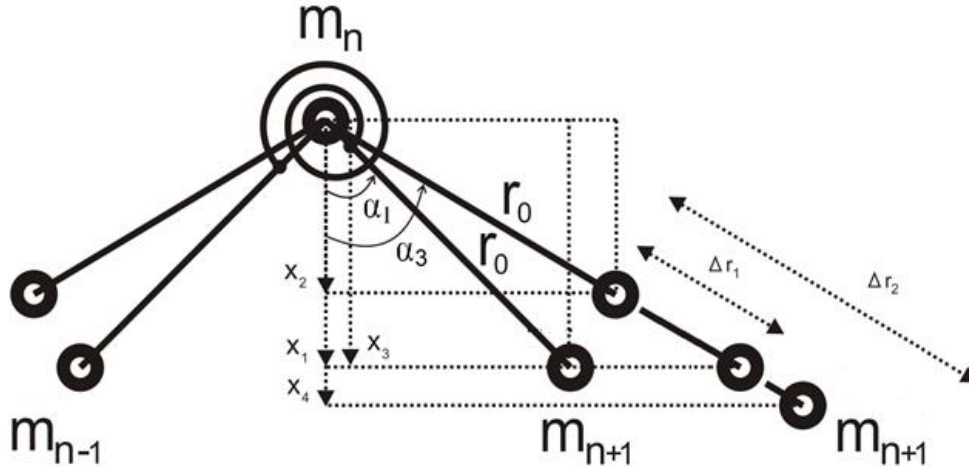


Figure 13: A mass-spring coupling system for T-mode vibrations with the application of extensional force including stepwise increased anharmonic effects represented by the increased force-arm's length.

The generalized equation of transversally polarized lattice displacement function (amended from equation 23) to include modeled anharmonicity effects can be written as following:

$$a_{GF} = r_{GF} \cdot \cos(\alpha_3) \quad (32)$$

and

$$r_{GF} = (r_0 + \Delta r) \quad (33)$$

where

GF 'Stands for GENERALIZED FUNCTION including anharmonicity'

a_{GF} = Generalized transversely polarized displacement function

r_{GF} = Generalized force-arm's length

r_0 = Original force-arm's length without extension

Δr = Increased part in the force-arm's length

The dispersion relation of transversally polarized vibrations (denoted by equation 24) can now be amended to:

$$\omega_{GF} = 2/a_{GF} \cdot (G/m)^{1/2} \cdot \sin(k \cdot a_{GF}/2) \quad (34)$$

This generalized stress affected dispersion relation (34) including (modeled) anharmonicity can be discussed in three basic limiting cases as following:

Case (1):

The 1st case, in which no anharmonicity is assumed in the material, means there would be no variation in the length of force-arm due to extensional force applied. The lattice displacement function in this case will be x_2 (figure 13). The equation (32) would become

$$x_2 = r_0 \cdot \cos(\alpha_3) \quad (35)$$

If we represent this displacement function (with no increase in force-arm's length) by a_{GF0} , then equation (35) can be written as:

$$a_{GF0} = r_0 \cdot \cos(\alpha_3) \quad (36)$$

The amended dispersion relation (according to equation 34) in this case can be written as following:

$$\omega_{GF0} = 2/a_{GF0} \cdot (G/m)^{1/2} \cdot \sin(k \cdot a_{GF0}/2) \quad (37)$$

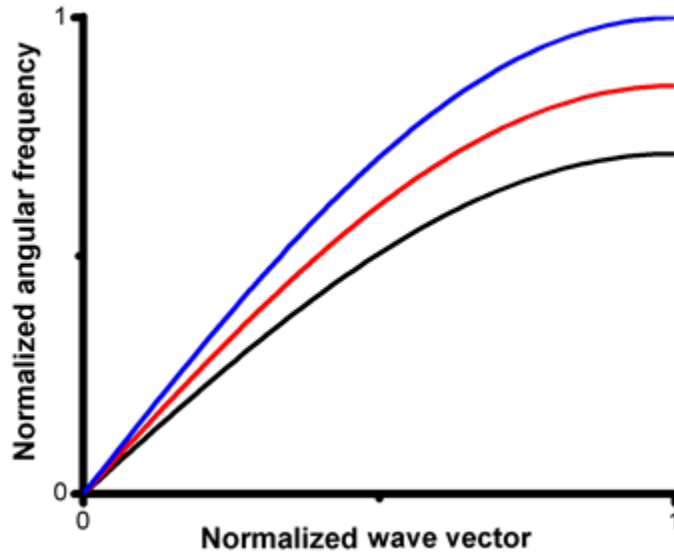


Figure 14: A force dependent graphical representation of dispersion relation (equation 37) without anharmonicity (the resulted graph will be the same as in figure 11). Here the black, red, and blue color lines represent the effects of single, double and triple units of extensional pulling forces respectively applied to the mass-spring chain.

The resultant TOF (according to equation 29) in this specific case at lower frequencies (i.e. $k \rightarrow 0$) will be

$$\text{TOF} = a_{GF0} \cdot (m/G)^{1/2} \quad (38)$$

As the term (m/G) is assumed to be a constant value in the model, the equation (38) can be represented as:

$$\text{TOF} \approx a_{GF0} \quad (39)$$

The function value of a_{GF0} will be decreasing (according to equation 36) as the angle of cosine is increasing due to extensional pull. Thus equation (38) concludes that in a transversely polarized acoustic mode with no anharmonicity, the TOF will decrease due to sideways extensional force.

Case (2):

In the 2nd case, the anharmonicity is assumed to be present in the material, and the variation in the force-arm's length due to extensional force is supposed to be such that the lattice displacement function x_3 (shown in figure 13) becomes equal to x_1 i.e.

$$x_3 = x_1$$

where

$$x_3 = (r_0 + \Delta r_1) \cdot \cos(\alpha_3)$$

If we represent this displacement function x_3 by a_{GF1} , then

$$a_{GF1} = (r_0 + \Delta r_1) \cdot \cos(\alpha_3) \quad (40)$$

The amended dispersion relation (according to equation 34) in this case can be written as:

$$\omega_{GF1} = 2/a_{GF1} \cdot (G/m)^{1/2} \cdot \sin(k \cdot a_{GF1}/2) \quad (41)$$

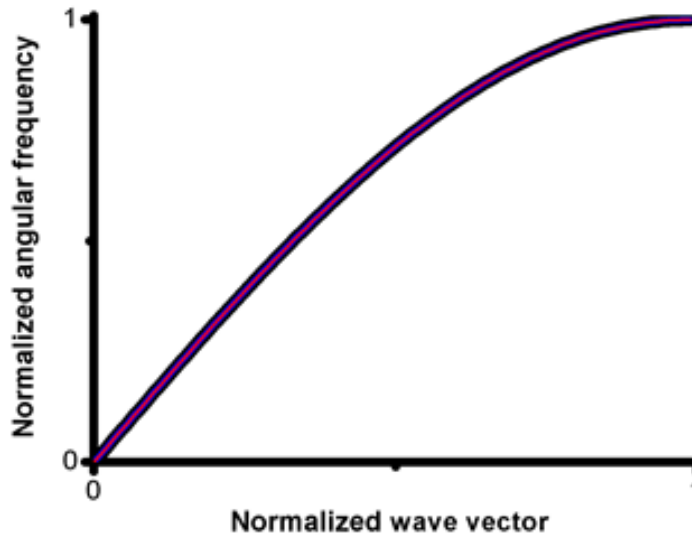


Figure 15: A force dependent graphical representation of dispersion relation (equation 41) with modeled anharmonicity present in the material such that the TOF remains constant for any extensional stress. Here all of the overlapped color lines (i.e. black, red, and blue) represent the effects of single, double and triple units of extensional pulling forces applied to the mass-spring chain.

The resultant TOF (according to equation 29) in this specific case at lower frequencies (i.e. $k \rightarrow 0$) will be

$$\text{TOF} = a_{GF1} \cdot (m/G)^{1/2} \quad (42)$$

$$\text{TOF} \approx a_{GF1} \quad (43)$$

The function value a_{GF1} remains constant with the simultaneous increase of deflection angle α_3 and force-arm's length. The equation (42) represents the relative effect of anharmonicity on TOF. This means even if the extensional force should decrease the TOF, but due to anharmonic effect (i.e. enlargement of force-arm), the TOF is compensated such that it becomes the same as was before the application of extensional force.

Case (3):

In the 3rd case, the anharmonicity is present in the material, and the variation in the force-arm's length due to extensional force is supposed to be such that the lattice displacement function x_4 (figure 13) becomes greater than x_1 i.e.

$$x_4 > x_1$$

where

$$x_4 = (r_0 + \Delta r_2) \cdot \cos(\alpha_3)$$

If we represent this displacement function x_4 by a_{GF2} , then

$$a_{GF2} = (r_0 + \Delta r_2) \cdot \cos(\alpha_3) \quad (44)$$

The amended dispersion relation (according to equation 34) in this case can be written as:

$$\omega_{GF2} = 2/a_{GF2} \cdot (G/m)^{1/2} \cdot \sin(k \cdot a_{GF2}/2) \quad (45)$$

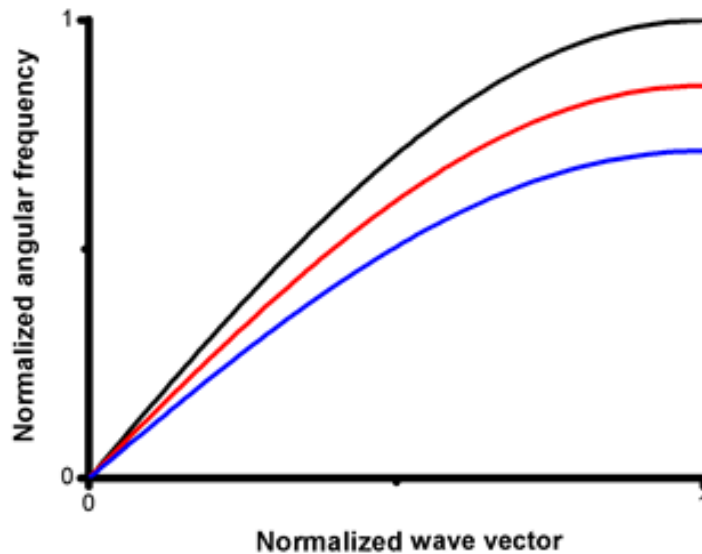


Figure 16: A force dependent graphical representation of dispersion relation (equation 45) with modeled anharmonicity present in the material such that the TOF is increased due to increased anharmonic effects resulting in the decrease of velocity as clear from the above graph. The color scheme showing black, red, and blue color lines represents the effects of single, double and triple units of extensional pulling forces respectively applied to the mass-spring chain.

The resultant TOF (according to equation 29) in this specific case at lower frequencies (i.e. $k \rightarrow 0$) will be

$$\text{TOF} = a_{GF2} \cdot (m/G)^{1/2} \quad (46)$$

$$\text{TOF} \approx a_{GF2} \quad (47)$$

The function value a_{GF2} increases with the simultaneous increase of deflection angle α_3 and force-arm's length. The equation (46) represents the relative effect of anharmonicity on TOF. Even though the extensional force should decrease the TOF, but due to the larger anharmonic effect, the total TOF is compensated such that it becomes increasing.

3.3 combined (L + T) -mode vibrations

The microscopic approach is used here to develop a unified (or combined treatment) linear chain mass-spring model to investigate the stress effects on longitudinally and transversely polarized modes of bulk acoustic waves.

The model [14] has used the TOF as a parameter to monitor the variations due to stress in the ultrasonic waves. The model provides a sufficient separation of longitudinal and directional acting restoring forces to allow a simple treatment of the relevant wave equations. The provided analysis could qualitatively predict the observed effects of extensional load on TOF for shear acoustic waves and the effects on the TOF variation observed for longitudinally polarized acoustic waves. The results obtained here are simultaneously compared with the individual models presented above and are found in good agreement.

3.3.1 Lattice dynamic modeling

To develop a model representing the combined treatment including longitudinal and transversal polarized behavior of mechanical waves upon extensional pull, an infinitely long chain can be represented by a point mass m at an arbitrary position n along with its two neighbors at $n+1$ and $n-1$ in the chain (figure 17). To get a rigidity for shear forces the directional forces or angle dependent torques are modeled by torsional springs acting on sideways directionally rigid connecting links. Springs acting freely only lengthwise allow a lengthening of the chain and respective longitudinally polarized propagating waves.

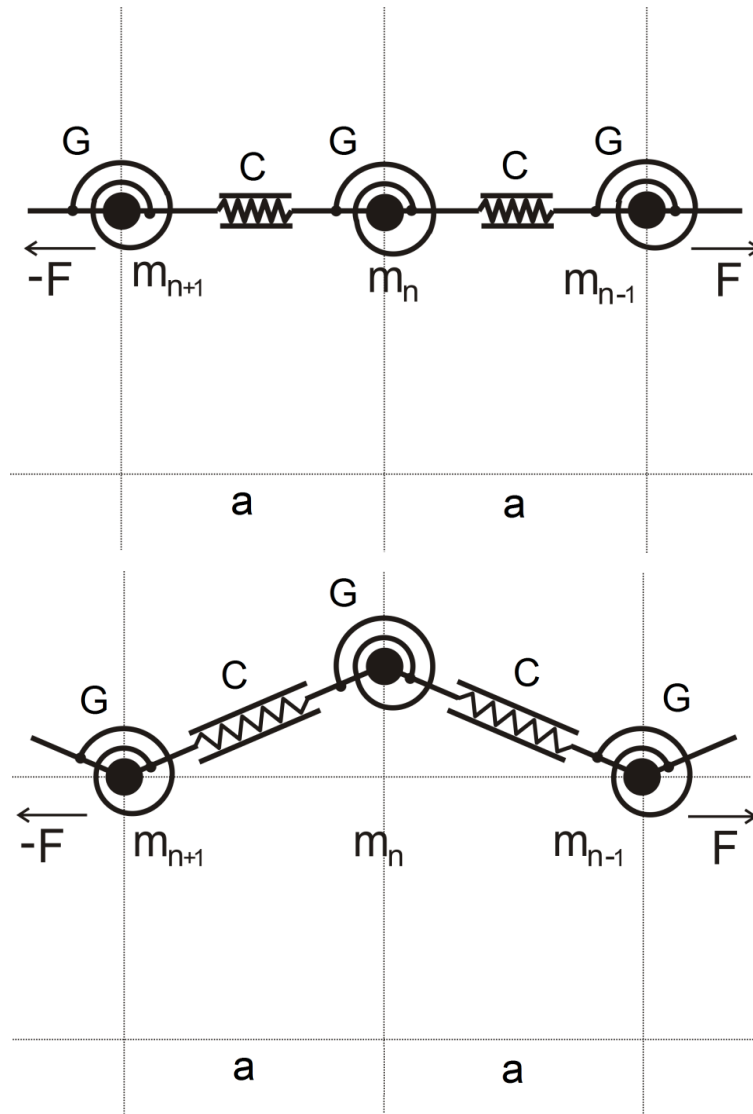


Figure 17: Mass-spring coupling system for a combined treatment of transversal and longitudinal polarized acoustic waves. F represents extensional stress applied externally to the linear chain. G is the stiffness coefficient of the rotational springs and represents the shear stiffness if only first neighbor interaction is considered; C is Hooke's spring coefficient representing the lateral stiffness, and a is the lattice displacement between the mass points (m_i ; $i = n, n+1, n-1, \dots$). Any lateral displacement shown here for substantial dislocations will be assumed to be negligibly small in the calculations treating the model. The first (top) figure shows the system in equilibrium and the second (bottom) figure shows the same system in the stressed form such that its lattice distance a remains the same.

The effect of angle dependent torque $\tau \sim (\alpha_{n+1} - \alpha_n)$ is equivalent to the shear stiffness that brings transversal force acting at the n th element

$$G/a^2 \cdot (y_{n+1} + y_{n-1} - 2y_n) \quad (48)$$

On the other hand the springs between the elements transfer the pulling force F that in case of the movement of the n th element out of the equilibrium by y_n creates the transversal restoring force

$$F/a \cdot (y_{n+1} + y_{n-1} - 2y_n) \quad (49)$$

In addition the lattice distance a becomes dependent on the external applied tensional stress represented by the force F according to:

$$a = a(F) = a_0 + F/C \quad (50)$$

Where C is the lateral spring coefficient as defined by Hooke's law and a_0 is the length of lattice unit without external force F .

3.3.2 Harmonic vibrations

In the mass-spring lattice model (MSLM) the basic features of the dispersion graphs can be derived by treating a unit of the chain which, if as assumed here for simplification only next neighbor forces are considered, consists of a mass at a selected position and the two next neighbor masses connected as demonstrated in figure 17. The simplification relates to a combination of waves in a sideways (2D or even 3D) infinitely extended point mass model.

The discrete wave equation in this case consists of inertial forces $\{m \cdot d^2y_n/dt^2\}$, the potential forces $\{G/(a^2) \cdot (y_{n+1} + y_{n-1} - 2y_n)\}$, and restoring forces $\{F/(a) \cdot (y_{n+1} + y_{n-1} - 2y_n)\}$ acting on the particle m_n . The equilibrium of these forces on the n th element leads to:

$$\begin{aligned} m \cdot d^2y_n/dt^2 - G/(a^2) \cdot (y_{n+1} + y_{n-1} - 2y_n) - F/(a) \cdot (y_{n+1} + y_{n-1} - 2y_n) &= 0 \\ d^2y_n/dt^2 - G/(ma^2) \cdot (y_{n+1} + y_{n-1} - 2y_n) - F/(ma) \cdot (y_{n+1} + y_{n-1} - 2y_n) &= 0 \\ d^2y_n/dt^2 - [G/(ma^2) + F/(ma)] \cdot (y_{n+1} + y_{n-1} - 2y_n) &= 0 \\ d^2y_n/dt^2 - [(G/a + F) / (ma)] \cdot (y_{n+1} + y_{n-1} - 2y_n) &= 0 \end{aligned} \quad (51)$$

The wave equation derived in that way is a general second order differential equation. It can be shown that the solution of that equation (51) will have a form of sinusoidal dispersion relation, but the sensitivity of the dispersion relation to the external pull depends on the inter-relation between the elastic coefficients G and C involved in the model. By proper selection of parameters concerning the general solution [appendix 3.4] of equation (51), the following equation is obtained:

$$\omega = 2 \cdot [(G/a + F) / (ma)]^{1/2} \cdot \sin(k \cdot a/2) \quad (52)$$

Here k represents the wave vector and lattice displacement is the function of applied stress such that $a = a(F) = a_0 + F/C$.

3.3.3 Generalized vibrations

Since the small amplitude and respectively small angle approximation is involved in the combined treatment of longitudinal and transversal vibrations, the dependence of TOF

with variable factors can be treated. Below some of the representative (discrete limiting) cases are discussed.

Case (1):

Suppose the shear stiffness G in the material has a finite fixed value (between zero and infinity) and the lateral stiffness C is very high (i.e. infinite) such that the distance between the chain elements does not elongate under any pulling force F . Then the dispersion relation (52) can be expressed by:

$$\omega_F = 2 \cdot \left((G/a_0 + F) / ma_0 \right)^{1/2} \cdot \sin(k \cdot a_0/2) \quad (53)$$

The group and phase velocities in the limit $k \rightarrow 0$ can both be represented by V

$$V = a_0 \cdot \left((G/a_0 + F) / ma_0 \right)^{1/2} \quad (54)$$

The time-of-flight needed to pass the lattice distance a_0 can also be given as:

$$\text{TOF}a_0 = a_0 / V \quad (55)$$

Evaluating equation (54) into equation (55)

$$\text{TOF}a_0 = \left(ma_0 / (G/a_0 + F) \right)^{1/2} \quad (56)$$

In the absence of a pulling force, the TOF will be constant as the stiffness coefficient is assumed here a fixed value. The presence of a pulling force will affect the TOF such that it will decrease for harmonic vibrations. This effect has been observed for the lowest anti-symmetric mode in the following experimental result which resembles the here treated transversely polarized acoustic modes (figure 18).

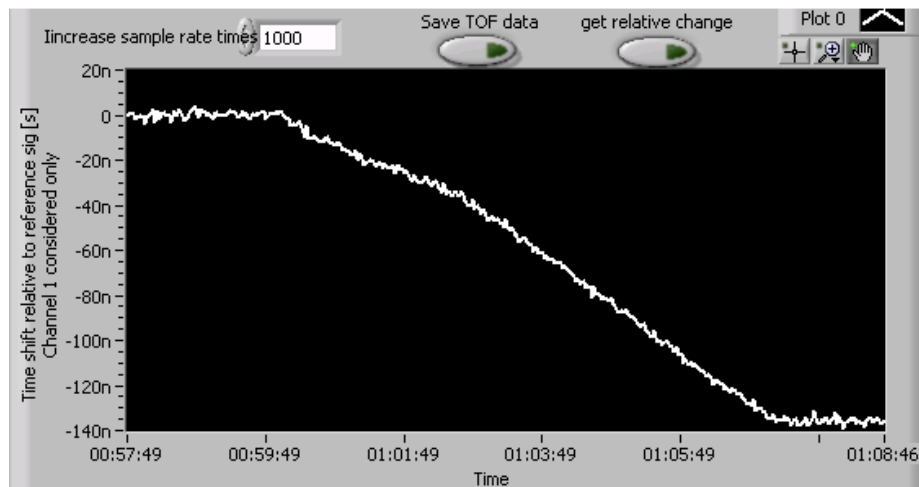


Figure 18: Live software view showing a runtime loading of aluminum (1 mm thick) strip from 01:00:10 till 01:06:20 (in time scale) with a loading rate of 5.4 kg per minute. The anti-symmetric A0 mode with a frequency range of 10°kHz to 220°kHz has been observed and has shown a decreasing feature in TOF with increasing extensional load.

Case (2):

Suppose there is no shear stiffness (i.e. $G = \text{zero}$) and the lateral stiffness C is very high (i.e. infinite) such that the distance between the chain elements does not change under any pulling force F . Then the dispersion relation (equation 52) can now be written as:

$$\omega_F = 2 \cdot [F / (ma_0)]^{1/2} \cdot \sin(k \cdot a_0 / 2) \quad (57)$$

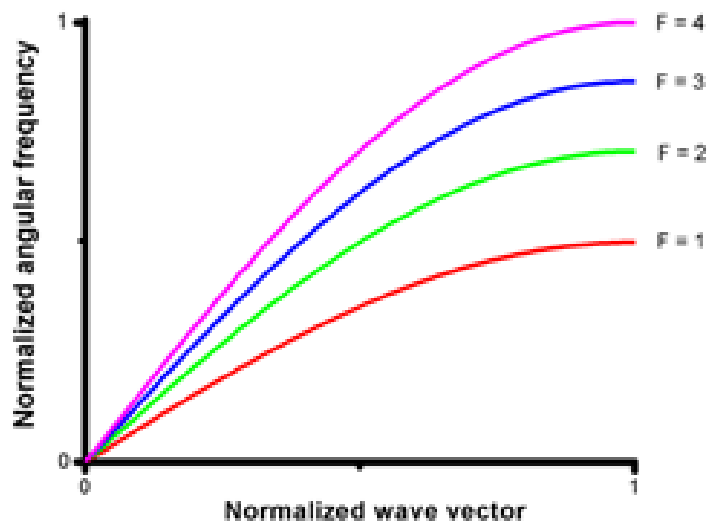


Figure 19: The plotted graph represents the dispersion dependence on the pulling force for a linear mass-spring chain without any shear stiffness and infinite longitudinal stiffness within the normalized parameters. The respective pulling forces are shown in colors from red, green, blue, magenta for a single, double, triple, and quadruple units of lengthwise pulling forces applied to the chain.

The technically relevant applications on which this chapter is concentrating relates for a microscopic interpretation where a_0 represents inter-atomic distances to the large wavelengths limit ($k \rightarrow 0$). In that case, group and phase velocities are equal which allows representing both by V and is given by:

$$V = a_0 \cdot (F / ma_0)^{1/2} \quad (58)$$

This means that in the absence of sideways pulling forces the velocity becomes zero, and will increase proportionally to the square root of pulling forces applied. The derived equation can further be transformed as:

$$V = (F / (m/a_0))^{1/2} \quad (59)$$

Here (m/a_0) is the linear mass density and F is the magnitude of the pair of external forces supplying the pull. This equation is already well known from the derivation of the velocity of transverse polarized mechanical waves traveling on an extensional stiff but concerning bending soft string [15] (idealized chain). For such a string or chain the velocity of mechanical waves v is given by:

$$v = \sqrt{T/\mu} \quad (60)$$

With T representing the tension (axial stress) and μ representing the mass per unit length of the string, this is in full accordance with the assumed simplified case treated above.

The resultant TOF derived for lattice displacement a_0 can then be written (from equation 58) as following:

$$\text{TOF} = (ma_0 / F)^{1/2} \quad (61)$$

The TOF is decreasing upon the increase of extensional forces under the condition that lattice is not elongating.

Case (3):

Suppose that a shear stiffness value G is present in the material (between zero and infinity) and also the lateral stiffness C has a value (between zero and infinity) such that the distance between the chain elements elongates under any pulling force F . The dispersion relation (equation 52) can now be written as:

$$\omega_F = 2 \cdot ((G/a + F) / (ma))^{1/2} \cdot \sin(ka/2) \quad (62)$$

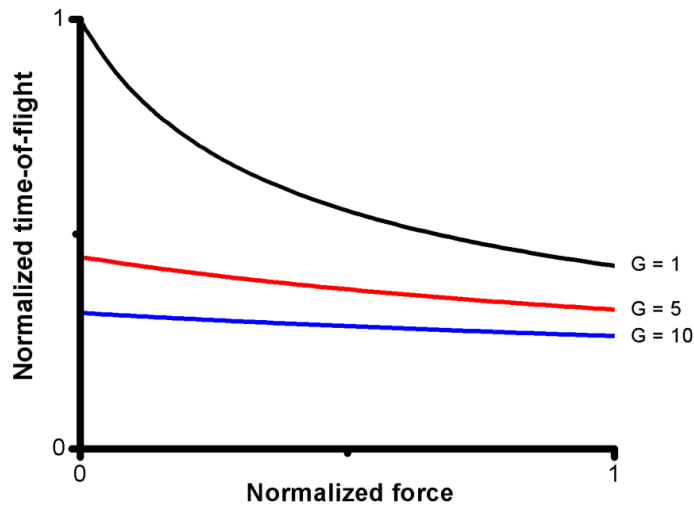


Figure 20: The plotted graph represents the dispersion dependence on the pulling force for a linear mass-spring chain with three different values of shear stiffness and infinite longitudinal stiffness within the normalized parameters at long wavelengths regime. The effects on the TOF with respective shear stiffness values ($G = 1$, $G = 5$, $G = 10$) are shown as black, red and blue colors respectively.

The group and phase velocities in the long wavelengths limit ($k \rightarrow 0$) are represented by:

$$V = a \cdot ((G/a + F) / ma)^{1/2} \quad (63)$$

The TOF needed to pass for the resultant lattice displacement a can be expressed by:

$$\text{TOF}_a = (ma / (G/a + F))^{1/2} \quad (64)$$

The equation (64) formulates the resulted TOF for a combined treatment of bulk acoustic modes at long wavelengths propagating under defined stressed conditions in an extendable chain of lattice unit a .

The graph (figure 20) clearly represents the difference of TOF behavior upon changing the value of shear stiffness G . The model actually can represent a combination of (lateral and transversal) vibrations such that the dominant part of it will dictate the TOF of the propagating bulk acoustic waves at longer wavelengths. For example for smaller shear stiffness ($G = 1$) and infinite longitudinal stiffness (i.e. $C = \infty$), the TOF is decreasing in nature and represents the resemblance to the results [16] obtained for lowest anti-symmetric propagating acoustic mode under stress. Similarly with the increased shear stiffness (e.g. $G = 10$) and infinite longitudinal stiffness (i.e. $C = \infty$), the effects on TOF compensate such that its nature with the increase of extensional stress becomes constant. This result resembles to the gradual loading response of lowest symmetric acoustic mode in which the TOF remains nearly constant.

The theoretical predictions concerning TOF variations of this model for both low frequency symmetric and anti-symmetric acoustic modes are verified by the experimental results shown in figure 21.

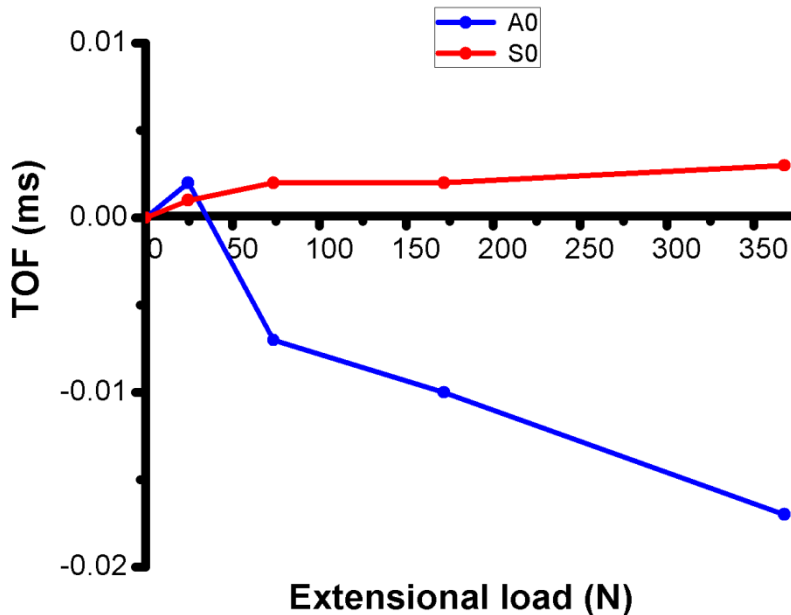


Figure 21: The plotted graph showing the experimental results [9] at low frequencies for symmetric and anti-symmetric modes. The dominant feature for A0 mode with frequency range between 10 kHz to 220 kHz is a decline in the TOF, whereas for the S0 mode with frequency range between 100 kHz to 200 kHz in comparison is almost constant TOF observed under increasing load on the aluminum (1 mm thick) strip.

The developed unified mass-spring linear chain model has demonstrated individually and in combination the expected effects of extensional stress on longitudinal and transverse polarized acoustic modes in form of dispersion relations of wave velocities and their respective TOFs.

3.4 Comparison of L-mode and T-mode vibrations

A comparison of velocity and TOF equations for L-mode and T-mode vibrations is given as following:

Velocity at long wavelength limit

In the long wavelength limit ($k \rightarrow 0$), group and phase velocities of transversally polarized acoustic waves (according to eq. 27) are identical and can both be given as:

$$V_T = (G/m)^{1/2} \quad (65)$$

Similarly for longitudinal polarized acoustic waves, group and phase velocities are identical (according to eq. 7) in the long wavelength limit ($k \rightarrow 0$) and can both be given as:

$$V_L = a \cdot (C/m)^{1/2} \quad (66)$$

As we know generally the transversal velocity V_T of acoustic waves [17] is two third of the longitudinal velocity V_L of the acoustic waves. Then we can write an equation as:

$$V_T = 2/3 \cdot (V_L) \quad (67)$$

Using values from equations (65) and (66) in equation (67), we get

$$(G/m)^{1/2} = 2/3 \cdot a \cdot (C/m)^{1/2} \quad (68)$$

$$G = 4/9 \cdot C \cdot a^2 \quad (69)$$

$$C = 9/4 \cdot G/a^2 \quad (70)$$

The above equation gives us the value of C in terms of G.

Time-of-flight (TOF) at long wavelength limit

In the long wavelength limit (i.e. $k \rightarrow 0$), the time-of-flight (TOF_T) for transversally polarized acoustic waves (according to equation 29) can be defined as:

$$TOF_T = a (m/G)^{1/2} \quad (71)$$

Using the value of G in terms of C (according to equation 69), we get

$$TOF_T = 3/2 \cdot (m/C)^{1/2} \quad (72)$$

Here (m/C) is a constant term for harmonic conditions,

$$TOF_T = \text{constant} \quad (73)$$

Also the time-of-flight (TOF_L) for longitudinally polarized acoustic waves (according to equation 9) at longer wavelengths is given by:

$$TOF_L = (m/C)^{1/2} \quad (74)$$

and this also is a constant term for harmonic conditions,

$$TOF_L = \text{constant} \quad (75)$$

The result of comparison shows that the above presented (in section 3.3) mass-spring linear chain model can be used as a representative unified model for longitudinal and transversal acoustic modes within harmonic and low frequency conditions.

3.5 Summary

The mass-spring linear chain modeling has been employed here to demonstrate the effects of extensional force on TOF for two basic modes of acoustic waves namely symmetric and anti-symmetric at low frequencies (or long wavelengths). The two individual and a combined models have demonstrated the theoretical results in the form of solved dispersion relations for longitudinally and transversally polarized (resembling low frequency symmetric and anti-symmetric modes of) acoustic waves. Generally the prominent feature of the longitudinally polarized (or L-mode) acoustic waves is that the TOF will remain constant for harmonic (or idealized) vibrations at low frequencies under the influence of extensional stress. In that case anharmonic effects are needed to describe any observed variations in the experimentally achieved results of the TOF. Different to the case for longitudinal polarization, transversally polarized (or T-mode) acoustic waves will exhibit a variation of TOF under external stress even in the absence of anharmonicities. As the real materials contain anharmonicity, a further step of investigation is conducted to include anharmonicity factor in these models and is represented by generalized vibrations. The here achieved modeling results have been compared with the corresponding experimental results and are found in good agreement.

3.6 References

- [1] Karl F. Graaf, "Wave motion in elastic solids", Reprint of Oxford 1975 edition, ISBN 978-0-486-66745-4, (1991)
- [2] Fritz K. Kneubühl, "Oscillations and waves", Springer, ISBN 3-540-62001-X, (1997)
- [3] A. D. D. Craik, "The origins of water wave theory", Annual Review of Fluid Mechanics 36, (2004)
- [4] L. W. Michael, D. Rubin, E. Krempl, "Introduction to Continuum Mechanics", 3rd edition, (1996)
- [5] K. S. Tarar, R. Meier, U. Amjad, and W. Grill, "Stress detection with guided acoustic ultrasonic waves by nonlinear elastic and geometric effects", SPIE Proc. 729518, (2009)

- [6] K. S. Tarar, U. Amjad, and W. Grill, "Lumped circuit mechanical models and lattice dynamics approach to the dependence of the time-of-flight of bulk and guided acoustical modes on elongation", Proc. SPIE 76500I, (2010)
- [7] Charles Kittel, "Introduction to solid state physics", Published by John Wiley and Sons, 8th edition, (2008)
- [8] Robert Hooke, "Ut tension, sic vis, (meaning: as the extension, so the force)", (1678)
- [9] K. S. Tarar, W. Grill, "Linear chain lattice dynamics approach to the dependence of the time-of-flight of acoustical modes on stress and strain", (article in preparation for publication)
- [10] P. M. Morse, "Diatomic molecules according to the wave mechanics II: Vibrational levels", Phys. Rev. 34, pp. 57-64, (1929)
- [11] J. E. Lennard-Jones, "On the determination of molecular fields", Proc. Roy. Soc. London A 106 (738), pp. 463–477, (1924)
- [12] V. B. Bhandari, "Design of machine elements", Tata-McGraw-Hill Publishers, 2nd edition, (2007)
- [13] Isaac Newton, "Mathematical Principles of Natural Philosophy", English translation based on 3rd Latin edition 1726, volume 1, containing Book 1, especially at the section Axioms or Laws of Motion starting page 19, (1729)
- [14] K. S. Tarar, M. Pluta, U. Amjad, W. Grill, "Lattice dynamics approach to determine the dependence of the time-of-flight of transversal polarized acoustic waves on external stress", Proc. SPIE 79842R, (2011)
- [15] T. C. A. Molteno, N. B. Tufillaro, "An experimental investigation into the dynamics of a string II", American Journal of Physics 72 (9), pp. 1157–1169, (2004)
- [16] U. Amjad, D. Jha, K. S. Tarar, H. Klinghammer, and W. Grill, "Determination of the stress dependence of the velocity of Lamb waves in aluminum plates", Proc. SPIE 798410, (2011)
- [17] G. Hartwig, "Polymer properties at room and cryogenic temperatures", Published by Springer, (1994)

4. Developed theory for guided acoustic waves

The linear chain mass-spring model [1] has been used here to demonstrate the combined effects treating longitudinal and transversal modes on propagating guided acoustic (Lamb) waves under extensional stress for isotropic homogeneous solid-state media. A comparison of physical parameters between continuum and discrete models is performed. Also included is an analytical investigation of the theoretical modeling to the experimentally achieved results. The theoretical and experimental results are compared and discussed in detail in this chapter.

The theoretical description employed here as linear chain model originates from lattice dynamics [2-5]. They can also be interpreted as mechanical lumped circuits. Since the chain elements relate to finite elements, the approach is also well suited for computational methods. The interaction of atoms is traditionally described by suitable potential forces. Concerning the forces relevant for the adjustment of the distance of neighboring atoms, the Lennard-Jones [6] and the Morse-Feshbach potentials [7] are historically relevant examples. The detection of variations of the time-of-flight (TOF) of acoustic waves for different modes propagating in solid plates is one of the numerous methods developed for that purpose. Different levels of sensitivity of the TOF for fundamental symmetric and anti-symmetric Lamb wave modes for such parameters as applied stress or temperature, allows the need for a selective determination of each of them. The modeling of lowest anti-symmetric (A0) Lamb wave mode is given preference due to its higher sensitivity to the external stress [8].

The given model [1] has provided an extension of the already available literature [9-10] in solid state physics. The advantage of this tool over Lamb wave equations is the direct submission capability of stress parameters and the hereby achieved relevant dispersion relations, especially the monitoring of TOF of propagating guided acoustic waves with respect to the material (in our case aluminum alloy). Here a further extension to this modeling has been provided by introducing detailed analytical investigation of theoretical results and their comparison with experimental results.

4.1 Derivation of the model

The presented research extends a lattice dynamics based theory [2] for the modeling of Lamb waves in pseudo-elastic solid material to exemplify the effects caused by stress and anharmonicity measured with Lennard-Jones interatomic binding potential and are compared with the experimental findings [11].

4.1.1 Lattice dynamic modeling

Consider a one dimensional linear chain model [1] under externally applied pull (force) consisting of equal distanced point masses that interacts with their neighbors (figure 1).

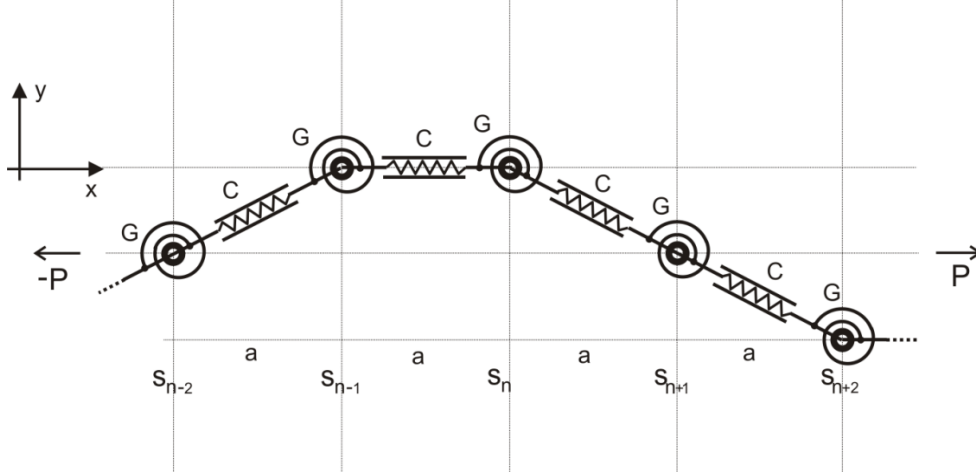


Figure 1: Linear mass-spring coupling system [1] at a fixed time in a non-equilibrium position for a combine treatment of the longitudinal (L-mode) and transverse (T-mode) polarized acoustic waves. Here P represents the magnitude of a pair of pulling forces describing the externally applied stress. Rest of the symbols are defined in the text.

Besides of the interaction by linear mass-free and sideways stiff linear springs, characterized by the spring constants C , also torsional springs, represented by G , are introduced. In the absence of external forces the position of the n -th element of the chain is $s_n = na_0$. In the here applied two dimensional model, the force exerted on the n -th element of the chain consists of the components parallel to the chain (in x -direction) and another orthogonal to the chain (in y -direction).

4.1.2 Sideways force dynamics

Concerning the dynamics of the chain, the parallel force component between neighbors can be expressed as $F_C^{i,i+1} = -F_C^{i+1,i} = C \cdot (x_{n+1} - x_n)$, where x_n is the horizontal component of the n -th element's displacement. The formula for the parallel force leads to the discrete wave equation with the dispersion relation [2]:

$$\omega = 2\sqrt{C/m} \left| \sin\left(\frac{1}{2}ka\right) \right| \quad (1)$$

Where ω - angular frequency and k is the wave number. At lowest frequency limit, the phase and group velocities are equal to $V = a\sqrt{C/m}$.

4.1.3 Perpendicular force dynamics

The vertically acting restoring force, related to the extensional pull P is given by:

$$F_{\perp}^P = (y_{n+1} - y_n) \cdot P/a - (y_n - y_{n-1}) \cdot P/a = (y_{n+1} + y_{n-1} - 2y_n) \cdot P/a \quad (2)$$

In addition to this force, at non-equilibrium state, the rotational springs with spring constant G supply a torque $M_n = G \cdot (\alpha_{n+1} - \alpha_n)$, with α_i denoting angular deviation of

inter-connecting sectors from equilibrium. It is assumed that the mechanical oscillation is limited to sufficiently small amplitudes. It has already been shown [1] that the presence of the rotational springs leads to the vertical force acting on the n-th element in the form:

$$F_{\perp}^G = G \cdot \left\{ \frac{-y_{n-2} + 4y_{n-1} - 6y_n + 4y_{n+1} - y_{n+2}}{a^2} \right\} \quad (3)$$

That force depends not only on the position of the next but also on the second next neighbor point masses.

4.1.4 Dispersion relation

Substituting both vertical force components (equations 2 and 3) to the equation of motion and by solving the resultant wave equation, the dispersion relation [1] for transversely polarized acoustic wave is obtained as following:

$$\omega = \sqrt{\frac{(2Pa + 6G) - (2Pa + 8G)\cos(ka) + 2G\cos(2ka)}{ma^2}} \quad (4)$$

The above dispersion relation allows the determination of phase and group velocity and consequently the TOF of propagating acoustic waves. Theoretical results derived from equation (4) are comparable to the lowest anti-symmetric (A0) guided acoustic mode. The case of linear inter-atomic dependence of $a = a_0 + P/C$ on extensional force has already been discussed by the author in literature [9]. Here the anharmonicity derived from Lenard-Jones potential in the form of distance-to-force relation is introduced.

4.1.5 Respective physical parameters derived from the model

The phase $V(\text{ph})$ and group $V(\text{gr})$ velocities for the dispersion relation (equation 4) are defined as:

$$V(\text{ph}) = \omega / k$$

$$V(\text{ph}) = \frac{1}{k} \cdot \left\{ \sqrt{\frac{(2Pa + 6G) - (2Pa + 8G)\cos(ka) + 2G\cos(2ka)}{ma^2}} \right\}$$

And for

$$V(\text{gr}) = d\omega/dk$$

$$d\omega/dk = \frac{1}{(ma^2)^{1/2}} \cdot d/dk \left[(2Pa + 6G) - (2Pa + 8G) \cdot \cos(ka) + 2G \cdot \cos(2ka) \right]^{1/2}$$

Here m and a are non-variables, because the derivative is performed with respect to wave number k only

$$V(\text{gr}) = \frac{1}{(m)^{1/2}} \cdot [(2Pa + 6G) - (2Pa + 8G) \cdot \cos(ka) + 2G \cdot \cos(2ka)]^{1/2} \cdot [(Pa + 4G) \cdot \sin(ka) - 2G \cdot \sin(2ka)]$$

$$V(\text{gr}) = \frac{[(Pa + 4G)\sin(ka) - 2G\sin(2ka)]}{[\sqrt{m}] \cdot [\sqrt{(2Pa + 6G) - (2Pa + 8G)\cos(ka) + 2G\cos(2ka)}]}$$

The TOF for transit of one unit lattice a in the low frequency limit can be expressed as following:

$$\text{TOF} = \frac{a}{V(\text{gr})}$$

which in our case will be

$$\text{TOF} = \frac{\sqrt{ma^2}}{[(Pa + 4G) \cdot \sin(ka) - 2G \cdot \sin(2ka)]} \left[\sqrt{(2Pa + 6G) - (2Pa + 8G) \cdot \cos(ka) + 2G \cdot \cos(2ka)} \right]$$

The above equation is a generalized formula of TOF for the guided acoustic waves under variable loading (or stress) conditions.

4.1.6 Lennard-Jones potential and respective coefficients for aluminum

The nonlinear dependence of the inter-atomic distance on the applied pulling force is due to the non-quadratic behavior of the atomic binding potential as discussed by Lennard-Jones potential [12].

$$U_{\text{LJ}} = 4\varepsilon \left[\left(\frac{\sigma_{\text{Al}}}{a} \right)^{12} - \left(\frac{\sigma_{\text{Al}}}{a} \right)^6 \right]$$

Here U_{LJ} is the Lennard-Jones potential function, a -inter-atomic distance between point masses, and rest of the symbols are defined in the following text (see section 4.3). The respective force (F_{LJ}) and spring (C_{LJ}) coefficients derived from Lennard-Jones potential are defined [appendix 4.1] as following:

$$F_{\text{LJ}} = 24\varepsilon \left[2 \frac{(\sigma_{\text{Al}})^{12}}{(a)^{13}} - \frac{(\sigma_{\text{Al}})^6}{(a)^7} \right]$$

$$C_{\text{LJ}} = 144\varepsilon \left[4 \frac{(\sigma_{\text{Al}})^{12}}{(a)^{14}} - \frac{(\sigma_{\text{Al}})^6}{(a)^8} \right]$$

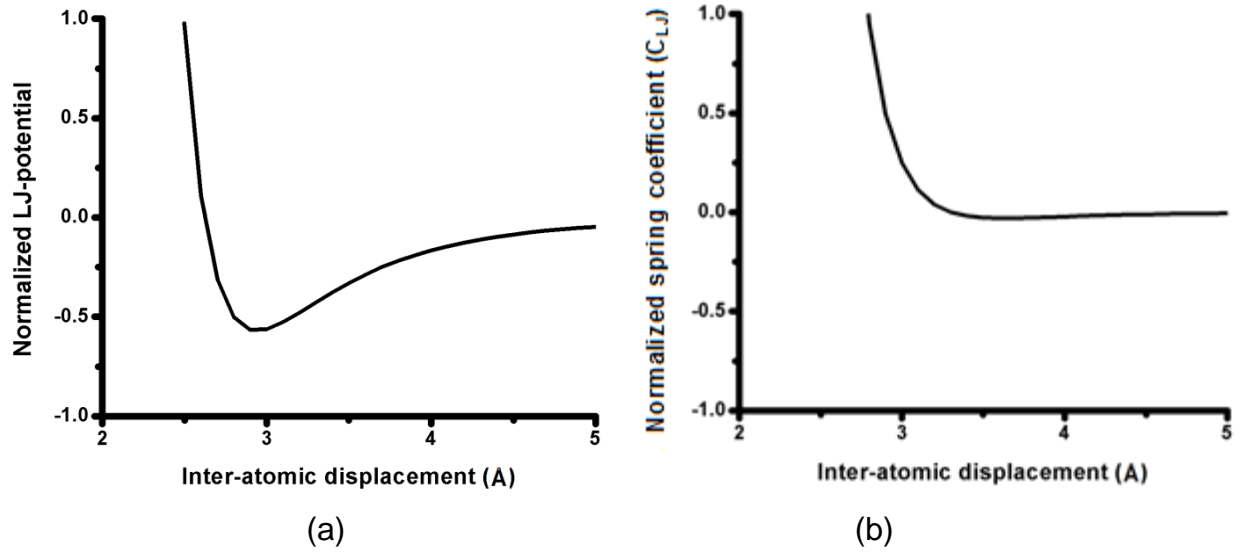


Figure 2: Interaction between aluminum atoms described by the Lennard-Jones potential: (a) Normalized plot of the LJ-potential, (b) Dependence of the relative spring coefficient (C_{LJ}) on the inter-atomic displacement Å (in angstrom).

As it is visible in the figure (2b), the relative spring coefficient (C_{LJ}) is strongly dependent [13] on the inter-atomic distance. The observed change of the TOF of lowest modes under applied pull occurs for both following reasons: (i) due to the change of sample length, (ii) due to the change in material elastic constant (i.e. Young's modulus).

4.2 Comparison of the frequency dependent physical parameters between continuum and discrete models

Here a comparison of frequency dependent physical parameters is provided between continuum (or elastic beam) and discrete (or mass-spring linear chain) models. The implementation conditions for both models are taken here such that to be valid only for low-frequency (or long wavelength) approximations.

The continuum model

Consider a transversal deformation of an elastic beam of cross-section S described by a second order differential equation [14]. The equation has been obtained after implementation of the influence of external extensional stress (pull) in the already available free beam model [15]. This result in

$$m \frac{\partial^2 \mathbf{u}}{\partial t^2} = T \frac{\partial^2 \mathbf{u}}{\partial x^2} - EI \frac{\partial^4 \mathbf{u}}{\partial x^4} \quad (5)$$

Where m is the mass per unit length of the beam, I is the second moment of the area, E is the Young's modulus, and T is the axial pulling force. The literature [14] also has provided a solution of the above equation (5) in the form of phase velocity as follows:

$$v_{ph} = \omega \sqrt{\frac{2EI}{\sqrt{T^2 + 4mEI\omega^2} - T}} \quad (6)$$

This equation (6) has further been solved [appendix 4.2] and has been obtained in the form of angular frequency for the continuum model as following:

$$\omega = \sqrt{\frac{Tk^2 + EI k^4}{m}} \quad (7)$$

An error is found in the literature [1] (for equation 7) and it has been corrected in the presented dissertation. As in this chapter we have used the notation m as mass, a as the length of lattice unit, and P as pulling force, so here in equation (7) by replacing $m = m/a$, $T = P$, we get

$$\omega = \sqrt{\frac{Pk^2 + EI k^4}{m/a}} \quad (8)$$

This is the resultant angular frequency (equation 8) for continuum model [14] in terms of extensional pulling force P .

The discrete model

The angular frequency equation obtained from discrete (or mass-spring chain) model [1] is given by:

$$\omega = \sqrt{\frac{(2Pa + 6G) - (2Pa + 8G)\cos(ka) + 2G\cos(2ka)}{ma^2}} \quad (9)$$

The above angular frequency equation (9) can be simplified by applying Taylor series expansion. By solving first three elements of suitable Taylor series for both cosines,

$$\cos(ka) \approx 1 - \frac{(ka)^2}{2} + \frac{(ka)^4}{24} \quad \text{and} \quad \cos(2ka) \approx 1 - \frac{(2ka)^2}{2} + \frac{(2ka)^4}{24}$$

in equation (9) leads to the following angular frequency equation

$$\omega = \sqrt{\frac{(2Pa + 6G) - (2Pa + 8G)\left\{1 - \frac{(ka)^2}{2} + \frac{(ka)^4}{24}\right\} + 2G\left\{1 - \frac{(2ka)^2}{2} + \frac{(2ka)^4}{24}\right\}}{ma^2}}$$

Modeling of guided acoustic waves

The series has been restricted to three elements only, due to the addition of increasingly very small elements, which would have a very small (or negligible) effect on the overall value of the function. The solution [appendix 4.3] of the above equation will give us:

$$\omega = \sqrt{\frac{Pk^2 + \left(Ga - \frac{Pa^2}{12}\right)k^4}{m/a}} \quad (10)$$

This is the angular frequency equation in simplified form (equation 10) for discrete model.

The comparison (between continuum and discrete models)

The comparison of both models along with their respective angular frequency equations (8 and 10) can be done by equating them as following:

$$\sqrt{\frac{Pk^2 + EIk^4}{m/a}} = \sqrt{\frac{Pk^2 + \left(Ga - \frac{Pa^2}{12}\right)k^4}{m/a}}$$

Squaring and solving [appendix 4.4] on both sides of the above equation,

$$EI = Ga - \frac{Pa^2}{12} \quad (11)$$

The equation (11) provides us elasticity modulus in terms of P, G and a. Also the value of G in this case would be

$$Ga = EI + \frac{Pa^2}{12}$$

Or

$$G = \left(EI + \frac{Pa^2}{12}\right) / a \quad (12)$$

This value of shear stiffness G (equation 12) is strictly limited towards diminishing inter-atomic displacements, loads and frequencies.

4.2.1 Velocity

It is a vector quantity which specifies the angular speed of an object and the axis about which the object is rotating.

The continuum model

In this case, the angular frequency (equation 8) obtained from continuum model [14] is:

$$\omega = \sqrt{\frac{Pk^2 + EIk^4}{(m/a)}}$$

And its phase velocity would be

$$v_{ph} = \frac{\omega}{k} = \frac{\sqrt{\frac{Pk^2 + EIk^4}{(m/a)}}}{k}$$

Or

$$v_{ph} = \frac{1}{k} \cdot \sqrt{\frac{Pk^2 + EIk^4}{(m/a)}} \quad (13)$$

After simplifying equation (13), we get

$$v_{ph} = \sqrt{\frac{P + EIk^2}{(m/a)}} \quad (14)$$

As we are interested in the parameters at low frequency or long wavelength limits. So by applying this limit (i.e. $k \rightarrow 0$), we get from equation (14)

$$v_{ph} = \sqrt{\frac{P}{(m/a)}} \quad (15)$$

This is the phase velocity at long wavelengths for continuum model.

And as the group velocity by definition is

$$v_{gr} = \frac{d\omega}{dk} = \frac{d}{dk} \left\{ \sqrt{\frac{Pk^2 + EIk^4}{(m/a)}} \right\} \quad (16)$$

After solving [appendix 4.5] the equation (16), we arrive at

$$v_{gr} = \left\{ \sqrt{\frac{1}{(m/a) \cdot (P + EIk^2)}} \right\} \cdot \{P + 2EIk^2\} \quad (17)$$

As we are interested in the parameters at long wavelength limits. So by applying this limit (i.e. $k \rightarrow 0$), we get from equation (17)

$$v_{gr} = \sqrt{\frac{P}{(m/a)}} \quad (18)$$

This is the group velocity at long wavelength limits for continuum model.

The discrete model

The angular frequency (equation 10) obtained from discrete model [1] is:

$$\omega = \sqrt{\frac{Pk^2 + \left(Ga - \frac{Pa^2}{12}\right)k^4}{(m/a)}}$$

And the phase velocity equation will be

$$v_{ph} = \frac{\omega}{k} = \frac{\sqrt{\frac{Pk^2 + \left(Ga - \frac{Pa^2}{12}\right)k^4}{(m/a)}}}{k}$$

Or

$$v_{ph} = \frac{1}{k} \cdot \sqrt{\frac{Pk^2 + \left(Ga - \frac{Pa^2}{12}\right)k^4}{(m/a)}} \quad (19)$$

After simplification the equation (19) would become

$$v_{ph} = \sqrt{\frac{\left\{P + \left(Ga - \frac{Pa^2}{12}\right)k^2\right\}}{(m/a)}} \quad (20)$$

Applying the long wavelength limits (i.e. $k \rightarrow 0$), we get from equation (20)

$$v_{ph} = \sqrt{\frac{P}{(m/a)}} \quad (21)$$

This is the phase velocity at long wavelength limits for discrete model.

Also for discrete model the group velocity equation will be

$$v_{gr} = \frac{d\omega}{dk} = \frac{d}{dk} \left\{ \sqrt{\frac{Pk^2 + \left(Ga - \frac{Pa^2}{12}\right)k^4}{(m/a)}} \right\} \quad (22)$$

After solving [appendix 4.6] the equation (22), we get

$$v_{gr} = \left\{ \frac{1}{\sqrt{(m/a) \cdot \left\{ P + \left(Ga - \frac{Pa^2}{12} \right) k^2 \right\}}} \right\} \cdot \left\{ P + 2 \left(Ga - \frac{Pa^2}{12} \right) k^2 \right\} \quad (23)$$

Applying the long wavelength limits (i.e. $k \rightarrow 0$), we get from equation (23),

$$v_{gr} = \left\{ \frac{1}{\sqrt{(m/a) \cdot \{P + 0\}}} \right\} \cdot \{P + 0\}$$

Or

$$v_{gr} = \sqrt{\frac{P}{(m/a)}} \quad (24)$$

This is the group velocity at long wavelength limits for discrete model.

The comparison (between continuum and discrete models)

The comparison of phase and group velocities for continuum and discrete models (equations 15, 18, 21, 24) shows their values at long wavelengths remain the same. This means that our assumption about phase and group velocity at long wavelengths to be a single accepted function, is valid!

4.2.2 Time-of-flight (TOF)

TOF is the measurement of time it takes for a particle or wave to travel a distance through a medium. In our case the TOF is the total time taken to cover the displacement unit length a . Thus

$$\text{TOF} = \frac{\text{Displacement}}{\text{Velocity}} \quad (25)$$

$$\text{TOF} = \frac{a}{v_g} \quad (26)$$

Here v_g is the group velocity. Because this approximation is intended for long wavelengths the overall choice of either phase or group velocity has not much difference on the TOF results.

The continuum model

The group velocity derived from continuum model (from equation 17) is:

$$v_{gr} = \left\{ \frac{1}{\sqrt{(m/a) \cdot (P + EI k^2)}} \right\} \cdot \{P + 2EI k^2\} \quad (27)$$

Applying the long wavelength limits (i.e. $k \rightarrow 0$),

$$v_{gr} = \sqrt{\frac{P}{(m/a)}} \quad (28)$$

Using this velocity equation (28) in TOF equation (26), we get

$$TOF = \frac{a}{\sqrt{\frac{P}{(m/a)}}}$$

Or

$$TOF = \sqrt{\frac{m \cdot a}{P}} \quad (29)$$

If the mass m and displacement a will remain unchanged, the TOF will decrease due to external pull P . This behavior of transversally polarized (resembling lowest anti-symmetric mode of) acoustic waves has also been shown in one of our experimental results discussed earlier (see chapter 3, figure 18).

The discrete model

The group velocity derived from discrete model (from equation 23) is:

$$v_{gr} = \left\{ \frac{1}{\sqrt{(m/a) \cdot \left\{ P + \left(Ga - \frac{Pa^2}{12} \right) k^2 \right\}}} \right\} \cdot \left\{ P + 2 \left(Ga - \frac{Pa^2}{12} \right) k^2 \right\} \quad (30)$$

Applying the long wavelength limits (i.e. $k \rightarrow 0$),

$$v_{gr} = \sqrt{\frac{P}{(m/a)}} \quad (31)$$

Using this velocity equation (31) in TOF (equation 26), we get

$$\text{TOF} = \frac{a}{\sqrt{\frac{P}{(m/a)}}}$$

Or

$$\text{TOF} = \sqrt{\frac{m \cdot a}{P}} \quad (32)$$

This is the TOF result for discrete model.

The comparison (between continuum and discrete models)

The comparison for both models (in equations 29 and 32) has shown a complete similarity of results at long wavelengths.

4.2.3 Momentum

Momentum is the quantity of motion of a moving body measured as a product of its mass and velocity. If the momentum is represented by M , then it can be written in the form of following equation:

$$\text{Momentum} = \text{mass} \times \text{velocity} \quad (33)$$

$$\mathbf{M} = \mathbf{m} \cdot \mathbf{v} \quad (34)$$

Here m is the mass and v is the velocity of the moving particle.

The continuum model

The angular frequency (equation 8) obtained from continuum model is:

$$\omega = \sqrt{\frac{Pk^2 + EIk^4}{(m/a)}}$$

As the phase and group velocities have the same values at long wavelength limits (see section 4.2.1). Then the phase velocity equation can be used for momentum calculation. For convenience we denote here phase velocity v_{ph} by v , as following:

$$v = \frac{\omega}{k} = \frac{\sqrt{Pk^2 + EIk^4}}{k} \quad (35)$$

Using this velocity equation (35) in momentum equation (34), we have

$$M = m \cdot \left(\frac{\sqrt{\frac{Pk^2 + EIk^4}{(m/a)}}}{k} \right)$$

Or

$$M = \frac{m}{k} \cdot \left(\sqrt{\frac{Pk^2 + EIk^4}{(m/a)}} \right) \quad (36)$$

Here the equation (36) gives the equation of momentum for continuum model.

The discrete model

The angular frequency (equation 10) obtained from discrete model [1] is:

$$\omega = \sqrt{\frac{Pk^2 + \left(Ga - \frac{Pa^2}{12}\right)k^4}{(m/a)}}$$

Then the (phase) velocity equation will become,

$$v = \frac{\omega}{k} = \frac{\sqrt{\frac{Pk^2 + \left(Ga - \frac{Pa^2}{12}\right)k^4}{(m/a)}}}{k}$$

Or

$$v = \frac{\sqrt{\frac{Pk^2 + \left(Ga - \frac{Pa^2}{12}\right)k^4}{(m/a)}}}{k} \quad (37)$$

Using this velocity equation (37) in equation (34), the momentum for discrete model will be

$$M = m \cdot \left(\frac{\sqrt{\frac{Pk^2 + \left(Ga - \frac{Pa^2}{12}\right)k^4}{(m/a)}}}{k} \right)$$

Or

$$M = \frac{m}{k} \cdot \left(\sqrt{\frac{Pk^2 + \left(Ga - \frac{Pa^2}{12}\right)k^4}{(m/a)}} \right) \quad (38)$$

Thus the equation (38) gives us the equation of momentum for discrete model.

The comparison (between continuum and discrete models)

To compare the momenta of both models, we can equate both equations (36 and 38) as following:

$$\frac{m}{k} \cdot \left\{ \sqrt{\frac{Pk^2 + EI k^4}{(m/a)}} \right\} = \frac{m}{k} \cdot \left\{ \sqrt{\frac{Pk^2 + \left(Ga - \frac{Pa^2}{12}\right)k^4}{(m/a)}} \right\}$$

After simplification finally we will arrive at

$$EI = \left(Ga - \frac{Pa^2}{12} \right) \quad (39)$$

Or

$$Ga - \frac{Pa^2}{12} = EI \quad (40)$$

$$Ga = EI + \frac{Pa^2}{12}$$

$$G = \left(EI + \frac{Pa^2}{12} \right) / a \quad (41)$$

The identical values (comparing to equation 12) of shear stiffness G represents here the conservation of momentum.

4.2.4 Energy

The energy of a vibrating system in physics is called vibrational energy. As this energy is related to the motion of system particles, it can also be denoted by kinetic energy (K.E.). The relation between momentum M and energy E (which in our case would be kinetic energy) is given by:

$$\text{Energy} = (\text{Momentum})^2 / (2 \times \text{mass}) \quad (42)$$

$$E = \frac{(M)^2}{2m} \quad (43)$$

By using the definition of momentum as being the product of mass and velocity, the equation (43) can be written as following:

$$E = \frac{(mv)^2}{2m}$$
$$E = \frac{1}{2}mv^2 \quad (44)$$

Here m is the mass and v is velocity of the moving particle.

The continuum model

The angular frequency (equation 8) obtained from continuum model is:

$$\omega = \sqrt{\frac{Pk^2 + EI k^4}{(m/a)}}$$

By denoting phase velocity as v , we have

$$v = \frac{\omega}{k} = \frac{\sqrt{\frac{Pk^2 + EI k^4}{(m/a)}}}{k} \quad (45)$$

Using this velocity equation (45) in energy equation (44), we will have

$$E = \frac{1}{2}m \cdot \left(\frac{\sqrt{\frac{Pk^2 + EI k^4}{(m/a)}}}{k} \right)^2$$
$$E = \frac{m}{2k^2} \cdot \left(\frac{Pk^2 + EI k^4}{(m/a)} \right) \quad (46)$$

Here the equation (46) gives the equation of energy for continuum model.

The discrete model

The angular frequency (equation 10) obtained from the discrete model is:

$$\omega = \sqrt{\frac{Pk^2 + \left(Ga - \frac{Pa^2}{12}\right)k^4}{(m/a)}}$$

By denoting phase velocity as v , we have

$$v = \frac{\omega}{k} = \frac{\sqrt{\frac{Pk^2 + \left(Ga - \frac{Pa^2}{12}\right)k^4}{(m/a)}}}{k} \quad (47)$$

Using this velocity equation (47) in energy equation (44), we will have

$$E = \frac{1}{2} m \cdot \left(\frac{\sqrt{\frac{Pk^2 + \left(Ga - \frac{Pa^2}{12}\right)k^4}{(m/a)}}}{k} \right)^2$$

Or

$$E = \frac{m}{2k^2} \cdot \left(\frac{Pk^2 + \left(Ga - \frac{Pa^2}{12}\right)k^4}{(m/a)} \right) \quad (48)$$

Thus the equation (48) gives us the equation of energy for discrete model.

The comparison (between continuum and discrete models)

To compare the energies of both models, we can equate both equations (46 and 48) as following:

$$\frac{m}{2k^2} \cdot \left\{ \frac{Pk^2 + EIk^4}{(m/a)} \right\} = \frac{m}{2k^2} \cdot \left\{ \frac{Pk^2 + \left(Ga - \frac{Pa^2}{12}\right)k^4}{(m/a)} \right\}$$

Or

$$\left\{ \frac{Pk^2 + EIk^4}{(m/a)} \right\} = \left\{ \frac{Pk^2 + \left(Ga - \frac{Pa^2}{12} \right) k^4}{(m/a)} \right\}$$

After simplification finally we will arrive at

$$EI = \left(Ga - \frac{Pa^2}{12} \right) \quad (49)$$

Or

$$Ga - \frac{Pa^2}{12} = EI \quad (50)$$

$$Ga = EI + \frac{Pa^2}{12}$$

$$G = \left(EI + \frac{Pa^2}{12} \right) / a \quad (51)$$

The numerical calculations are performed here assuming to be used for long wavelength approximations only.

4.2.5 Elasticity

Elasticity is the tendency of solid materials to return to their original shape after being deformed. Solid objects will deform when forces are applied on them. If the material is elastic, the object will return to its initial shape and size when these forces are removed. For an elastic case in which the Hooke's springs in the model can be assumed representing elasticity of the material, the extensional pulling force P can be written as following:

$$P = E\varepsilon \quad (52)$$

Here E is the modulus of elasticity and ε is the resultant strain in the material due to extensional force P .

The comparison (between continuum and discrete models)

As the functions and their values will remain the same in the case of (linear or idealized) elasticity defined by Hooke's law. We can directly substitute the extensional pulling force P as defined by equation (52) in the derived shear stiffness function G (equation 12) obtained by the comparison of continuum and discrete models as following:

$$G = \left(EI + \frac{E\epsilon a^2}{12} \right) / a$$

After simplification,

$$E = \frac{Ga}{\left(I + \frac{\epsilon a^2}{12} \right)} \quad (53)$$

As the conditions used here are elastic (according to Hooke's law), the symbol E can be replaced by E_{elast} and if we denote the rest of the symbols as following:

$$Ga = A, \quad \frac{\epsilon a^2}{12} = B$$

Then the equation (53) can be written as:

$$E_{\text{elast}} = \frac{A}{(I + B)} \quad (54)$$

4.2.6 Viscoelasticity

Viscoelasticity is the property of materials that exhibit both viscous and elastic characteristics when undergoing deformation. Viscous materials resist shear flow and strain linearly with time when a stress is applied. Elastic materials strain when stretched and quickly return to their original state once the stress is removed. Viscoelastic materials have elements of both of these properties and, as such, exhibit time-dependent strain. Whereas elasticity is usually the result of bond stretching along crystallographic planes in an ordered solid, viscosity is the result of the diffusion of atoms or molecules inside an amorphous material. For a simple viscoelastic case, the Kelvin-Voigt model [16] can be assumed representing elasticity of the material, the extensional pulling force P [appendix 4.7] can be written as:

$$P = \frac{\eta}{t} \epsilon \quad (55)$$

Here η the viscosity factor and t is the time. The function $\frac{\eta}{t}$ is equivalent to E in the Hooke's definition of elasticity (defined in equation 52).

The comparison (between continuum and discrete models)

As mentioned above in the discrete model case, we can directly substitute the extensional pulling force P (equation 55) in the shear stiffness G (equation 12) obtained by the comparison of continuum and discrete models as following:

$$G = \left\{ EI + \left(\frac{\eta}{t} \varepsilon \right) \cdot \frac{a^2}{12} \right\} / a$$

After simplification,

$$E = \left\{ Ga - \frac{\eta}{t} \left(\frac{\varepsilon a^2}{12} \right) \right\} / I \quad (56)$$

As the conditions used here are viscoelastic, the symbol E can be written as $E_{v\text{-elast}}$,

$$E_{v\text{-elast}} = \left\{ Ga - \frac{\eta}{t} \left(\frac{\varepsilon a^2}{12} \right) \right\} / I \quad (57)$$

And by using the above defined (in equation 54) symbols, equation (57) gets the shape as following:

$$E_{v\text{-elast}} = \left(A - \frac{\eta}{t} B \right) / I \quad (58)$$

Here the equation (54) is the numerical modulus of elasticity, whereas the equation (58) represents the viscous effects on the same elastic modulus. Thus

$$E_{\text{elast}} = \frac{A}{(I + B)} \quad E_{v\text{-elast}} = \left(A - \frac{\eta}{t} B \right) / I$$

The above comparison in the elastic and viscoelastic cases clearly represents a (decreasing/increasing) variation effect on modulus of elasticity E. If A, B and I values remain the same concerning there equivalent variations with respect to each other. The

variation factor then is only $\left(\frac{\eta}{t} \right)$, where η is a fixed viscosity factor (value), so we can show here analytically that with increasing time, the value of elasticity modulus E will change. This effect of variations was also observed in the literature [17].

4.2.7 Resonance

Frequencies at which the response amplitude is relatively maximum are known as the system's resonant or resonance frequencies. At these frequencies even small periodic driving forces can produce large amplitude oscillations, because the system stores vibrational energy.

The continuum model

The angular frequency (equation 8) of continuum model is:

$$\omega = \sqrt{\frac{Pk^2 + EI k^4}{(m/a)}} \quad (59)$$

Modeling of guided acoustic waves

As the resonant frequency ω_{reson} is the natural frequency of vibrations without any external force (i.e. $P = 0$) involved, so the equation (59) can be written as:

$$\omega_{\text{reson}} = \sqrt{\frac{0 + EI k^4}{(m/a)}}$$

Or

$$\omega_{\text{reson}} = (k)^2 \cdot \sqrt{\frac{(EI)}{(m/a)}} \quad (60)$$

The discrete model

The angular frequency (equation 10) of discrete model is:

$$\omega = \sqrt{\frac{Pk^2 + \left(Ga - \frac{Pa^2}{12}\right)k^4}{(m/a)}} \quad (61)$$

For no external force ($P = 0$), the angular frequency ω will become ω_{reson}

$$\omega_{\text{reson}} = \sqrt{\frac{0 + (Ga - 0)k^4}{(m/a)}}$$

Or

$$\omega_{\text{reson}} = (k)^2 \cdot \sqrt{\frac{(Ga)}{(m/a)}} \quad (62)$$

The comparison (between continuum and discrete models)

Comparing both resonant frequency equations (60 and 62),

$$(k)^2 \cdot \sqrt{\frac{(EI)}{(m/a)}} = (k)^2 \cdot \sqrt{\frac{(Ga)}{(m/a)}}$$

After simplification,

$$G = \frac{EI}{a} \quad (63)$$

Here G in terms of E , I , and a , is the value of shear stiffness at resonant frequency.

4.2.8 Impedance

Impedance is the measurement of resistance of a structure when subjected to harmonic motion. It can be given by relation [18] as following:

$$Z = \frac{F}{V} \quad (64)$$

Where Z is the impedance, F the force, and V is the resultant velocity due to applied force.

The continuum model

The angular frequency (equation 8) of the continuum model is:

$$\omega = \sqrt{\frac{Pk^2 + EIk^4}{(m/a)}} \quad (65)$$

As the phase velocity is equal to

$$v_{ph} = \frac{\omega}{k} = \frac{\sqrt{\frac{Pk^2 + EIk^4}{(m/a)}}}{k} \quad (66)$$

Also we know by definition the impedance Z is a ratio between force to the resultant velocity. So we can formulate the impedance equation using equation (66) as following:

$$Z = \frac{P}{v_{ph}} = \frac{P}{\frac{\sqrt{\frac{Pk^2 + EIk^4}{(m/a)}}}{k}}$$

The phase velocity has been used in the above equation because the approximation here is being conducted for long wavelengths only. And in this range the group and phase velocities become identical. Thus

$$Z = \frac{P \cdot k}{\sqrt{\frac{Pk^2 + EIk^4}{(m/a)}}} \quad (67)$$

This is the equation of impedance for continuum model.

The discrete model

The angular frequency (from equation 10) of the discrete model is:

$$\omega = \sqrt{\frac{Pk^2 + \left(Ga - \frac{Pa^2}{12}\right)k^4}{(m/a)}}$$

As the phase velocity is equal to

$$v_{ph} = \frac{\omega}{k} = \frac{\sqrt{\frac{Pk^2 + \left(Ga - \frac{Pa^2}{12}\right)k^4}{(m/a)}}}{k} \quad (68)$$

Applying the definition of impedance Z and using equation (68), we get the following relation:

$$Z = \frac{P}{v_{ph}} = \frac{P}{\frac{\sqrt{\frac{Pk^2 + \left(Ga - \frac{Pa^2}{12}\right)k^4}{(m/a)}}}{k}}$$

Or

$$Z = \frac{P \cdot k}{\sqrt{\frac{Pk^2 + \left(Ga - \frac{Pa^2}{12}\right)k^4}{(m/a)}}} \quad (69)$$

This is the equation of impedance for discrete model.

The comparison (between continuum and discrete models)

Comparing the impedances of both models (equations 67 and 69),

$$\frac{P \cdot k}{\sqrt{\frac{Pk^2 + EI k^4}{(m/a)}}} = \frac{P \cdot k}{\sqrt{\frac{Pk^2 + \left(Ga - \frac{Pa^2}{12}\right)k^4}{(m/a)}}}$$

After simplification,

$$Ga - \frac{Pa^2}{12} = EI \quad (70)$$

Or

$$P = (Ga + EI) \cdot \left(\frac{12}{a^2} \right) \quad (71)$$

The condition:

Suppose if the applied pulling force is minimum (i.e. almost equal to zero), then the equation (71) would become

$$0 = (Ga + EI) \cdot \left(\frac{12}{a^2} \right)$$

Or

$$G = -\frac{EI}{a} \quad (72)$$

As we know only a minimum force (≈ 0) is needed to move a structure at resonant frequency. The equation (72) is just the same result which we already have obtained in the resonance frequency case (equation 63) but with opposite (negative) sign. The opposite sign here shows that it has an opposing or resistive behaviour towards the motion of the structure.

4.3 Analytical treatment of modeling results (in comparison with the experimental results)

As according to the given lattice dynamics model [1], the dispersion relation of transversely polarized mechanical waves traveling along the linear mass-spring chain under external pull simulating the guided acoustic waves at long wavelengths limit is given by the following equation (original is equation 4):

$$\omega = \sqrt{\frac{(2Pa + 6G) - (2Pa + 8G) \cdot \cos(ka) + 2G \cdot \cos(2ka)}{ma^2}} \quad (73)$$

The comparison of modeling results is performed here to the results of A0 Lamb wave mode and the parameters used for calculations are according to our experimental sample dimensions given as following:

$$a = \{a_0 + P / C\} \quad (\text{Lattice displacement function with external pull } P)$$

Where,

$$a_0 = 1 \text{ mm} = 0.001 \text{ m} \quad (\text{Basic lattice unit with no external pull } P)$$

$$P = 60 \text{ N/min} \quad (\text{Pulling force applied linearly for 10 minutes to reach a maximum of 600 N})$$

$$C = 144\varepsilon \left[4 \frac{(\sigma_{Al})^{12}}{(a_0)^{14}} - \frac{(\sigma_{Al})^6}{(a_0)^8} \right]$$

Here C is the nonlinear inter-atomic spring coefficient (see section 4.1.6) acting within the lattice chain and is derived from Lennard-Jones potential. It is evaluated according to literature [19] as following:

$$\varepsilon = 4551 \text{ K} \quad (\text{Depth of the potential well})$$

$$\sigma_{Al} = 2.62 \text{ \AA} = 2.62 \times 10^{-10} \text{ m} \quad (\text{Inter-atomic displacement where the potential becomes zero})$$

$$d = 20 \text{ mm} = 0.02 \text{ m} \quad (\text{Total width of the aluminum sample})$$

$$a_0 \times d = 20 \times 10^{-6} \text{ m}^2 \quad (\text{Cross-sectional area of the aluminum sample})$$

$$L = 38 \text{ cm} = 0.38 \text{ m} \quad (\text{Total length of the aluminum sample})$$

$$m = 5.4 \times 10^{-5} \text{ kg} \quad (\text{Point mass value of the aluminum})$$

$$G = 115 \text{ Nm} \quad (\text{Torsional stiffness value in the aluminum})$$

And,

$$k = \text{Wave number} \quad \text{Where} \quad k_{\max} = \frac{\pi}{a} \quad (\text{in units } 1/\text{m})$$

Also the TOF (see section 4.1.5) is defined as following:

$$\text{TOF} = \frac{\sqrt{ma^2}}{[(Pa + 4G) \cdot \sin(ka) - 2G \cdot \sin(2ka)]} \left[\sqrt{(2Pa + 6G) - (2Pa + 8G) \cdot \cos(ka) + 2G \cdot \cos(2ka)} \right] \quad (74)$$

To observe the resulting acousto-elastic effects on guided acoustic waves due to extensional stress, here an elastic coupling function denoted by E_{CF} [11] is defined such that:

$$E_{CF} = \frac{1}{\left[\frac{L \cdot P}{a_0 \cdot d} \right]} \cdot [\text{TOF}] \quad (75)$$

Where

TOF = Time-of-flight calculated by equation (74)

P = Total pulling force applied during experiment

L = Total length of the sample used

$a_0 \cdot d$ = Area of cross-section of the sample

E_{CF} is obtained by substituting the above parameters relating to experiment in equation (75). The units of this function are given in terms of $\text{ns m}^{-1} \text{MPa}^{-1}$. A plotted graph with experimental and function generated data is provided in the figure 3.

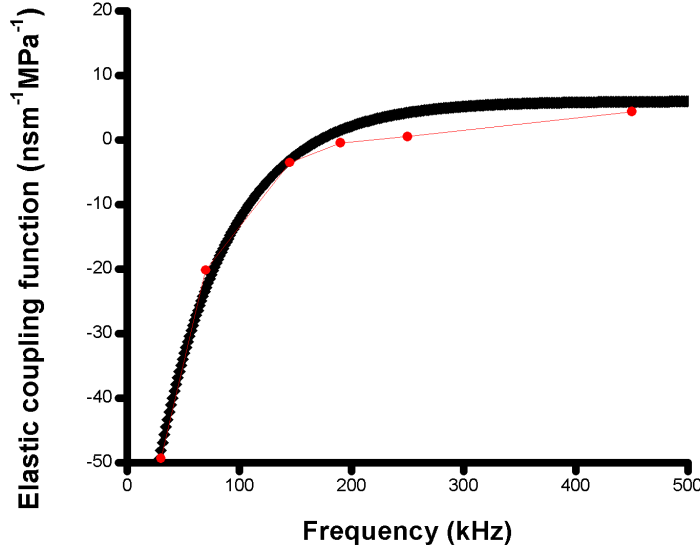


Figure 3: The plotted graph shown by the experimental data (red) points and model derived elastic coupling function (E_{CF}) generated data (black) line.

In the above graph (figure 3), the experimental data points are plotted in the low frequency range from 0 to 500 kHz. The developed acousto-elastic function has been employed here by using the derived inter-atomic Lennard-jones potential. A close match between experimental and function derived theoretical results has been found.

Both results (figure 3) indicate a gradual rising at the start of frequency, increasing exponentially and later become almost parallel to the zero E_{CF} scale. The corresponding asymptotic functions for frequencies approaching zero and infinity are derived in the following text. First of all, we will find a function defined for frequency at $E_{CF} = 0$.

4.3.1 Zero crossing (i.e. frequency value at zero E_{CF}):

To find the value of frequency at E_{CF} equals to zero, the respective zone boundary or wave number function (ka) can be derived from equation (75) and is defined [appendix 4.8] as following:

$$ka = \cos \left[\frac{(2Pa + 4G) \cdot (4G)}{(2Pa + 8G)} \right] \quad (76)$$

The equation (76) gives us function value in terms G , P , and a , to evaluate frequency at zero E_{CF} . The value obtained from this function (equation 76) is further substituted in the following frequency equation (77) derived from equation (73).

$$f = \frac{\sqrt{\frac{(2Pa + 6G) - (2Pa + 8G)\cos(ka) + 2G\cos(2ka)}{ma^2}}}{2\pi} \quad (77)$$

The result found is the frequency value at zero E_{CF} ,

$$f = 198.5124 \text{ kHz} \quad (78)$$

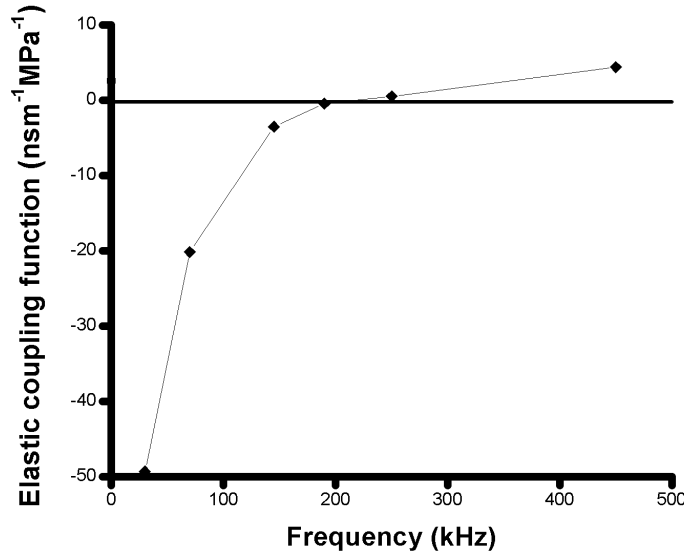


Figure 4: The graph drawn by the measured experimental data points and joined each other by thin straight lines.

We can see in the graph (figure 4) that the experimental data will intersect the zero-line (i.e. $E_{CF} = 0$) near 200 kHz, which is almost equal to the theoretically (equation 77) derived result (198.5124 kHz). The comparison of the function generated result to the experimentally measured data provides a close match which suggests the derived function (equation 76) can serve a generalized model for the ultrasonic guided waves to predict the frequency value at zero E_{CF} .

4.3.2 Horizontal asymptote (i.e. elastic coupling function for $f \rightarrow \infty$):

To find the horizontal asymptote with frequency approaching infinity, the respective wave number function (ka) can be derived from equation (75) and is defined [appendix 4.9] as following:

$$ka = \sqrt{\frac{6aP}{(12G - aP)}} \quad (79)$$

The equation (79) gives us function value in terms G , P , and a , related to the horizontal asymptote. The value obtained from this function (equation 79) is further substituted in

the equation (75). Thus evaluating E_{CF} the numerical value of horizontal asymptote is found to be:

$$E_{CF} = 8.3934 \text{ nsm}^{-1}\text{MPa}^{-1} \quad (80)$$

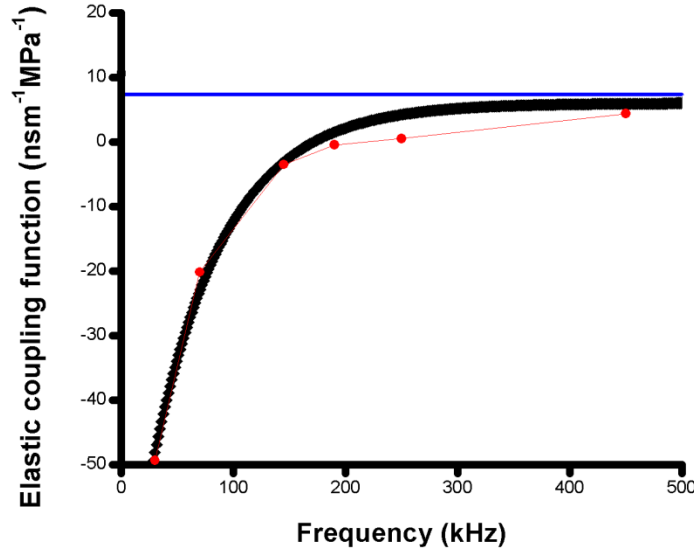


Figure 5: The plotted graph drawn by experimental data (red) points and elastic coupling function (E_{CF}) generated data (black) line. The blue line represents the horizontal asymptote for the infinite frequency limit.

The straightening behaviour becomes more and more prominent as the graph approaches near the horizontal asymptote (blue line). The function E_{CF} represents rather ideal conditions in the material and can produce a close match for the expected horizontal asymptote. The graph expresses the insensitivities of the material reaction towards external stress as its frequency tends to reach infinity or when it nears the acousto-elastic value of $8.3934 \text{ nsm}^{-1}\text{MPa}^{-1}$.

4.3.3 Vertical asymptote (i.e. elastic coupling function for $f \rightarrow 0$):

To find the vertical asymptote with frequency approaching zero, the respective wave number function (ka) can be derived from equation (75) and is defined [appendix 4.10] as following:

$$ka = \sqrt{\frac{P}{\left(\frac{P}{6} - \frac{2G}{a}\right)}} \quad (81)$$

The equation (81) gives us function value in terms G , P , and a , related to the vertical asymptote. The obtained value from equation (81) is further substituted in the frequency

equation (77) to get the frequency axis point of vertical asymptote. The numerical value of vertical asymptote here is found to be:

$$f = 6.3158 \text{ kHz} \quad (82)$$

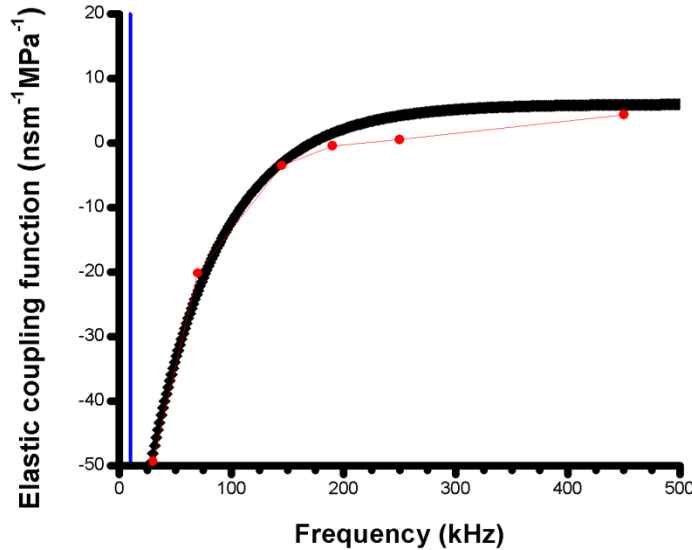


Figure 6: The plotted graph drawn by experimental data (red) points and elastic coupling function (E_{CF}) generated data (black) line. The blue line represents the vertical asymptote for the minimum frequency limit.

As shown in figure 6, the vertical asymptotic behaviour of graph will become more evident as it goes towards its minimum frequency scale. The graph extends itself such that it never reaches to zero frequency but becomes increasingly parallel to a vertical scale value equal to 6.3158 kHz. The result confirms that the derived wave number function (equation 81) can produce a closely predictable vertical asymptotic.

For the lowest anti-symmetric (A0) mode at a specific frequency, the TOF becomes insensitive to the applied puling force due to the opposing interplay of the stress stiffening as known from strings, and softening caused by the anharmonicity of the binding potential. This behavior has been theoretically confirmed by the E_{CF} graph (figure 5) where it shows a considerable (parabolic) variation at lower frequencies (from minimum to nearly 300 kHz), and lately tends to align with horizontal asymptote.

4.4 Conclusive statement of the analytical treatment:

Due to the higher sensitivity of A0 Lamb wave mode and its wider applicability for the structural assessment techniques, the mode is investigated theoretically and is compared to the experimental findings. The provided comparison has been found in satisfactory agreement between the measured and theoretically predicted results. Since a real material with experimentally measured results can include several other factors

involving temperature change, material defects, etc., the theoretically predicted results can only present a near similar possible shape, as demonstrated here.

The comparison of results is here restricted to the range of wavelengths, where the discrete structure of the model is of no significant relevance. Even though numerical calculations on the basis of continuum mechanics have been performed to demonstrate the influence of externally applied tensional stress on guided ultrasonic waves traveling in plates concentrating on anti-symmetric Lamb waves of the lowest branch, no generalized treatment based on discrete modeling has so far been presented. In the absence of stiffness to bending, the then soft chain will show an increase in the velocity of transversely polarized mechanical waves that approaches, concerning the related elastic coupling function (E_{CF}), even infinity for vanishing external stress. As demonstrated here, the situation is less dramatic for chains exhibiting a finite stiffness with respect to bending. Under this condition the stress induced effect will dominate the behavior at sufficiently long wavelengths and the TOF will rapidly diminish under rising external extensional stress. On the other hand, for sufficiently small wavelengths the behavior of the stiff chain will dominate. For sufficiently small wavelengths the guided acoustic waves will finally exhibit a small but positive effect concerning the dependence of the observed TOF on external extensional stress. This is caused by softening due to anharmonic effects. For longer wavelengths the stress stiffening will finally dominate the result for transversely polarized acoustic waves and rather large negative acousto-elastic coefficients can be observed (figure 3).

The current chapter has provided a further extended study in the form of its derived physical parameters, their comparison with continuum mechanics, and an analytical comparison to the experimentally achieved results. The provided advancement in the lattice dynamics simply can add a step further in the existing knowledge of Science especially in the Solid State Physics.

4.5 Summary

The developed mass-spring chain model [1] has been applied here using Lennard Jones potential as stiffness coefficients to demonstrate the effects of anharmonicity on TOF under extensional stress. Due to its more sensitive nature to the extensional stress, the focus is given to the fundamental anti-symmetric (A_0) Lamb wave mode. The provided modeling has been analyzed by deriving frequency dependent physical parameters, and by comparing them to their relevant continuum model. A close matching between the results of discrete and continuum models has been found. The theoretical results are further verified analytically by developing elastic coupling function (E_{CF}) and by comparing it with the experimental results.

4.6 References

[1] M. Pluta, U. Amjad, H. Klinghammer, D. Jha, K. S. Tarar, W. Grill, "Dispersion relations and stress dependencies of acoustic waves travelling on a chain of point

- masses connected by linear and torsional springs”, *Acoustical Imaging* 31, 253-265, (2012)
- [2] Charles Kittel, “Introduction to solid state physics”, Published by John Wiley and Sons, 8th edition, (2008)
- [3] J. Appel, “Atomic ordering and T_c of narrow-band superconducting alloys”, *Phys. Rev. B* 13, pp. 3203–3208, (1976)
- [4] B. Donovan, J. F. Angress, “Lattice Vibrations”, Published by Chapman and Hall, (1971)
- [5] Richard H. Bube, “Electrons in solids: An introductory survey”, 3rd edition, Published by Academic Press Limited, (1992)
- [6] Lennard-Jones, “On the Determination of Molecular Fields”, *Proc. Roy. Soc. London A* 106 (738), pp. 463–477, (1924)
- [7] P. M. Morse, “Diatomic molecules according to the wave mechanics. II. Vibrational levels”, *Phys. Rev.* 34, pp. 57- 64, (1929)
- [8] U. Amjad, D. Jha, K. S. Tarar, H. Klinghammer, W. Grill, “Determination of the stress dependence of the velocity of Lamb waves in aluminum plates”, *Proc. SPIE* 798410, (2011)
- [9] K. S. Tarar, U. Amjad, W. Grill, “Lumped circuit mechanical models and lattice dynamics approach to the dependence of the time-of-flight of bulk and guided acoustical modes on elongation”, *Proc. SPIE* 76500I, (2010)
- [10] K. S. Tarar, M. Pluta, U. Amjad, W. Grill, “Lattice dynamics approach to determine the dependence of the time-of-flight of transversal polarized acoustic waves on external stress”, *Proc. SPIE* 79842R, (2011)
- [11] K. S. Tarar, M. Pluta, W. Grill, “Linear chain lattice dynamics approach to the dependence of the time-of-flight of acoustical modes on stress and strain”, (article in preparation for publication)
- [12] Robert Hooke, “Ut tension, sic vis, (meaning: as the extension, so the force)”, (1678)
- [13] M. Pluta, U. Amjad, H. Klinghammer, D. Jha, K. S. Tarar, W. Grill, “Stress dependent dispersion relations of acoustic waves travelling on a chain of point masses connected by anharmonic linear and torsional springs”, *AIP Conf. Proc.* Vol. 1433, 471 (2012)
- [14] P. D. Wilcox, F. Chen, “The effect of load on guided wave propagation”, *Ultrasonics*, Vol. 47, 111–122, (2007)
- [15] E. Carrera, G. Giunta, M. Petrolo, “Beam Structures: Classical and Advanced Theories”, Published by John Wiley & Sons Ltd, Print ISBN: 9780470972007, (2011)

- [16] M. A. Meyers, K. K. Chawla, "Mechanical Behavior of Materials", Published by Cambridge, 2nd edition, ISBN: 9780521866750, (2008)
- [17] S. Hyun, T. K. Hooghan, W. L. Brown, R. P. Vinci, "Linear viscoelasticity in aluminum thin films", Applied Physics Letters, Vol. 87 (061902), (2005)
- [18] P. L. Gatti, "Applied Structural and Mechanical Vibrations", Published by CRC Press, ISBN: 9780203014554, (2002)
- [19] T. Halicioglu, and G. M. Pound, "Phys. Status Solidi A 30", 619, (1975)

5. Signal processing scheme (pulse compression)

For applications involving the determination of variations of the time-of-flight (TOF) in pulsed echo or transit experiments, a method [1-2] has been developed based on Fourier transformation with forced optimized compression of the reference signal to an only bandwidth limited approximation of a Dirac delta function. The respective transformation of time shifted response signals allows the effective separation of otherwise overlapping signals and the detection of differences in the time-of-flight for the individual components with high resolution. The developed processing scheme corrects for dispersion and attenuation in the electronics, the transmission lines, and the transducers. The method is presented and applications are demonstrated.

A scheme [3-4] more suitable for higher precision at even lower power levels is chirped excitation and signal compression following the detection. This scheme used in radar-ranging since 1944 was originally based on passive devices for compression serving the purpose to raise the amplitude to a level above the noise. It is also favorable for signal generation since the excitation energy can be distributed in time, and excessively high power levels unsuitable for the available components can thus be avoided. In the case of the application of similar techniques in acoustics, the conditions are often such that signal levels are sufficient for detection, such that the signals are not deeply buried in the noise. Compression can thus be performed digitally following the digitization of the detected signal. Such temporal resolution can be optimized to minimize overlaps, and to separate signals from different modes, echoes or flaws in applications [5-8] involving NDT or NDE and for ultrasonic imaging [9-11].

For the development presented here, a special group of applications involving the detection of only small variations of the time-of-flight which on the other hand should be detected with a high resolution if compared to the involved total time-of-flight is addressed. Additionally optimum pulse compression close to the limits given by the available band width is desired to minimize temporal overlaps of signals from different acoustic modes or paths.

5.1 The compression scheme

Optimum compression would be achieved if the closest possible approximation to a Dirac delta function is obtained for the purpose addressed here. For single shot measurements, if not alternatively analyzed by Laplace transform methods, a continuous Fourier transform would be needed for analysis which is approximated here in the usual way by computing with the aid of Fast Fourier Transformation [12] (FFT) with a sufficiently large number of points respectively frequencies to obtain a suitable resolution. Such numerically the ultimate compression would be obtained if, following the compression performed with the aid of Fourier transformation, only a single point of the time resolved representation finally obtained would have a value different than zero indicating directly the time-of-flight. Since a Dirac pulse requires an unlimited bandwidth, this can under experimental conditions only approximately be achieved. Furthermore for discrete (digital) representations positions can be determined to a resolution beyond the limitation given by the sampling intervals. By fitting to slopes or other shaped structures of the signals, the signal resolution (usually between 8 and 16 bit) will also contribute to

the achievable temporal resolution. Under the conditions of interest here this idealized result will be limited by the bandwidth achievable under the given experimental conditions. Of primary influence is thereby the bandwidth of the ultrasonic transducers and the transport properties for acoustic waves in the sample in which the ultrasound is traveling.

Furthermore digitizing is employed for signal acquisition and only a limited time span is used for processing. The selection of the respective equipment and parameters will define the number of available data points that can be used for FFT in the evaluation process including the desired compression. The suitable electronic devices can be identified within the limits of availability on the basis of bandwidth with the aid of the Nyquist-Shannon-theorem [13] and from the (in a single shot measurement) achievable signal-to-noise ratio concerning the number of bits desired for the resolution. Signals can be averaged to enhance the signal-to-noise ratio for the processed data. A basic feature of the spectral content of a Dirac pulse is that the spectral magnitude does not depend on frequency, representing a so called “white spectrum”. If the position of the pulse in time is zero, then the phases of all frequencies in the decomposition are identical to the phases of cosine functions (zero for all frequencies). A shift of the pulse position in time will result in a respective slope of the (strictly linear) phase dependence on frequency, proportional to the temporal position. The sign of the slope relates to a temporal position prior (positive slope) respectively past (negative slope) zero time.

The method presented [1-2] here relies on the feature that optimum pulse compression is to be expected, if received signals are transformed such that within the useful bandwidth all magnitudes for the frequencies of the decomposition are equal (for simplicity here normalized to 1), and the phases as a function of frequency display a strictly linear dependence. To achieve that (in an unusual way as indicated in a related patent [14]), the magnitudes and phases related to the recorded echo in the reference signal are forced to one respectively zero (in that order) within the useful frequency ranges (as displayed in combination with an actual measurement in figure 8). Outside such ranges the magnitudes are forced to zero. There the phases could have any value but are just set in a similar way as for the relevant frequency ranges. Whereas the transformation such needed for magnitude correction is just a forced definition, the transformation employed for the phase is simply a subtraction of the phase determined by FFT (ideally by a continuous Fourier transform) for the initially (ideally continuous) measured time dependent reference signal. The phase transformation such determined with the aid of the reference signal serves as compression procedure for any signal for which a relative shift is to be determined. The range where in that process amplitudes are subjected to a forced definition should be selected such that for the reference and any temporally shifted signal the same definition is employed.

5.2 Example with an artificial chirped signal

For the results presented here, for simplicity only quasi rectangular amplitude definitions are employed. It has to be mentioned that, depending on the desires, any suitable window such as the well-established Hamming or Blackman-Harris window can be employed. The rectangular windowing, even though providing a narrow center lobe will,

on the other hand, lead to pronounced side lobes. The result of such a compression for an idealized, analytically defined chirp signal (figure 1) is represented in figure 2 and compared to the result obtained from an autocorrelation procedure.

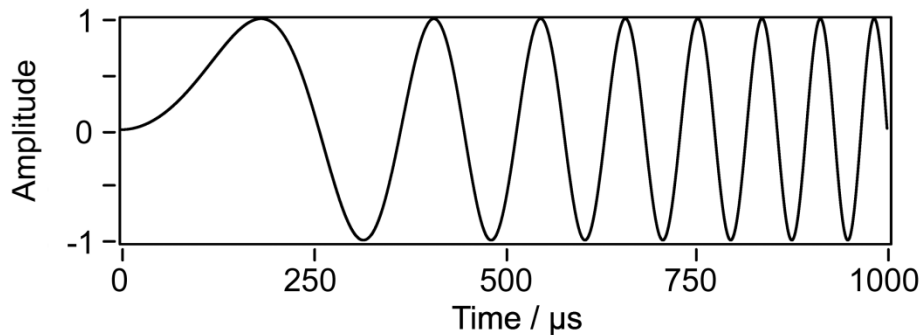


Figure 1: Analytically defined linear chirp pulse (from almost zero to 5 MHz) used as input data for the demonstration of the compression scheme (figure 2) under idealized conditions.

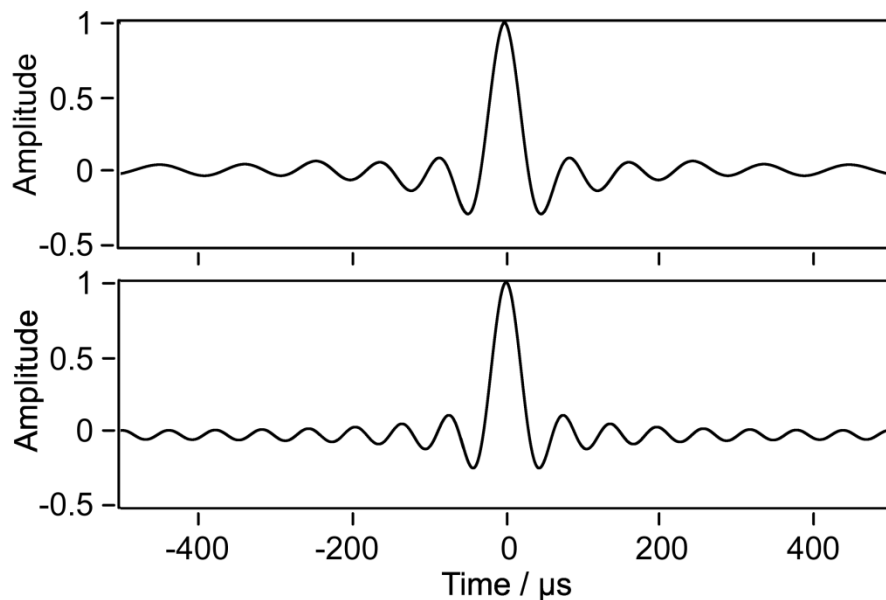


Figure 2: Result of compression by the developed method (bottom) and result of an autocorrelation (top) for comparison; both displayed on identical scales with normalized maximum amplitudes.

As can be deduced from the graphs (figure 2), only a slight advantage is obtained by signal compression with respect to the results of (standard) correlation procedures concerning the width of the center lobe and the respective relative height and distance of the adjoining side lobes. So obviously for an ideal (received and recorded) signal, no significant advantage, other than the narrowing of the central peak by a factor of about

0.7 ($\frac{1}{2}\sqrt{2}$ is to be expected for folding of Gaussian profiles), can be obtained by the developed method with respect to well established correlation procedures.

It is the purpose of the developed compression scheme to optimize the results for non-ideal signals, obtained at least often if not generally in applications. Among the distortions usually observed are dispersive effects in phase and (for resonances following Kramers and Kronig related) frequency dependent amplitudes. The obtainable advantages also including a comparison to correlation results are presented and discussed in combination with the experimental results for an application used for demonstration of the method following a short outline of the instrumentation.

5.3 Instrumentation

For the measurements presented here, commercially available equipment including a lap-top computer interfaced to an arbitrary function generator and synchronized transient recorder has been employed (figure 3). The limiter and preamplifier are custom designed. The software is custom developed with the aid of LabVIEW[®] (computer program).

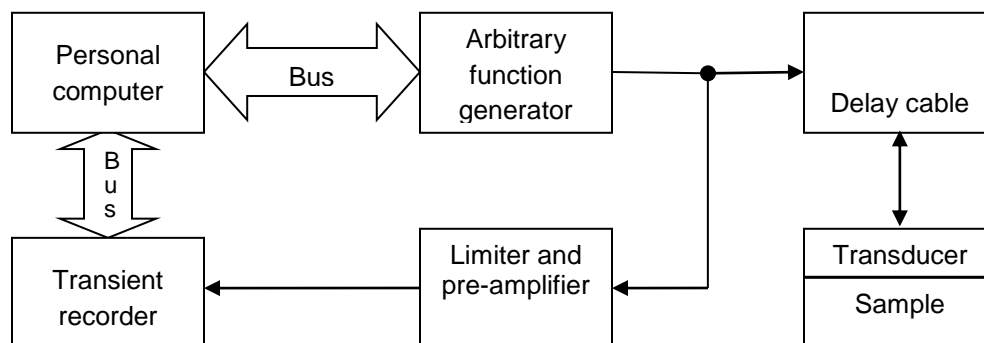


Figure 3: Experimental set-up used for the signal and data acquisition by computer controlled equipment with online evaluation.

5.4 Application

A brass sample with a length of 50 mm and 50 mm diameter is used in combination with a piezoelectric disc transducer with a diameter of the active part of 28 mm. For the signal delay, 50 Ohm coaxial cable (RG 58) is employed. An overview of the detected signal obtained for a chirp ranging from 500 kHz to 12 MHz is displayed in figure 4. The overloaded part of the signal at the beginning represents the crosstalk from excitation followed by the first echo. The part of that echo used for processing is indicated in the graph by dashed vertical lines. Three more echoes follow with the last one only partially displayed.

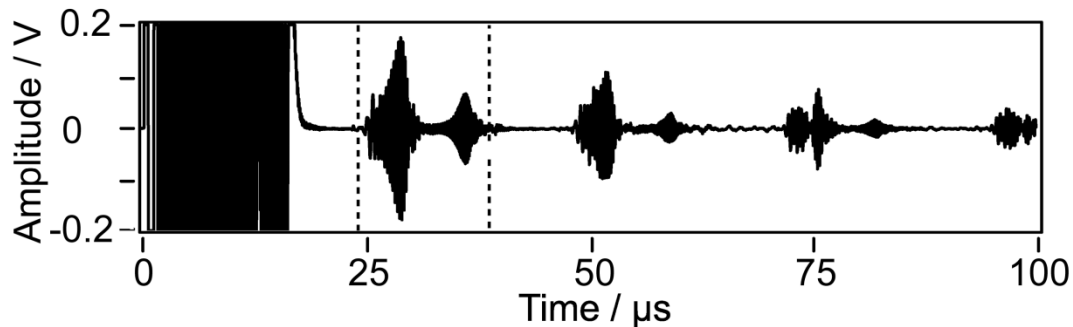


Figure 4: Digitized time dependent received electrical signal (oscillatory parts with overlapping lines connecting the measured points) with indicated range of the processed first echo of longitudinal polarized acoustic waves.

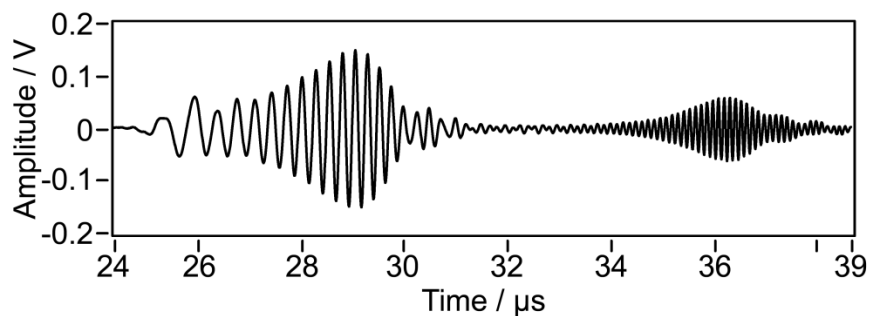


Figure 5: Magnified view of the part of figure 4 containing the range of the processed first echo (part representing higher frequencies displayed with overlapping lines).

The range of the processed first echo is displayed in more detail in figure 5. The measurement represented in these figures relate to the minimum electronic delay and room temperature. The other measurements evaluated involve only small additional delays and only minor changes in the signal shape not easily recognizable in an overview (and therefore not displayed here). All measurements presented here have been performed with 50 MHz sampling rate and 12 bit resolution for excitation, and 100 MHz sampling rate and 8 bit resolution for detection with phase locked sampling frequencies.

Since a linear chirp is involved, the numerically determined spectrum (figure 6) resembles the envelope of the time dependent signal used for evaluation (figure 5). The phase represented in a continuous representation shows a kink (sign change of 1st derivative) at a frequency where the magnitude is rather small and can in some ranges not necessarily be easily interpreted due to the rather small magnitudes involved, which may be comparable to the noise. This can lead to arbitrary phases (concerning multiples of 2π) in a continuous representation (of the sampled data). Such a possible jump is at least recognizable in the range below 1 MHz.

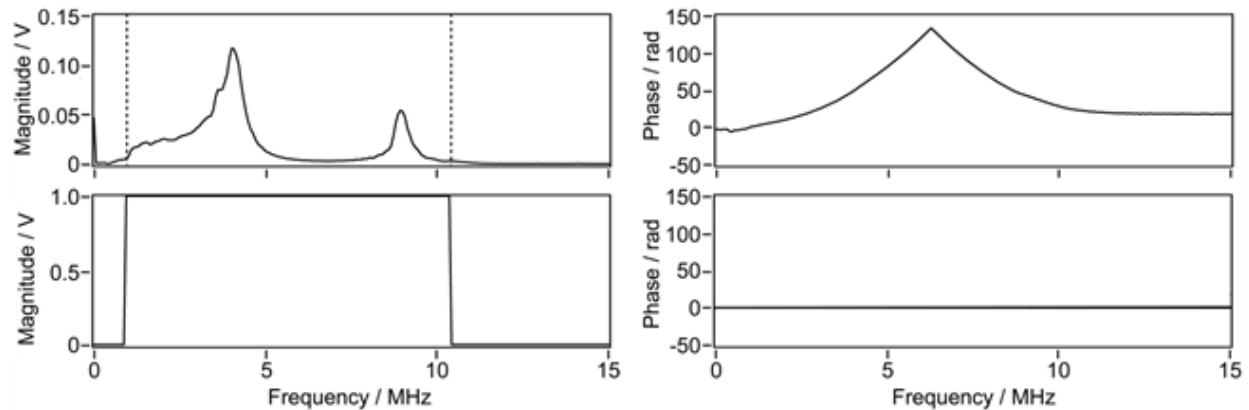


Figure 6: Illustration of the data processing concerning the reference signal with the determined spectral content (top, left), the determined phase (top, right) and an illustration of the normalized forced magnitude (bottom, left) and forced phase (bottom, right) serving as a basis for the determination of the transformation involved in the compression scheme.

In figure 6 the experimentally determined frequency dependencies of magnitude and phase are compared to the forced amplitudes and phases used for the developed compression scheme. The correction function involved in the compression scheme is simply the phase determined for the reference measurement (top, right in figure 6) with opposite sign for the phase (multiplied by -1) respectively as displayed if subtracted in the transformation process (and therefore not displayed in an extra graph).

Following the just outlined determination of the transformation procedure, which was also adjusted concerning the used frequency range to the results of the (following) measurements involved in the differential measurement scheme, the data collected for additional delays is evaluated.

First the numerical results for processing of the data obtained in a measurement, otherwise identical to the one acting as reference, but with an additional electronic delay introduced by a different inserted delay cable (figure 3) are analyzed according to the developed scheme. Correction of the detected phase by the phase transformation defined above delivers in that case (at least at first glance) a rather complicated structure represented in figure 7. Due to non-realistic phase tracking in the region of smaller signals, the center part exhibits a slope relating to earlier arrival whereas in the region of sufficiently large signals about equal slopes, relating to a delayed arrival, are displayed. Identifiable are also regions with mixed slopes respectively fluctuating phases relating to frequencies with rather small signal magnitude.

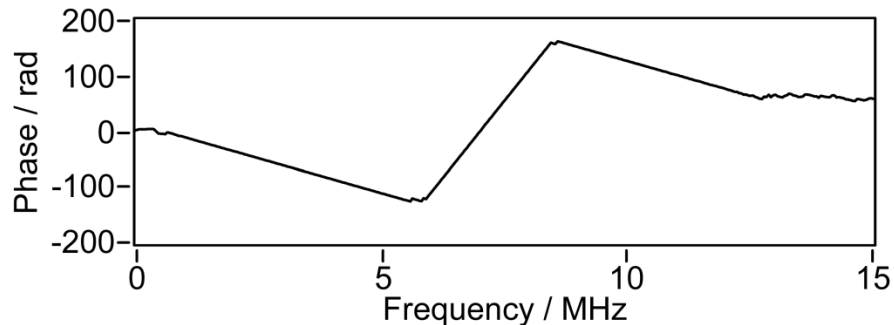


Figure 7: Numerically determined phase in continuous representation for the data measured with additional cable delay corrected by the transformation based on the determined phase of the reference signal.

This result (figure 7) is displayed to demonstrate that, even though the delay can also be determined from the slope of the phase, special efforts are needed in that case, to identify the ranges where a reliable continuous representation can be achieved. The developed compression scheme is not depending on continuous representations employed here only for display.

5.5 Results

Following the developed procedure, a time dependent compressed signal is derived numerically from the transformed phase and defined magnitude by inverse-FFT from the recorded data for the measurements involving a variation of the time-of-flight (additional delay). The results are displayed in figure 8 (left). First the evaluation scheme is applied to the data of reference measurement itself to demonstrate the result for an unaltered position and subsequently zero differential delay concerning the scheme of the method. To allow comparison on similar scales, the results for the following measurements involving additionally delayed signals are displaced by the differential delay time (ΔTOF ; table 1). The individual delay times are determined in the final step of the procedure by fitting of a Gaussian function to the primary peak of the measured data (figure 9, table 1).

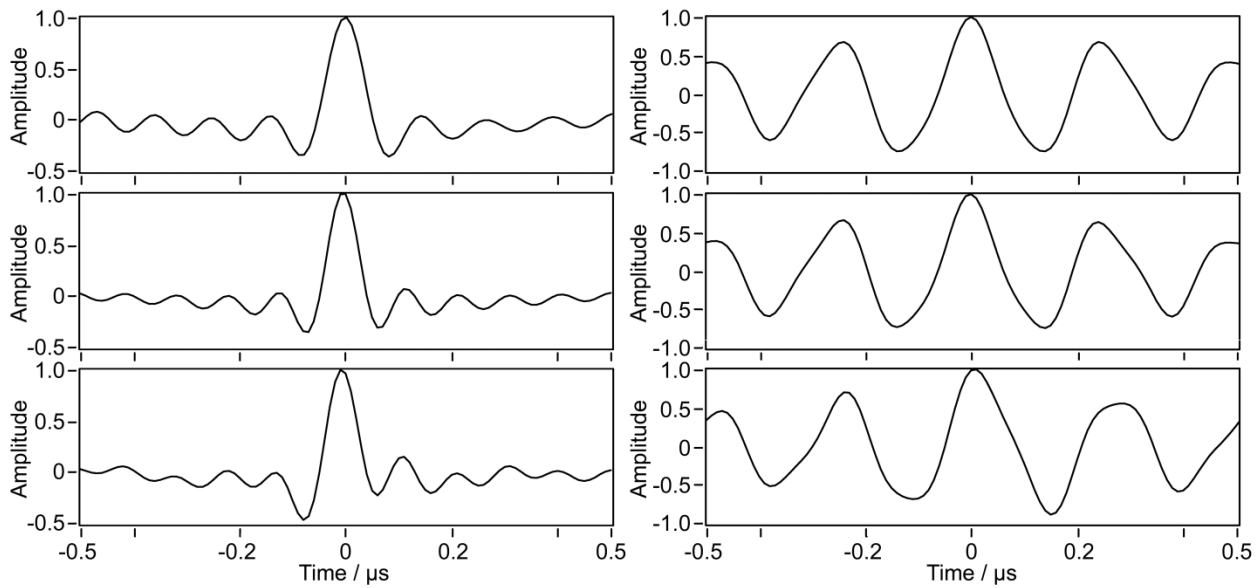


Figure 8: Results of compression (left) and of correlation (right) for comparison with reference signal (top), signal for extra cable delay (middle) and for a signal delayed by heating (bottom). The time scales are each shifted by the respective finally determined (table 1) differential delay times.

As a first application, a delay is introduced by an extra length of cable, for which only a small minor change in the pulse shape due to dispersion in the cable is to be expected.

Alternatively a delay is introduced by a temperature rise of the sample, relating to a scenario typical for ultrasonic application involving the need for differential schemes. Mainly since the temperature variation influences the resonance frequencies of the employed transducer, the shape of the compressed signal shows recognizable differences from that obtained for the reference itself. The width of the main lobe and the relative height of the larger (right) side lobe with respect to the main lobe remain nevertheless almost unaltered.

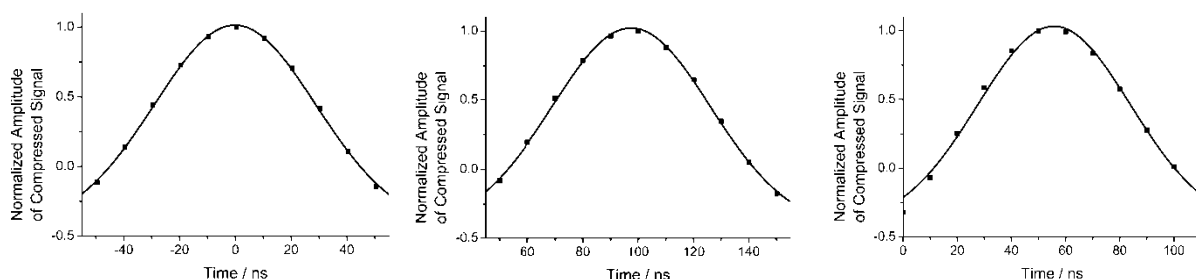


Figure 9: Center peak and fitted Gaussian curve for the processed reference signal (left), the signal obtained with additional cable delay (center), and the signal shifted by (moderate) heating of the sample (right) with a time scale for which the zero position relates to the expectation value for a signal not delayed with respect to the reference

signal. In all graphs the squares represent measured data points and the lines Gaussian functions fitted to the data for the displayed points.

Δ TOF for the reference signal	- 0.1 ns \pm 0.2 ns
---------------------------------------	-----------------------

The results listed below are corrected for the extra delay (Δ TOF) determined (above) for the reference signal.

Δ TOF for the signal delayed by a cable	97.8 ns \pm 0.4 ns
--	----------------------

Δ TOF for the thermally delayed signal	55.9 ns \pm 0.7 ns
---	----------------------

Table 1: Results for the determination of the differential time-of-flight (Δ TOF) referenced to the expectation value by the developed compression scheme obtained by fitting of a Gaussian function to the center peak (figure 9).

The comparison with respective results obtained by correlation exhibits the advantages of the developed compression scheme for chirped signals. The width of the center lobe and the relative height of the side lobes are both favorable for the developed scheme. The dominant disadvantage of the correlation scheme is the large side lobes, which for variations of the transducer and of the transport properties beyond the level already visible for the delay caused by heating, can lead to a mix up of the peaks (jump of the global maximum to a former side peak). In the application exemplified here, this would lead to an error of more than 200 ns (figure 9).

A larger number of processed points concerning FFT can further enhance the resolution until sufficient over-sampling is involved. Due to limitations of the involved online processing, this is not the case for the results displayed here. Furthermore the resolution is derived in the presented examples from a least square deviation to a fitted Gaussian function. Since concerning the shape a forced fit is used for an experimental result where this shape is not to be expected, a systematic error is involved. This can be rectified by adaptive fitting. If (with forced fitting) the resolution is determined from subsequent measurements under otherwise identical conditions, standard deviations in the regime of a few picoseconds can be achieved. For the signal delay with respect to excitation of about 30 μ s observed here, the ultimate so far reached resolution of about 5 ps (with the sample employed here) represents an uncertainty of 1 in 6×10^6 with respect to the total delay.

5.6 Summary

A pulse compression scheme suitable for differential measurements concerning the time-of-flight of ultrasound echo or transit signals based on Fast Fourier Transformation has been demonstrated. The scheme takes care of corrections of phase and amplitudes for optimum pulse compression in applications where small variations of time-of-flight are involved. It provides an almost ideal pulse compression of the chirped ultrasonic signals. The resolution obtainable with this method can reach and surpass the limitations of the time references installed in standard equipment (of about 1 in 10^6). In

applications aiming at high precision, equipment relating to established time standards should be employed. The advantage of the presented method has been exemplified by a comparison between compression and correlation scheme.

5.7 References

- [1] K. S. Tarar, "Optimization of chirped input signals and processing of the received signals for optimum time-of-flight resolution in ultrasonic measurements", Master thesis, University of Leipzig, (2005)
- [2] K. S. Tarar, R. Meier, E. Twerdowski, R. Wannemacher, W. Grill, "A differential method for the determination of the time-of-flight for ultrasound under pulsed wide band excitation including chirped signals", Proc. SPIE 693519, (2008)
- [3] C. E. Cook, "Pulse compression-key to more efficient radar transmission", Radar systems 3, 310-315, (1960)
- [4] S. A. Hovanessian, "Radar system design and analysis", Artech House Norwood, (1984)
- [5] A. Sinclair, "An analysis of ultrasonic frequency response for flaw detection: a technique review", Materials evaluation 43, 870-883, (1989)
- [6] F. K. Lam, and M. S. Hui, "An ultrasonic pulse compression system for non-destructive testing using maximal-length sequences", Ultrasonics 20, 107-112, (1982)
- [7] F. K. Lam, "Microcomputer-based digital pulse compression system for ultrasonic NDT", Ultrasonics 25, 166-171, (1987)
- [8] F. K. Lam, and J. Szilard, "Pulse compression techniques in ultrasonic non-destructive testing", Ultrasonics 14, 111-114, (1976)
- [9] X. M. Thanassis, G. Kim, and H. J. Christian, "Potential of coded excitation in medical ultrasound imaging", Ultrasonics International symposium, Lyngby, Denmark, (1999)
- [10] S. Venkatraman, N. A. H. K. Rao, "Combining pulse compression and adaptive drive signal design to inverse filter the transducer system response and improve resolution in medical ultrasound", Med. Biol. Eng. Comput. 34, 318-320, (1996)
- [11] T. H. Gan, D. A. Hutchins, D. R. Billson, and D. W. Schindel, "The use of broadband and acoustic transducers and pulse compression techniques for air-coupled ultrasonic imaging", Ultrasonics, 181-194, (2001)
- [12] J. W. Cooley, and J. W. Tukey, "An algorithm for the machine calculation of complex Fourier Series", Mathematics Computation 19, 297-301, (1965)
- [13] C. E. Shannon, "Communication in the presence of noise", Institute of Radio Engineers 37, 10-21, (1949)
- [14] G. Adlhoch, W. Grill, R. Kociorski, "Verfahren zur Bestimmung der Spannkraft in Verbindungsbauteilen", German Patent (Patentschrift, appl. 2004), (2006)

6. Flaw detection scheme (for aero plane slat tracks)

Here presented is a scheme of signal detection of defects including small dimensional wear and corrosion in slat tracks with the aid of combined ultrasonic and electro-magnetic acoustic transducers (EMATs). The detection scheme relies on the creation of images using the drive needed for operation during scanning. The images are line scans with a second dimension relating to the frequency and parameters leading to different contrast. Among those are differential time-of-flight (TOF) monitoring with respect to a fixed transducer and respectively by using a movable EMAT [1]. The scheme is suitable for in-flight and on-ground monitoring of the structural health of aero plane's slat tracks.

The propagation of ultrasound waves in materials is of particular interest for the non-destructive characterization of materials [2-3]. This problem has been investigated for over a century in mechanics of deformable solid materials [4-5] and has been applied for practical applications. Various theoretical models [6-7] have been proposed for the propagation understanding of surface and guided acoustic waves in isotropic and anisotropic materials. Lamb, Rayleigh and other guided acoustic waves are of prime importance for detection of small changes in the structure of material. For non-inductive plate metals a popular technique in non-destructive testing (NDT) is the mode-selected Lamb wave approach [8] where one specific mode is preferably excited and studied for relative changes with respect to the applied conditions.

Due to the specific design and material nature of slat tracks a combined monitoring with fixed and movable non-contact transducers in combination for scanned inductive monitoring is employed here for integral and local monitoring including in-flight inspection sensitive to possibly reduced structural health and for inspection of cracks and excessive wear.

6.1 The detection scheme

Irregularities at and near the surface can favorably be detected by surface acoustic waves (Rayleigh waves, SAW) if the depth is not substantially smaller than $\frac{1}{4}$ of the wavelength employed. There are two different regimes for monitoring:

1st: Employment of excitations with a rather small wavelength, limited nevertheless by the necessity to use sufficiently low frequencies or sufficiently small distances of propagation to avoid excessive attenuation as to be expected especially from the grease used for lubrication. The small wavelength assures high sensitivity for small cracks.

2nd: Relatively long wavelength but small enough for proper guidance (conditions) with high sensitivity for variations of the local wave propagation velocity with respectively favorably relaxed conditions for distortion by lubricants at the surfaces.

Both methods rely on the assumption, that the defects to be monitored originate at accessible surfaces, sufficiently planar to allow scanned monitoring. Method 1 is especially suited for small distance monitoring with two closely spaced EMATs

(contained in one sensor head). Method 2 is best suited for monitoring with one movable EMAT and one or a pair of fixed transducers.

The here employed detection scheme is based on 2nd method. The involved fixed transducers are positioned at the ends (relating to maximum extension). The movable EMAT is connected to a sliding mechanical motor. For positioning at both ends, high sensitivity load detection can be additionally employed also during flight. The ratio of actual load (detected by conventional devices like accelerometers or piezo-resistive sensors) and monitored stress induced variations of the time-of-flight of ultrasound, can be employed for integral inspection of the mechanical stability and structural health of the entire slat track. This method, even though not capable to determine the position of possible flaws, is also sensitive to internal cracks and cracks not originating at surfaces suitable for scanned monitoring. Based on novel developments implemented here, different modes can be employed for temperature compensation and detection of long term deteriorations (corrosion, wear, creep etc.). This is achieved on the basis of wide band excitation and detection scheme including an improved EMAT design and pulse compression technique [9] in combination with correlation methods for data processing with high temporal resolution (typically at least 10^{-4} of the time for one oscillation of the employed guided waves).

6.2 Improved EMAT design and instrumentation

The most important part in this detection scheme is the specific design of the movable EMAT which has been developed on the basis of demanded task to get an increased magnetic induction at the pointed location for even a very minute scratch on the surface of sample material. The developed EMAT has been employed here to detect smaller dimensional flaws including wear and corrosion preset on the surface of aging aero plane's slat tracks. The following figure (1) shows the details of the EMAT dimensions, material and its assembly.

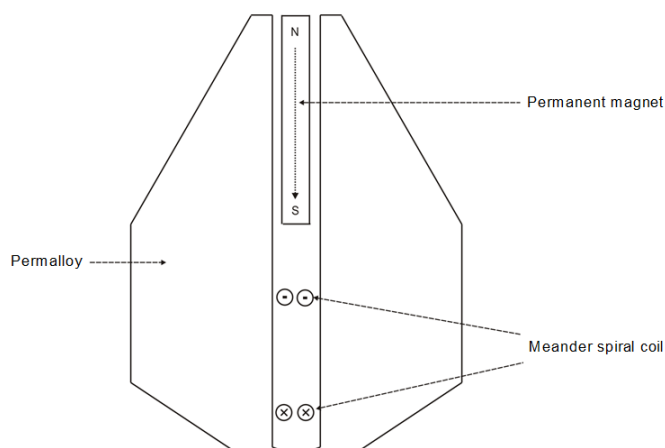


Figure 1: Schematic design [1] of the EMAT which consists of two wedge (L 30mm x W 23mm x T 6.5mm) shaped disks of permendur alloy (1J22) material. These disks have been assembled along with strong permanent magnets (6Pieces: L 10mm x W 5mm x T 2mm) and a current inducing coil.

Signal detection

An EMAT induces ultrasonic waves into a test object with two interacting magnetic fields. A high intensity field generated by electrical coils is applied together with a stable field provided by permanent magnets to generate the wave on the surface of the observed material traveling along the monitored sample (slat track, figure 2).

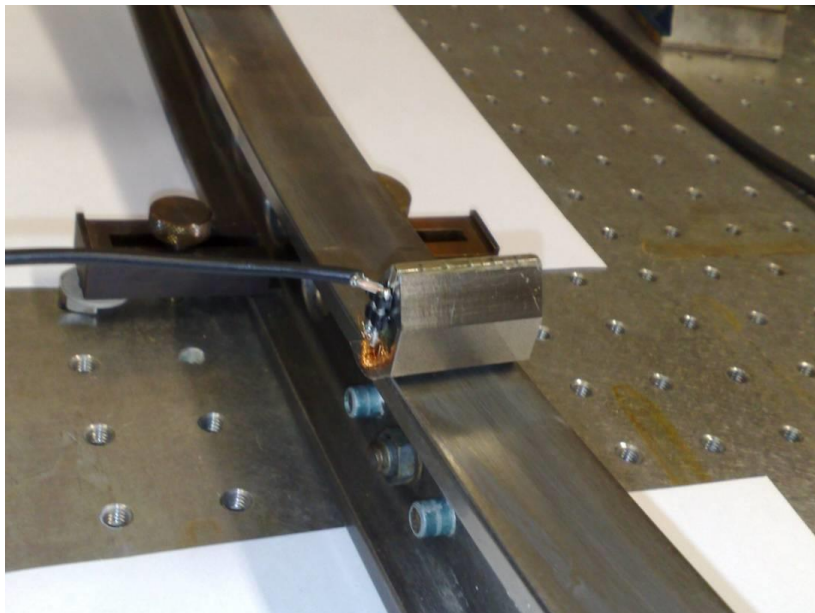


Figure 2:°The developed movable EMAT employed for scanning the slat track shown without assembly to mechanical motor drive.



Figure 3:°The instruments used in experimental set-up with connections including digital oscilloscope (TiePie HS3) and power amplifier.

Signal detection

A basic principle of experimental set-up used in our detection scheme is shown in the following schematic diagram (figure°4).

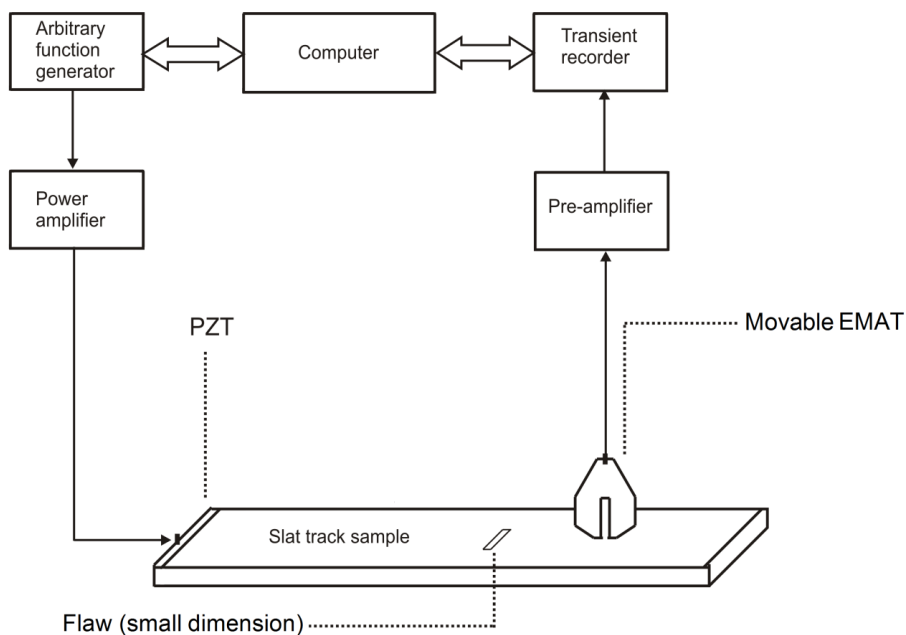


Figure 4:°The schematic diagram of experimental set-up for generation and detection of guided ultrasonic signals with a movable EMAT and fixed transducer (PZT).

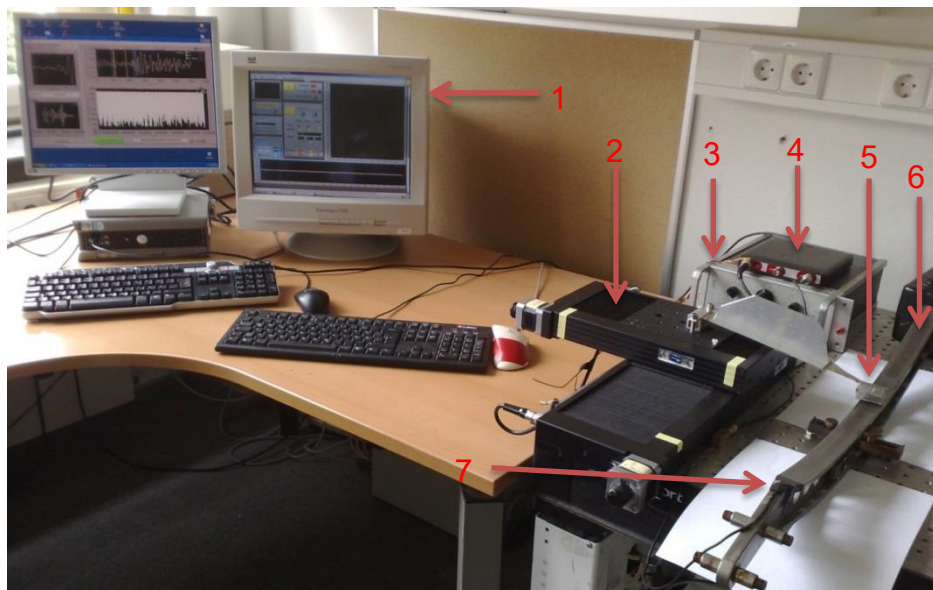


Figure 5:°The complete set-up employed for scanning the slat track during experiment where the listed instruments are as following: 1. Computer with two monitor screens, 2. Computer controlled electric motor, 3. Power amplifier, 4. HS3 digital oscilloscope, 5. Movable EMAT, 6. Slat track of DC9 airplane, 7. Fixed transducer.

Even though an EMAT can equally well be used for detection, it is advantageous in this mixed double ended scheme employing also a piezoelectric transducer to use the EMAT for excitation and generation of signals. The relatively low efficiency can such be counteracted by sufficiently large signals whereas respective amplification needed alternatively for detection would be limited by thermal noise. The high sensitivity employed with the aid of respective low noise preamplifiers and the high suppression of crosstalk achieved by coaxial wiring and respective shielding in part with tri-axial design, assures operation with a rather moderate effective power during excitation of 0.75 W at a duty cycle of only 0.05% which results in an average power of only 0.2 mW of which even only a minor fraction (typically 1%) is converted into ultrasound by the EMAT. This is in a positive way quite unusual for detection schemes based on EMATs and supportive for any in-flight monitoring. Additionally a rolling system is included to position and drive the EMAT. The software, which can operate in real-time, allows to record data and images as displayed in figure 5.

6.3 Application

The operation is based on dedicated LabView® software [10] assuring a high degree of universality and adaptation for future demands. The handling can on one hand be based on manual operation supported by respectively selectable windows for interactive selection of operation. On the other hand fully automatic recording with predefined settings and all required information for the desired mode of operation can be performed. This mode of operation allows among other applications in-flight monitoring including issuing of monitoring information which can include information on critical conditions if an adequately threshold is defined. Interactive operation is demonstrated displaying some of the windows of the respective menu (figure 5).

The sample under investigation is a DC9 (aero plane) slat track made up of grade 5 titanium with dimensions (L 580 mm x W 30 mm x T 50 mm). A motor drive positioned EMAT has been used to excite the signals with a frequency range of 10 kHz to 300 kHz and each line scan step of 1 mm apart. The flaw (wear and corrosion) on the surface of slat track and the fixed wide band transducer at far end are shown in the figures (6, 7) respectively.



Figure 6:°Optical image of wear and corrosion (near center) on the surface of titanium built slat track of a DC9 aero-plane.

Signal detection



Figure 7: Mounting of the stationary (piezoelectric SAW) transducer at the far end of DC9 slat track during experiment.

A digital oscilloscope (TiePie HS3) is used to generate acoustic signals of varying frequencies controlled through (LabView) software program. The signal generated by the movable transmitting EMAT propagates through the slat track (sample) and is received by the (wide band) fixed transducer at far end of the sample. It is then amplified by a low noise preamplifier, digitized by the same oscilloscope unit displaying on computer monitor screen as a function of time (as well as a function of frequency). The signal strength for both time history and frequency spectrum is displayed in Volts. The variation of signal strength vs. time is called time history (or transient curve), and the variation of the signal amplitude vs. frequency is called the spectral plots. During the raw data collection every time step has been averaged by the program for at least 1024 times before being recorded to give a consistent value. The data now is ready to be analyzed, processed or viewed for live monitoring as according to the demand.

Defective region in our case is a wear (and some corrosion) on the surface of the slat track. The aim of this detection scheme is to get increased sensitivity which can detect the flaws of very small dimension. The resultant differential TOF variations of recorded signal transient are shown in the following figure (8).

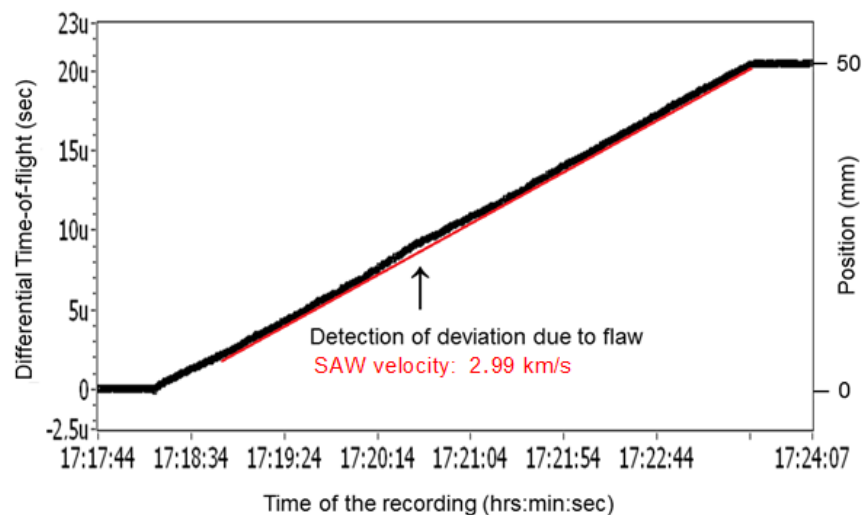


Figure 8: The detection of differential TOF for SAW on a DC9 titanium slat track during experiment [1]. A deviation of TOF can be observed at 17:20:30 on time scale over a total

Signal detection

scanned surface of 50 mm. The here calculated SAW velocity is 2990 m/s and is very close to the literature [11] value of 3000 m/s.

If the recorded signal is reflected by the defect or transmitted through the defect and then reflected back by the sample end then it should be affected by the defect. The graph (figure 8) shows some dependence of TOF on the dimensions of defect. However, it is difficult to estimate the defect size from these small variations of TOF. A better estimation of the defect size can be obtained through Fourier transformations of the transient signals with and without damages, and their respective comparisons. But because these methods are already well established and are in place so it's not the part of present investigation.

6.4 Results

The deviation in the slop of differential time-of-flight in the employed software clearly represents the effective detection capability of the method. But a further sensitivity test of the employed method has been performed by inducing a very small dimension wear (flaw) on the surface of the sample under investigation. The previous wear (or flaw at 150 mm) was relatively of high intensity than the new one on the same slat track surface (figure 9).

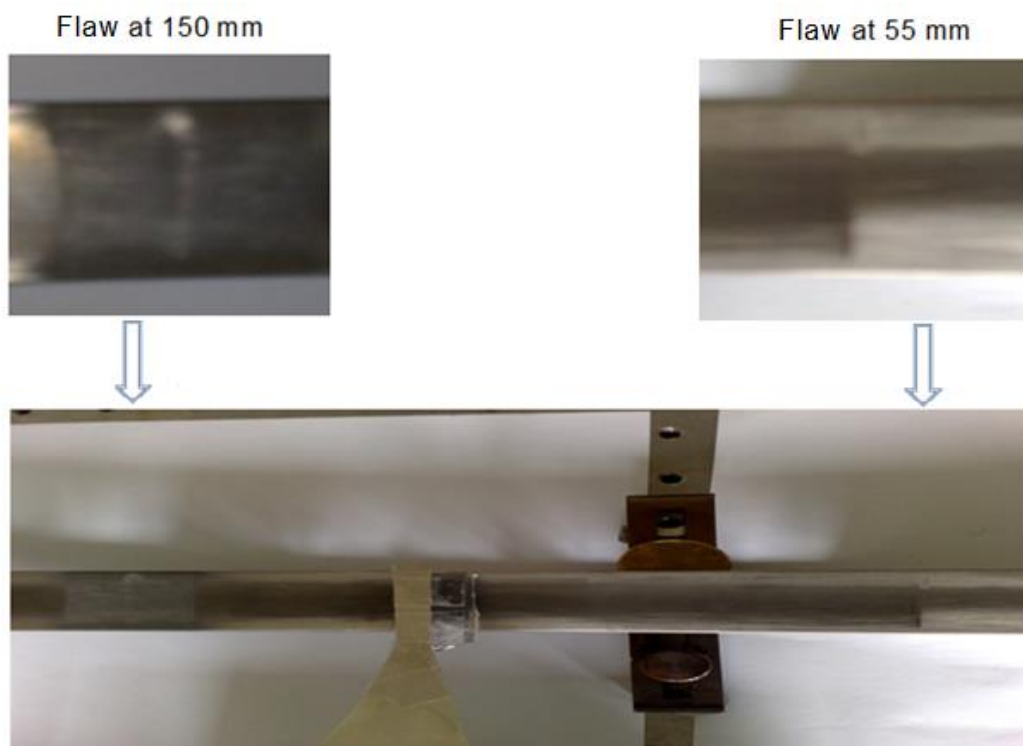


Figure 9: Optical image of DC9 Slat track with both flaws on the surface including magnified images of small dimension (right) and medium dimension (left) shown separately.

The result of transit signal obtained by scanned EMAT generation and detection is displayed in figure°10. A waterfall representation showing the discontinuity at both positions from starting point of scanning has confirmed the successful detection of the flaws and detection scheme's applicability in the structural health monitoring. The flaws are recognizable without any refined signal processing simply by eyesight.

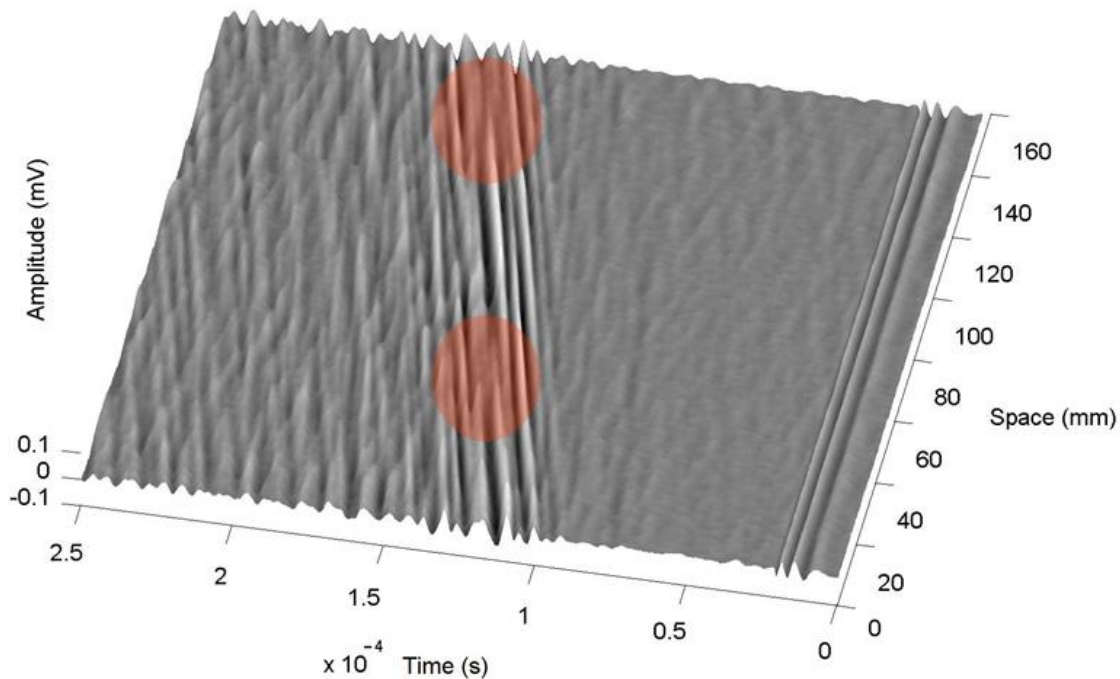


Figure 10: 3D representation of scanned monitoring [1] showing two areas with broken continuity (or interference) marked by red circular cloud. The numerical data also shows a difference of 95 mm between two discontinuities which confirms the original space gap between flaws on the surface of DC9 slat track.

The phenomena of discontinuity of signals due to flaw in the waterfall representation can be explained as: if the recorded signal is dominated by the guided waves propagating through the smooth section then its magnitude should be reduced because a defect creates an obstruction to the propagating energy.

6.5 Comparison with literature

There are a number of methods and techniques available in the literature for mechanical flaw detection in the vital structural and body parts of aero-planes (including slat tracks). For example Mr. H. Boukabache has employed a set of piezoelectric sensors network to demonstrate [12] the feasibility of flaw detection. The technique is vulnerable for application during flight especially during landing and take-off times due to the sensors network limitations towards excessive stress generated at that time. Mr. V. Giurgiutiu has demonstrated [13] the capability of embedded piezoelectric wafer

active sensors (PWAS) for flaw detection in aeronautical parts and structures. He demonstrated S₀, A₀ Lamb wave modes to be most effective for crack and corrosion detection respectively in the metal (and composite) sheets. Again the limitation in this technology is the vulnerability of sensors set-up to the mounting stress generated during landing or take off times. Mr. I. Pitropakis and his colleagues used [14] the electrical crack gauges to monitor flaws in the metallic parts including the slat tracks. With this method the flaws can be monitored when they reach a minimum level of size. This characteristic can also be considered as a limiting factor for this technology as it may not be able to detect the start of a crack or small dimensional wear or corrosion on the surface of slat tracks. Most of the structural monitoring technologies provided in the literature employed for health assessment of aero-plane's body and wing parts are based on piezo-electric transducers and related sensor networks. These transducers are glued to the metal sheets / parts and are vulnerable to the excessive pressures and variation of temperatures during flight.

The here employed non-contact movable EMAT detection technology has the increased ability of countering these effects. For slat tracks manufactured from magnetic materials, magnetically polarized areas at or near the two ends of the devices can be favorably used for the planned application. This avoids any need to glue or fixate by other means transducers such that ultrasound can be coupled effectively. The involved rapidly alternating forces can such be supplied in a non-contact scheme via magnetic fields by nearby electrically driven coils mounted by conventional methods. This method is especially suited for operation under harsh environmental conditions. EMATs are similarly rugged devices as inductive pick-ups used for example regularly for monitoring of the wheel rotational speed for electronically controlled brake systems (Antilock Braking System, ABS) in passenger cars and trucks. The scheme can generate a two or three dimensional image with multi-contrast features and flaw can be distinguishable without any need for refined signal processing simply by eyesight. As marked in figure 10 by circular red clouds at the positions of 55 mm and 140 mm, both flaws are safely detected as clearly identifiable by the discontinuity of the signals in waterfall representation.

6.6 Summary

An inductive monitoring scheme with a (or pair of) fixed transducer and improved movable EMAT has been developed for monitoring of the reduced structural health of slat tracks. The locally resolved monitoring relies for imaging of flaws on the provided drives for activation of the slats. It can be used on ground for periodical rapid inspection but also during flight for quasi-continuous structural health and load monitoring. The developed scheme has successfully shown the ability of its sensitive detection of small dimensional flaws on the surface of slat tracks with a temporal resolution of 10^{-4} of the time per oscillation of the propagating guided waves. The scheme can be a selection of choice for a future early warning system installed on the aircrafts to provide on-board information for the reliability of their structures even during flight. The developed system itself was a part of research [15] for safe air travel supported by European Commission.

6.7 References

- [1] K. S. Tarar, U. Amjad, W. Grill, "Movable EMATs scanning and inductive testing of the slat tracks," , (article in preparation for publication)
- [2] T. Kundu, "Ultrasonic Non-destructive Evaluation: Engineering and Biological Material Characterization", CRC Press, London, (2004)
- [3] D. E. Bray, R. K. Stanley, "Non-destructive Evaluation: A Tool for Design, Manufacturing and Service"; CRC Press, London, (1996)
- [4] Joseph L. Rose, "Ultrasonic Waves in Solid Media", Cambridge University Press, ISBN-13: 978-0521548892, (2004)
- [5] J. David N. Cheeke, "Fundamentals and Applications of Ultrasonic Waves", CRC Press, ISBN-13: 978-1439854945, (2012)
- [6] H. Lamb, "On Waves in an Elastic Plate", Proceedings of the Royal Society of London. Series A 93 (648), pp. 114–128, London, (1917)
- [7] I. A. Viktorov, "Rayleigh and Lamb Waves: Physical Theory and Applications", Published by Springer, ISBN-13: 978-1489956835, (2013)
- [8] K. Hahn, U. Amjad, K. S. Tarar, D. Jha, W. Grill, "Mode selective excitation and detection of Lamb waves", Proc. SPIE 76500D, (2010)
- [9] K. S. Tarar, R. Meier, E. Twerdowski, R. Wannemacher, W. Grill, "A differential method for the determination of the time-of-flight for ultrasound under pulsed wide band excitation including chirped signals", SPIE Proc. 693519, (2008)
- [10] <http://www.ni.com/labview/>
- [11] E. S. Fisher, "US Patent 4313070", (Jan 26th, 1982)
- [12] H. Boukabache, C. Escriba, S. Zedek, J. Y. Fourniols, "Wavlet decomposition based diagnostic for structural health monitoring on metallic aircrafts: Case of crack triangulation and corrosion detection", International Journal of Prognostics and Health Management, ISSN: 2153-2648, 2013 003
- [13] V. Giurgiutiu, "Tuned Lamb wave excitation and detection with piezoelectric wafer active sensors for structural health monitoring", Journal of intelligent material systems and structures, DOI: 10.1177/1045389X05050106, Vol. 16, pp. 291-305, (April 2005)
- [14] I. Pitropakis, H. Pfeifer, T. Gesang, S. Janssens, M. Wevers, "Crack detection in Aluminium 2024-T3 plates and in an Airbus A320 slat-track using electrical crack gauges", WCNDT papers 433, (2012)
- [15] The scheme was developed with financial support of European Union as part of AISHA II (Aircraft Integrated Structural Health Assessment II, EU-FP7-CP 212912).

7. Ultrasonic application (for ablation monitoring of aluminum plate)

A thickness monitoring investigation of aluminum plate is presented here based on the Lamb wave mode selective excitation and detection [1]. The study has its importance due to the increased demand of structural health monitoring (SHM) of the aging aircrafts, and the concern of their surface / structural parts affected by erosion, corrosion, and abrasion etc. with the passage of time. Guided symmetric and anti-symmetric Lamb wave modes selected from the corresponding theoretical dispersion relations of material are excited and studied during gradual thickness reduction of aluminum plate. Results [2] are presented in the form of suitable mode and frequency range. In addition the relevance of theoretically and experimentally derived dispersion graphs and times-of-flight (TOF) assures the reliability of the results presented here.

The demand to increase the workable life of metallic structures, vehicles, and aircrafts is gaining popularity not only due to tough competition in markets, but also due to the large costs associated with new purchases. For aircrafts, many of their structural parts consist of composite laminates. Under cyclic loading, delaminations do occur, compromising the strength of the composite material, causing the material layers to act independently. These delaminations can have catastrophic consequences when they occur especially in load bearing structures. There are many techniques available for detection of delaminations [3-5]. At the same time surface parts are affected due to harsh environmental conditions and do face corrosion and abrasion. These conditions reduce the effective thickness of the metal plate and create ablation. The ablated structural part also creates a potential danger of integrity especially in commercial transporting structures (e.g. aeroplanes and ships). There are a number of techniques in literature [6-8] developed for a sensitive monitoring of metallic (alloys and composites) ablation, however not all can be applied in practical situations. For an aircraft, a suitable scheme must be selected to be able to perform on-ground and in-flight positions simultaneously with optimum result.

An attractive ultrasonic structural health monitoring scheme is the use of guided Lamb waves [9-12]. The main advantage of Lamb waves is that they interrogate the entire thickness of the specimen along the line joining the transmitter and the receiver, hence, making them very useful for large area scanning. Another advantage is their ability to propagate on the surface with less loss of energy. In the current investigation TOF of the Lamb waves has been measured in 5 mm, 3 mm, and 1 mm thick aluminum plate during its three stages of ablation. The progressive ablation phenomena can determine the projected safety level of the material being used.

7.1 The ablation scheme

The basic concept of the scheme applied here can most easily be explained under simplifying symmetric conditions: Any ablation will lead to a reduction of the effective thickness of the original material skin. This is illustrated here (figure 1) under the assumption that the material plate has an ablation in the center and is such separated into two identical plates. For example if the fundamental symmetric and anti-symmetric Lamb wave modes undergo ablation such that it leads to a decrease of the effective

thickness by a factor of 1/2, the result with parallel propagation of the ultrasonic modes in each fragment can be represented as indicated in figure 1.

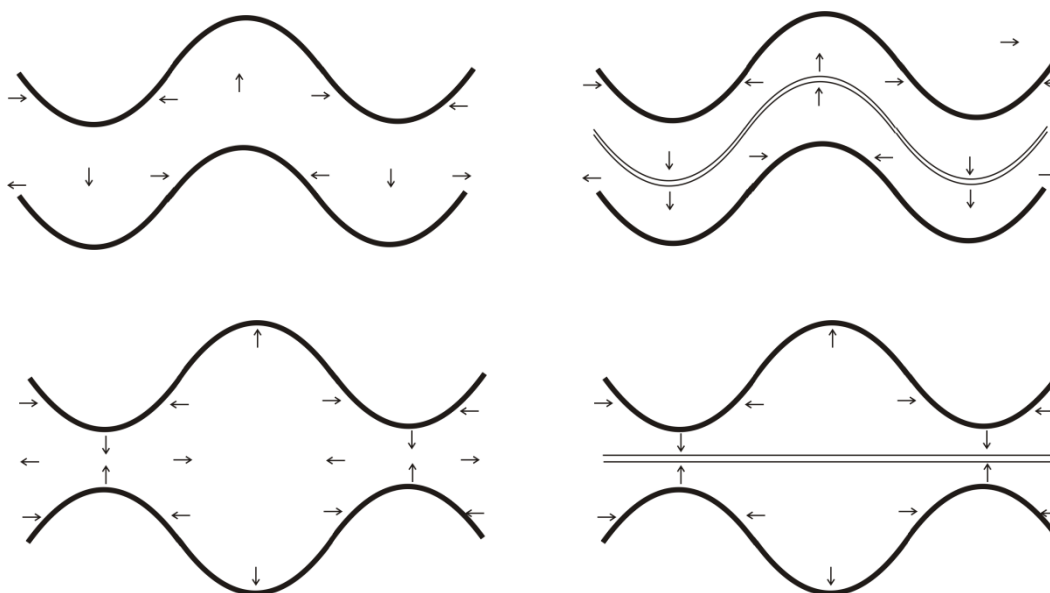


Figure 1: Expected deformation and particle velocity (arrows) of the A0- (top) and S0- (bottom) mode before (left) and after (right) ablation process. Whereas the A0-mode needs, concerning the illustrated properties, no adjustment to the split-condition, the S0-mode on each fragment has to undergo re-adjustment to symmetrical conditions as illustrated here only for the intact sample.

In the case of a single ablation parallel to the surfaces the fractions are then 'a' and '1-a' for any 'a' between 0 and 1. Rather small 'a' close to 0 represents in close approximation surface ablation with total removal of the thin component, which will, even if assumed to be still in place, not contribute significantly to the transport properties used for monitoring. Ablations parallel to the direction of propagation can be resembled to abrasion and corrosion, and can be detected, since the transit signal will vanish or be significantly reduced for resultant effective thickness.

7.2 Instrumentation

An essential ingredient for high resolution thickness monitoring with guided ultrasonic waves is the mode selective generation and detection scheme [1] with broad band transducers (figures 2, 3). A schematic diagram of the experimental set-up is shown in the following figure (4).

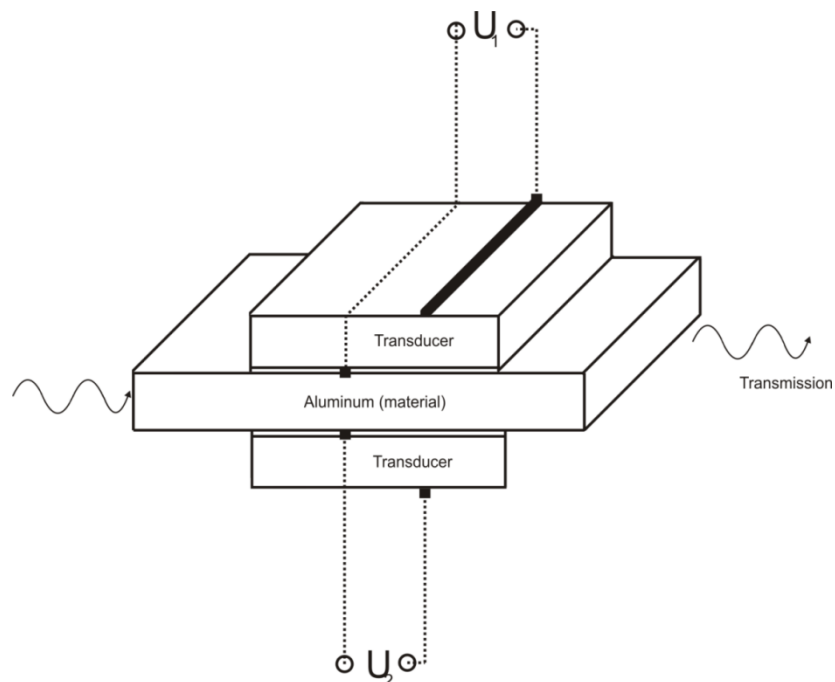


Figure 2: Design and installation of two piezoelectric vertical polarized discs including electrical contacting (U_1 , U_2) of broad band mode selective transducer [13-14].

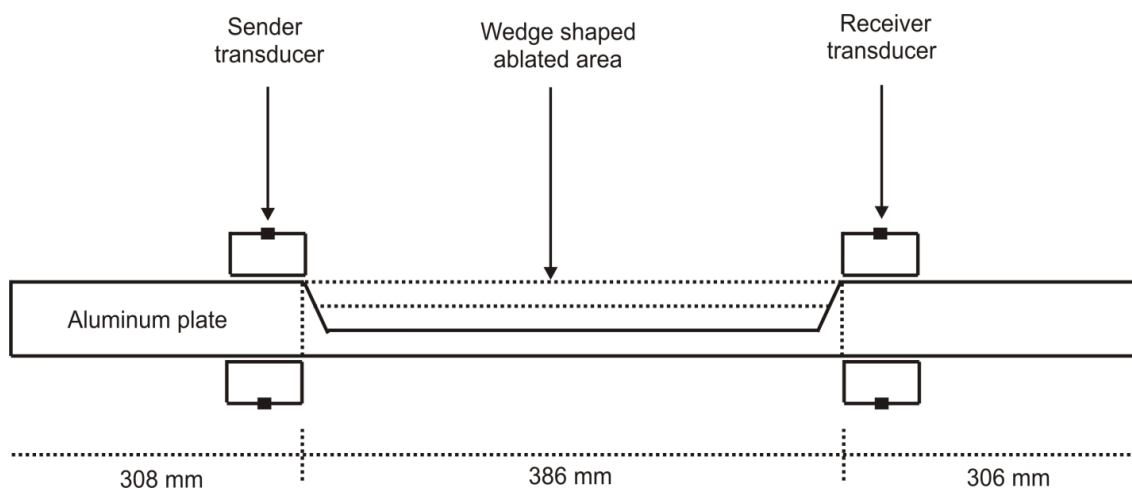


Figure 3: The schematic diagram [2] representing aluminum plate with broad band transducers, ablated area and respective dimensions.

The dimensions of the broad band transducers employed are 20 mm X 10 mm X 1 mm (Length X Width X Thickness). These transducers consist of piezoelectric sintered heterogeneous ceramic materials manufactured from modified Lead Zirconate Titanate (PZT) and Barium Titanate material. The dimensions of the aluminum (density = 2700 Kg/m³, Young's modulus = 70 GPa) plate sample are 1000 mm X 20 mm X 5 mm. The length of ablated part is 386 mm from the edges of sender to receiver transducers. Two

wedges of 9 degree have been induced on both sides of the aluminum plate near transducers to provide a better propagation of Lamb waves through the ablated area (figure 3). The non-ablated lengths of aluminum plate near sender and receiver transducers towards respective extreme plate edges are 308 mm and 306 mm respectively. The aluminum plate was placed on Styrofoam to maintain the level and stress-free boundary environment. The entire set-up was secured in a thermal chamber to avoid any change in TOF due to variation in temperature. Two broad band transducers were attached on two sides of the aluminum plate for the generation and detection of Lamb waves by using two piezoelectric vertical polarized discs on each side (figure 3).

To develop high frequency broad band transducer [13-14], two silver line electrodes were rigidly attached to the piezoelectric discs at a distance one-fourth of its length from the direction of propagation of the wave. During excitation the PZT causes vibration inducing wave propagation on the surface of plate sample. The narrow thickness of the electrodes produces the higher frequency [14] response. The one-fourth distance of electrode from the edge of the transducers ensures the separation of lateral resonance from the thickness resonance of the PZT and facilitates the maximum travel of energy in the direction of Lamb waves.

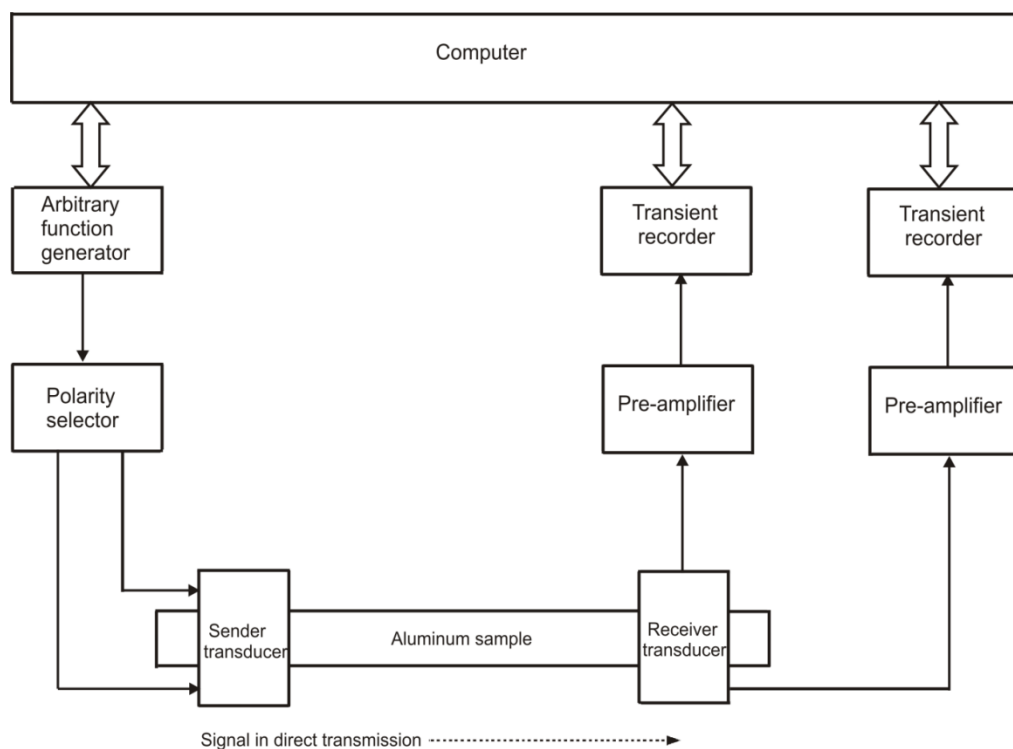


Figure 4: The schematic diagram for signal generation and detection demonstrating the actual implementation of scheme [2].

For mode selective signal generation, an inverting unity gain amplifier is employed for selective reversal of the signal phase supplied to one of the two opposing sender

transducer discs. For signal detection, two transient recorder channels (figure 4) are used with additive or subtractive processing including fine adjustment for relative delay and sensitivity. The operation of the broad band transducers (figure 2) applied here to generate Lamb waves have already been discussed in detail in the literature [13-14].

7.3 Application

A set of symmetric and anti-symmetric Lamb wave modes are generated and detected to observe the related effects of gradual reduction of effective thickness of the aluminum plate. Theoretical group velocity dispersion curves for respective Lamb wave modes are generated by a software named disperse [15] for specific material, and dimensions. The achieved data is converted into TOF data by dividing it to the total length of the sample. A comparison of symmetric and anti-symmetric Lamb wave modes for different thicknesses of aluminum plate has already been provided in the literature [3, 16] and suggested a low frequency range would be sufficient for this investigation. The data plotting is limited up to 2 MHz and the respective results are analyzed.

For signal processing the Fast Fourier Transformation (FFT) on symmetric and anti-symmetric transient responses was performed to identify the dominant frequencies and Lamb modes of the guided acoustic waves. The frequency spectra indicate the multiple modes of dispersion. However global FFT will lead to a loss of temporal resolution. To overcome this effect, Short-Time Fourier Transformation (STFT) was performed on symmetric and anti-symmetric transient responses to generate from the experimental results the dispersion relations for the sample material under investigation. In STFT the entire time domain signal is broken down into short time period intervals. The short signals are selected with a Hanning window and FFT is performed subsequently. With the aid of the determined individual Fourier spectra the dispersion relations are displayed in spectrograms. By STFT the resolution of either time or frequency will be limited as pointed out for the general case by Heisenberg's uncertainty principle. The time-frequency information depends on the size of the window. A wider window will provide higher frequency resolution but the time resolution will be reduced and vice versa.

7.4 Results

Numerical data for theoretical dispersion curves of Lamb waves for 5 mm, 3 mm, and 1 mm thick aluminum plate is generated by disperse (software). The experimentally obtained dispersion spectrograms of symmetric and anti-symmetric Lamb wave modes are superimposed on the theoretically obtained dispersion curves for the corresponding thicknesses of the aluminum plate.

a). Anti-symmetric modes

The following spectrograms represent the frequencies and corresponding TOF for anti-symmetric modes in the range of 1 kHz to 2 MHz (figures 5, 6, 7).

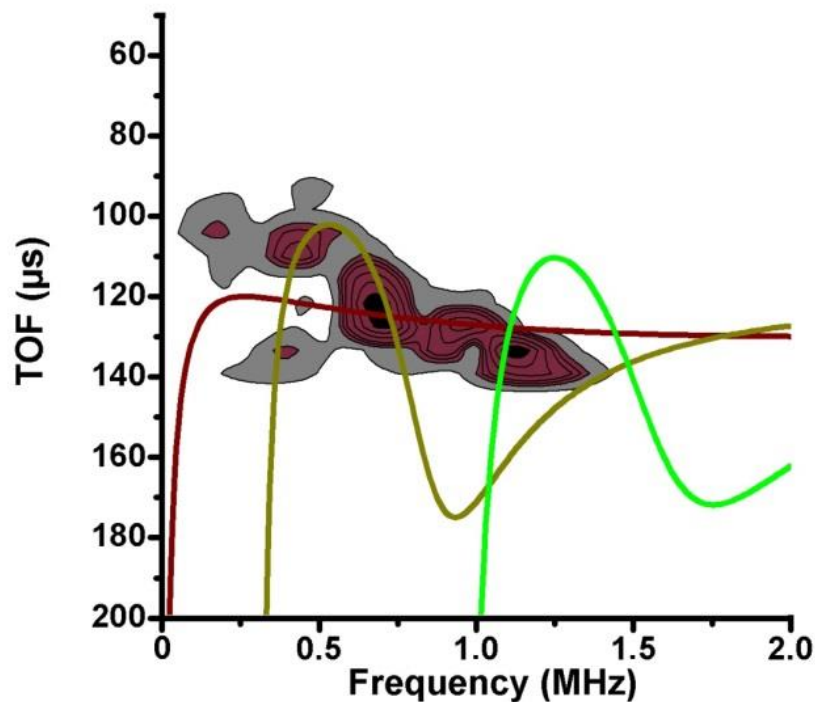


Figure 5: Anti-symmetric Lamb wave modes propagation in 5 mm thick aluminum plate with the theoretical results as shown by color continuous lines while the experimental results [2] are represented by contour plots. The coloring intensity represents the intensity of energy the modes possess in the respective frequency range. The color lines representing the modes are: A0 = Maroon line, A1 = Olive line, A2 = Green line.

In figure 5, we can see from theoretical and experimental superimposed dispersion graphs that a strong (anti-symmetric) A0 mode has been generated by broad band transducers between 0.3 MHz to 1.4 MHz frequency range. This energy contribution is also shared by A1 and A2 modes, where the frequency range for A1 mode is from 0.3 MHz to 0.8 MHz, and for A2 mode is from 1 MHz to 1.4 MHz. The experimental spectrogram shows strong shared contributions of A1 mode along with A0 mode at 0.7 MHz, and A2 mode along with A0 mode at 1.1 MHz. In this graph (figure 5), the A0 mode has been found more dominant towards propagating Lamb wave energy contributions in 5 mm thick aluminum plate.

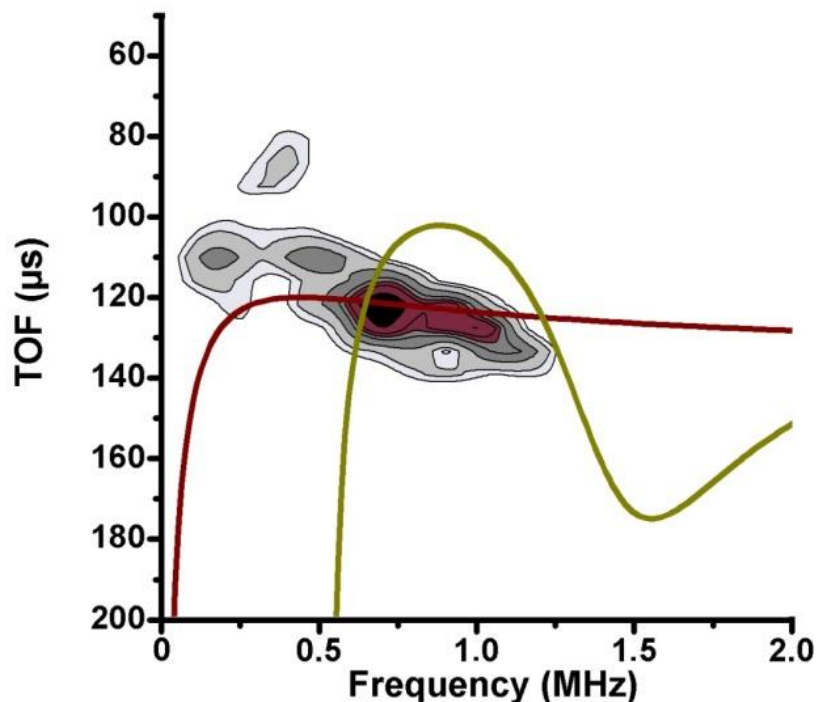


Figure 6: Anti-symmetric Lamb wave modes propagation in 3 mm thick aluminum plate with the theoretical results as shown by color continuous lines while the experimental results [2] are represented by contour plots. The coloring intensity represents the intensity of energy the modes possess in the respective frequency range. The color lines representing the modes are: A0 = Maroon line, A1 = Olive line.

In figure 6 the aluminum plate has been ablated to 3 mm thickness. The graph shows the strong energy between frequency ranges of 0.4 MHz to 1.4 MHz which is shared by A0 and A1 modes. It is clearly visible from the graph that most of the energy contribution comes from A0 mode and the A1 mode provides only small contribution while A2 mode is completely absent in this range. This graph analysis provides A0 mode as more energy carrying mode and more suitable for ablation monitoring of aluminum plates.

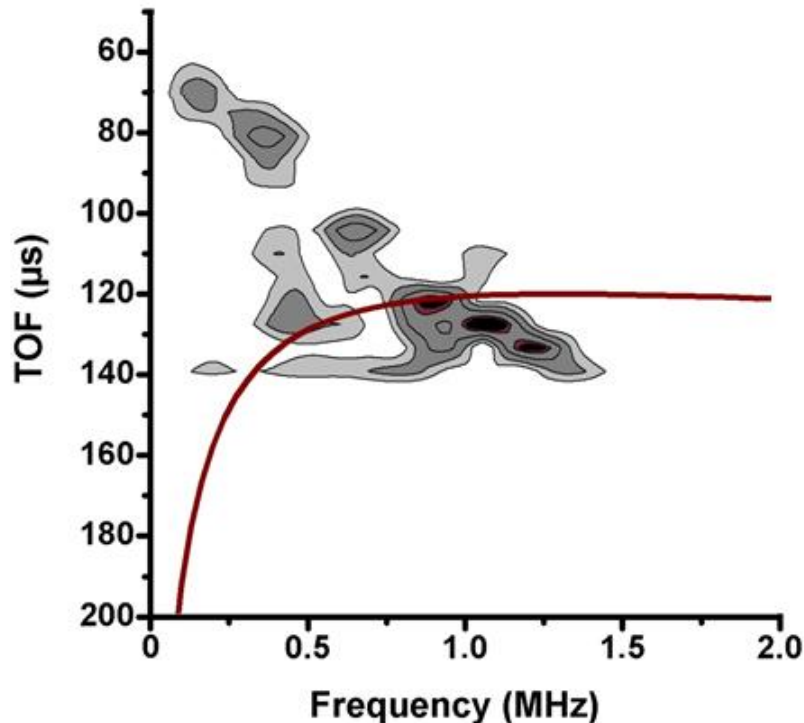


Figure 7: Anti-symmetric Lamb wave modes propagation in 1 mm thick aluminum plate with the theoretical results as shown by color continuous lines while the experimental results [2] are represented by contour plots. The coloring intensity represents the intensity of energy the modes possess in the respective frequency range. The color lines representing the modes are: A0 = Maroon line.

In figure 7 the aluminum plate has been further ablated to 1 mm thickness. The graph shows the relatively stronger energy between frequency range of 0.7 MHz to 1.4 MHz which is only contributed by A0 mode. The A1 and A2 modes are not even visible in this frequency range. This graph (figure 7) analysis also proves the more sensitive nature of A0 mode for aluminum ablation monitoring.

b). Symmetric modes

The following spectrograms represent the frequencies and corresponding TOF for symmetric modes in the range of 1 kHz to 2 MHz (figures 8, 9, 10).

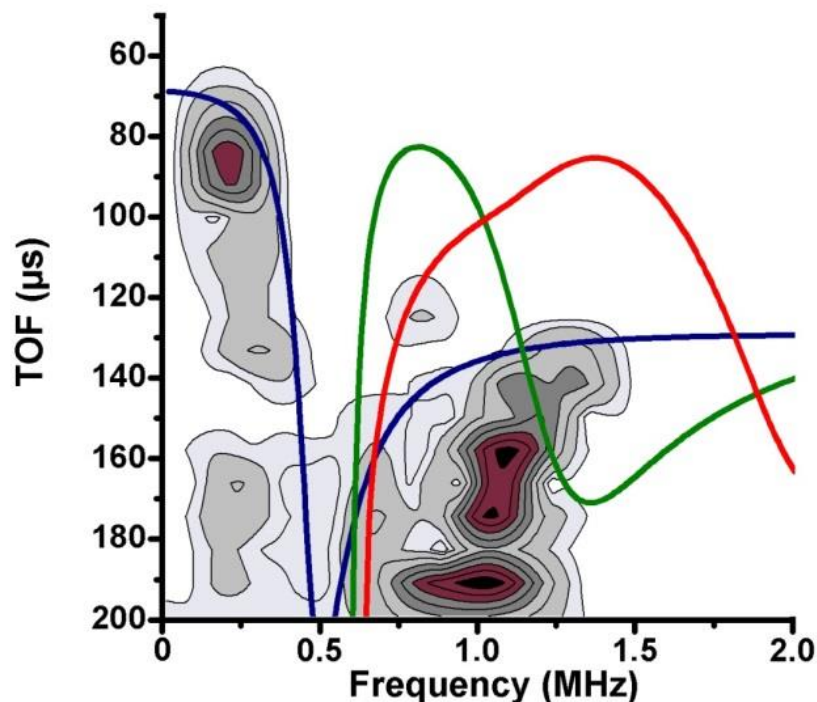


Figure 8: Symmetric Lamb wave modes propagation in 5 mm thick aluminum plate with the theoretical results as shown by color continuous lines while the experimental results [2] are represented by contour plots. The coloring intensity represents the intensity of energy the modes possess in the respective frequency range. The color lines representing the modes are: S0 = Dark Blue line, S1 = Dark Green line, S2 = Red line.

In figure 8, we can see three strong energy contributions from three symmetric (S0, S1, S2) modes. Only the S0 Lamb mode energy contribution between frequency range of 0.1 MHz to 0.4 MHz is found to be more (or nearest) matching to the theoretical dispersion curves. Relatively less match-able energy contributions from S0 mode shared with S1 and S2 modes are found near 0.6 MHz and 0.65 MHz respectively. The two stronger energy contributions found between 0.8 MHz to 1.2 MHz are, however not match-able to theoretical dispersion curves and therefore are not taken into consideration. The analysis of this graph (figure 8) suggests S0 mode a better option for ablation monitoring of aluminum amongst other symmetric modes.

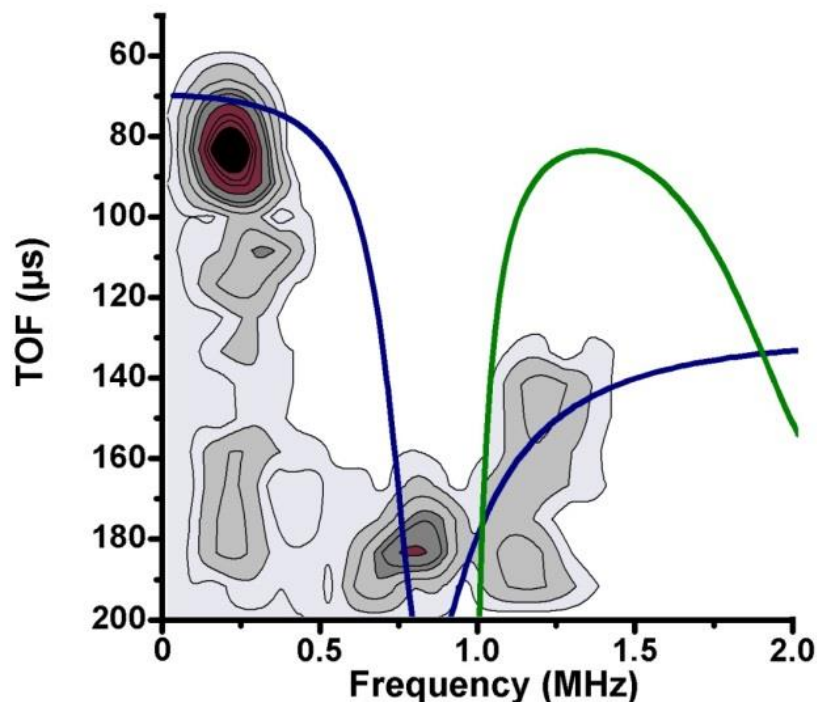


Figure 9: Symmetric Lamb wave modes propagation in 3 mm thick aluminum plate with the theoretical results as shown by color continuous lines while the experimental results [2] are represented by contour plots. The coloring intensity represents the intensity of energy the modes possess in the respective frequency range. The color lines representing the modes are: S0 = Dark Blue line, S1 = Dark Green line.

In figure 9 the aluminum plate has been ablated to 3 mm thickness. The graph shows a strong energy contribution between frequency range of 0.1 MHz to 0.4 MHz provided by the S0 mode only. Also a relatively lesser energy contribution has been found by S0 mode between the frequency range of 0.65 MHz to 0.85 MHz. A weak shared energy contribution of S0 and S1 modes is found near 1 MHz but is negligible in its effect and is not consider for analysis. This graph (figure 9) shows the S0 mode as more suitable option for aluminum ablation monitoring.

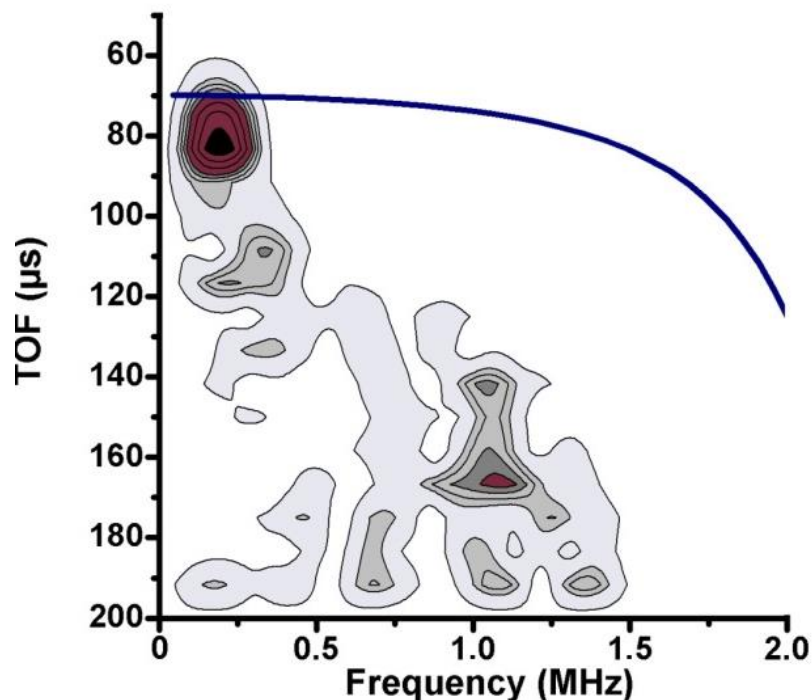


Figure 10: Symmetric Lamb wave modes propagation in 1 mm thick aluminum plate with the theoretical results as shown by color continuous lines while the experimental results [2] are represented by contour plots. The coloring intensity represents the intensity of energy the modes possess in the respective frequency range. The color lines representing the modes are: S0 = Dark Blue line.

In figure 10 the aluminum plate has been further ablated to 1 mm thickness. The graph shows a strong energy contribution between the frequency range of 0.1 MHz to 0.4 MHz provided by the S0 mode only. There is another visibly less strong energy contribution in this graph between 1 MHz to 1.2 MHz but is not match-able with theoretical dispersion curves and so is not considered for further analysis. This graph (figure 10) also shows the S0 mode as more sensitive to the gradual thickness reduction monitoring of aluminum plate comparing to other symmetric modes.

c). Comparison of the spectrograms of symmetric and anti-symmetric modes

During the progressive ablation process of the aluminum plate (5 mm, 3 mm, 1 mm), experimental in combination with the theoretically derived symmetric and anti-symmetric modes are analyzed and the following facts are found during this investigation.

- In both cases the fundamental symmetric (S0) and anti-symmetric (A0) modes are found more reliable for ablation monitoring of aluminum plate.
- The best frequency range for anti-symmetric modes during ablation monitoring has been found between 0.7 MHz to 1.4 MHz.
- The best frequency range for symmetric modes during ablation monitoring has been found between 0.1 MHz to 0.4 MHz.
- There are some strong energy contributions found in the symmetric experimental graphs which could not be explained through theoretical dispersion graphs. The most possible reason is the side boundary effects of propagating Lamb waves at low frequencies.
- The anti-symmetric mode experimental dispersion graphs are more match-able with their corresponding theoretical dispersion graphs especially for strong energy contributions.
- These spectrograms reveal that anti-symmetric A0 mode has more variation of energy than the symmetric S0 mode representing its more sensitive nature towards thickness variation, and can be better result giving in case of application for ablation monitoring of aluminum plates.

This comparison of symmetric and anti-symmetric Lamb modes with progressive ablation of aluminum plate has provided (anti-symmetric) A0 mode as the most suitable mode with in the frequency range of 0.7 MHz to 1.4 MHz.

7.5 Comparison with literature

Some of the literature produced for sensitive ablation monitoring of aluminum plates is related to Laser detection based techniques [17-19]. These techniques even though are quite sensitive to ablation process, involve metal processing (e.g. evaporation, laser induced plasma) and in some cases other than the dry conditions, which are not suitable in our case for online structural health monitoring. Another closely related application to ablation monitoring of aluminum plates (or their composites) is the delamination monitoring. There are a number of applications provided in the literature for delamination monitoring [3, 20-22] of aluminum plates. As delamination is a process of two or more than two layers of material dis-joining, which in most cases are joined by a gluing fluid, the dynamics of delamination cannot be directly compared with ablation process due to gluing material or gap between laminated layers involved. The presented study proves the suitability of the applied (mode selective generation and detection) technique for ablation monitoring of aluminum plates relating to the SHM of aircraft surface / structural parts.

7.6 Summary

In this chapter the ablation of aluminum plates has been investigated [2] by employing selective symmetric and anti-symmetric Lamb wave modes. The mode selective generation and detection scheme [1] has been chosen due to its dry contact suitability for aircrafts, and can be employed simultaneously on-ground and in-flight positions. The frequencies and modes are selected from the respective theoretical dispersion relations

of the material and thickness. The ablation detection is performed on the basis TOF measurement of Lamb waves. The experimentally obtained spectrograms consist of energy contour plots and are superimposed on theoretical dispersion graphs. A careful analysis of symmetric and anti-symmetric modes of various frequency ranges has revealed the S0 and A0 modes to be the most sensitive in nature. The observation is based on the variation of mode's energy due to ablation process in the respective (experimental) spectrograms in combination with theoretical dispersion graphs. A final comparison of both fundamental (S0 and A0) Lamb wave modes has suggested A0 mode within the frequency range of 0.7 MHz to 1.4 MHz, to be the most suitable for ablation monitoring in aluminum plates, for a maximum thickness of 5 mm. The presented investigation has direct applications in SHM of large metallic alloy and composite structures (bridges, pipe lines) and has been financed by AISHA II [23].

7.7 References

- [1] K. Hahn, U. Amjad, K. S. Tarar, D. Jha, W. Grill, "Mode selective excitation and detection of Lamb waves", Proc. SPIE 76500D, (2010)
- [2] K. S. Tarar, U. Amjad, W. Grill, "Progressive ablation of 5 mm thick aluminum plates using mode selective excitation and detection of ultrasonic guided waves", (article in preparation for publication)
- [3] A. Shelke, T. Kundu, U. Amjad, K. Hahn, W. Grill, " Mode-selective excitation and detection of ultrasonic guided waves for delamination detection in laminated aluminum plates", Ultrasonics, Ferroelectrics, and Frequency Control, IEEE Transactions on, Vol. 58 (3), pp. 567-577, (2011)
- [4] P. Cawley, "Low Frequency NDT Techniques for the detection of disbonds and delamination", British Journal of NDT, Vol. 32 (9), pp. 454-460, (1990)
- [5] N. Guo, P. Cawley, "Interaction of Lamb waves with delaminations in composite laminates", Journal of the Acoustical Society of America, Vol. 94, pp. 2240-2246, (1993)
- [6] J. Pei, M. I. Yousuf, F.L. Degertekin, B. V. Honein, B. T. Khuri-Yakub, "Lamb wave tomography and its application in pipe erosion/corrosion monitoring", Research in Non-destructive Evaluation, Vol. 8 (4), pp. 189-197, (1996)
- [7] R. J. Dewhurst, C. Edwards, A. D. W. McKie, S. B. Palmer, "Estimation of the thickness of thin metal sheet using laser generated ultrasound", Applied Physics Letters, Vol. 51, (1987)
- [8] Y. Hayashi, S. Ogawa, H. Cho, M. Takemoto, "Non-contact estimation of thickness and elastic properties of metallic foils by the wavelet transform of laser-generated Lamb waves", Ndt & E International 32, 21-27, (1999)
- [9] H. Lamb, "On Waves in an Elastic Plate", Proceedings of the Royal Society of London. Series A 93 (648), pp. 114–128, (1917)
- [10] D. Worlton, "Ultrasonic testing with lamb waves. Non-destructive test", Vol. 15, pp. 218–22, (1957)
- [11] I. Viktorov, "Rayleigh and Lamb waves", Plenum Press; New York USA, (1967)

- [12] S. S. Kessler, S. M. Spearing, C. Soutis, "Damage detection in composite materials using Lamb wave methods", *Smart materials and structures*, Vol. 11 (2), pp. 269–278, (2002)
- [13] U. Amjad, K. Hahn, T. G. Tang, W. Grill, "Non-inertial ultra-wideband acoustic transducers", *Proc. SPIE 7295*, (2009)
- [14] K. Hahn, "Strukturierte piezoelektrische Transducer zur modenselektiven Erzeugung und Detektion geführter Ultraschallwellen", *Diplomarbeit, Universität Leipzig*, (2009)
- [15] B. Pavlakovic, M. Lowe, D. Alleyne, P. Cawley, "Disperse: A general purpose program for creating dispersion curves", *Review of Progress in Quantitative Non-destructive Evaluation*, Vol. 16, pp. 185-192, (1997)
- [16] U. Amjad, K. S. Tarar, A. Shelke, M. Pluta, T. Kundu, W. Grill, "Generalized representations and universal aspects of Lamb wave dispersion relations", *Proc. SPIE 76502F*, (2010)
- [17] Y. M. Lai, N. H. Cheung, "Pulsed laser-induced damage threshold studies of thin aluminum films on quartz: Simultaneous monitoring of optical and acoustic signals", *Review of Scientific Instruments*, Volume 64 (6), pp. 1606-1610, (1993)
- [18] F. P. Mezzapesa, V. Spagnolo, A. Ancona, G. Scamarcio, "Detection of ultrafast laser ablation using quantum cascade laser-based sensing", *Applied Physics Letters* 101, 171107 (2012)
- [19] H. Sobrala, M. V. Muniz, "Energy balance in laser ablation of metal targets", *Journal of Applied Physics* 98, 083305 (2005)
- [20] S. C. Rosalie, M. Vaughan, A. Bremner, W. K. Chiu, "Variation in the group velocity of Lamb waves as a tool for the detection of delamination in GLARE aluminum plate-like structures", *Composite Structures* 66, pp. 77–86, (2004)
- [21] N. Guo, Peter Cawley, "The interaction of Lamb waves with delaminations in composite laminates", *Journal of the Acoustical Society of America* 94 (4), pp. 2240-2246, (1993)
- [22] K. Maslov, T. Kundu, "Selection of Lamb modes for detecting internal defects in composite laminates", *Ultrasonics* 35, pp. 141-150, (1997)
- [23] European Union project under the 7th framework program within AISHA II (Aircraft Integrated Structural Health Assessment II, EU-FP7-CP 212912)

8.1 Structural health stability and stress monitoring by ultrasound

Structural Health Monitoring (SHM) has gained increasingly higher importance in recent decades, particularly in the aerospace industry and civil engineering. Various SHM systems have already been developed for numerous potential applications. Despite all of these significant recent advancements, there still is a need of scientific understanding and of the development of new applications, which was the motivation of this research. The presented dissertation has been the effort to provide an extended scientific insight to this multi-disciplinary field.

The main focus of this dissertation lies in theoretical modeling of the acoustic wave propagation in isotropic solid media under defined stressed conditions, also including the ultrasonic signal processing and detection schemes and respective applications.

All contributions are individually addressed, discussed and their conclusions are summarized in each of the respective chapters. This chapter has been placed to briefly summarize all of these contributions to make a conclusive statement:

8.2 Summary of the performed work

The dissertation can generally be divided into two main sections. The first section is mainly theoretical and starts with an analytical comparison of microscopic (discrete model) and macroscopic (continuum model) approaches for the stress dependence of the time-of-flight (TOF) of bulk and guided acoustic waves in solid materials. The discrete modeling is given preference on the basis of its better capability to explain the stress dependence of acoustic waves in the anharmonic conditions.

The physics behind the acoustic wave's propagation through solids under stressed conditions is simulated by employing mass spring lattice dynamic (MSLD) modeling. This approach is used here to exemplify the nature of the effects involved in stress or load detection. The effects caused by anharmonicity are also included to present a generalized modeling solution. The two linear chain mass-spring (discrete) models for longitudinal -(resembling S0) and transversal -(resembling A0) polarized acoustic modes are presented to demonstrate their individual responses upon external stress. Whereas the unified discrete model can demonstrate the variations in the velocity and TOF of bulk acoustic waves with and without external pull at long wavelengths for a combined treatment of both of the fundamental mode's propagation. Generally the prominent feature of the longitudinally polarized acoustic modes is that the TOF will remain constant for idealized (material) conditions at low frequencies under the influence of extensional stress and under the same conditions a decrease in TOF is resulted for transversely polarized acoustic modes.

Similarly, an upgraded model (with next neighbor mass-spring coupling) is used to simulate the guided acoustic wave's propagation in isotropic solid media demonstrating the combined effects of longitudinal and transversal polarized modes under extensional stress. The anharmonicity factor has been added by employing Lennard-Jones binding potential dependent lattice function. Due to its more sensitive nature to the extensional stress, the focus is given to the fundamental anti-symmetric (A0) Lamb wave mode. The provided modeling has been analyzed by deriving frequency dependent physical

Conclusions

parameters and comparing them to their relevant continuum model. A close matching between the results of discrete and continuum models has been found. The theoretical results are further verified analytically by developing an elastic coupling function and comparing it with the experimental results.

The second section consists of two ultrasonic signal processing and detection schemes, and an ultrasonic monitoring application of ablation process. The first one is a pulse compression scheme for the determination of differential measurements of the time-of-flight of ultrasound. The scheme takes care of corrections of phase and amplitudes for optimum pulse compression in applications where small variations of time-of-flight are involved. It can provide an almost ideal pulse compression of the chirped ultrasonic signals. The resolution obtainable with this method can reach and surpass the limitations of the time references installed in standard equipment (of about 1 in 10^6). The comparison with respective results obtained by correlation scheme exhibits the advantages of the developed compression scheme for chirped signals. The width of the center lobe and the relative height of the side lobes are both favorable for the developed scheme. The dominant disadvantages of the correlation scheme are the large side lobes, which can lead to a mix up of the peaks (jump of the global maximum to a former side peak), and in the application presented here, this would lead to an error of more than 200 ns.

The developed detection scheme is based on the inductive monitoring of wedge shaped movable EMAT in combination with a (or pair of) fixed transducer primarily designed for aero plane slat tracks. The specific shape and fabrication of EMAT with permender alloy maximizes its local detection capability. The monitoring relies for imaging of flaws on the provided drives by activation of the slat tracks. It can be used, not only on ground for periodical rapid inspection, but also during flight for quasi-continuous structural health and load monitoring. The developed scheme has successfully shown the ability of its sensitive detection of small dimensional flaws with a temporal resolution of 10^{-4} of the time per oscillation of the propagating guided waves.

The ultrasonic application consists of an ablation monitoring of aluminum plate by employing mode selective generation and detection scheme. This scheme has been chosen due to its dry contact suitability for aircrafts. Guided symmetric and anti-symmetric Lamb wave modes selected from the corresponding theoretical dispersion relations of material are excited and recorded during gradual thickness reduction of aluminum plate. The experimentally obtained spectrograms are superimposed on theoretical dispersion graphs. In addition the relevance of theoretically and experimentally derived dispersion graphs and times-of-flight assures the reliability of the results presented here. A careful analysis has suggested the fundamental anti-symmetric (A_0) Lamb wave mode within the frequency range of 0.7 MHz to 1.4 MHz, to be the most suitable for ablation monitoring in aluminum plates, for a maximum thickness of 5 mm. The presented study has its importance due to the increased demand of structural health monitoring of the aging aircrafts affected by erosion, corrosion, and abrasion etc. with the passage of time.

8.3 Contributions to the advancement of the state of the art

The main contributions of this dissertation to the advancement of the state of the art are briefly listed as following:

- Development and implementation of a generalized lattice dynamic modeling based theory for acoustic waves propagation in isotropic solid materials under defined stressed conditions
- Demonstration of the applicability of this theory for the prediction of reaction of two fundamental symmetric and anti-symmetric modes of acoustic waves in homogeneous solid materials under defined stressed conditions
- Development and implementation of novel ultrasonic signal and data processing technique
- Development and implementation of in-flight structural health acoustic monitoring techniques

9. Appendices:

Following are some of the solved equations used in the dissertation. They are chapter wise organized:

Appendix 2.1 (Derivation for $dt/t = dl/l - dv/v$)

By definition in the absence of acceleration

$$v = l/t$$

and therefore after deformation, where all values have changed by a respective “d”

$$t = l/v$$

$$\text{and } t+dt = (l+dl) / (v+dv)$$

From this result:

$$(t+dt)/t = ((l+dl)/l) / ((v+dv)/v)$$

$$1+dt/t = (1+dl/l) / (1+dv/v)$$

$$1+dt/t = (1+dl/l) / (1+dv/v)$$

Multiply “top” and “bottom” of right side with $(1-dv/v)$

$$1+dt/t = (1+dl/l) (1-dv/v) / (1+dv/v) (1-dv/v)$$

$$1+dt/t = (1+dl/l-dv/v-dldv/lv) / (1-dv^2/v^2)$$

Neglect now higher order (in “d”) terms since (these are exceedingly small) differential expression are involved. This leads (in the approximation for sufficiently small variations) to:

$$1+dt/t = (1+dl/l-dv/v) / (1)$$

$$1+dt/t = 1+dl/l-dv/v$$

$$dt/t = (1+dl/l-dv/v)-1$$

and finally to:

$$dt/t = dl/l - dv/v$$

Appendix 2.2 (Derivation for dv/v)

From

$$v = \sqrt{(E/\rho)}$$

Valid for axial-radial polarized waves in long wavelength (much larger as diameter) approximation can be derived (for that case) that for constant E as assumed here (neglecting variations of E due to external stress):

$$(v + dv)/v = \sqrt{(E/(\rho + d\rho))} / \sqrt{(E/\rho)} = \sqrt{(\rho/(\rho + d\rho))}$$

$$1 + dv/v = \sqrt{(1/(1 + d\rho/\rho))} = 1/\sqrt{(1 + d\rho/\rho)}$$

Appendices

$$\text{and } dv/v = [1/\sqrt{(1 + dp/\rho)}] - 1$$

Appendix 2.3 (Derivation for dt/t)

For further analysis a simplification is useful (hopefully?): As we already have the equation

$$dt_{of}/t_{of} = dl/l + 1 - 1 / \sqrt{(1 + (2v - 1) dl/l)}$$

Where we can write the term,

$$1 / \sqrt{(1 + (2v - 1) dl/l)} = 1 / \sqrt{(1 + 2(v - 0.5) dl/l + (v - 0.5)^2 (dl/l)^2)}$$

is approximately valid since only higher order term has been added (which has almost no addition numerically so to speak). Now, since the root is solvable:

$$1 / \sqrt{(1 + (2v - 1) dl/l)} = 1 / (1 + (v - 0.5) dl/l)$$

and with this approximation, (hopefully?) valid for small enough second order terms:

$$\begin{aligned} dt_{of}/t_{of} &= dl/l + 1 - 1 / (1 + (v - 1/2) dl/l) \\ &= (dl/l + 1) - [1 / (1 + (v - 1/2) dl/l)] \\ &= \{(dl/l + 1) (1 + (v - 1/2) dl/l) - 1\} / (1 + (v - 1/2) dl/l) \end{aligned}$$

with higher order terms neglected:

$$= \{dl/l + 1 + (v - 1/2) dl/l - 1\} / (1 + (v - 1/2) dl/l)$$

Multiply the top and bottom with $(1 - (v - 1/2) dl/l)$

$$\begin{aligned} &= \{dl/l + 1 + (v - 1/2) dl/l - 1\} (1 - (v - 1/2) dl/l) / \text{next line} \\ &(1 + (v - 1/2) dl/l) (1 - (v - 1/2) dl/l) \end{aligned}$$

again with higher order terms neglected:

$$\begin{aligned} &= \{dl/l + 1 + (v - 1/2) dl/l - 1\} (1 - (v - 1/2) dl/l) / 1 \\ &= \{dl/l + 1 + (v - 1/2) dl/l - 1\} (1 - (v - 1/2) dl/l) \end{aligned}$$

And finally (for higher order terms neglected, which is equivalent to: “for small enough dl/l”, which is indeed realistic for any practical case):

$$\begin{aligned} &= (dl/l - 0) + (1 - (v - 1/2) dl/l) + ((v - 1/2) dl/l - 0) - 1 + (v - 1/2) dl/l \\ &= dl/l + 1 - (v - 1/2) dl/l + (v - 1/2) dl/l - 1 + (v - 1/2) dl/l \\ &= dl/l + (v - 1/2) dl/l \end{aligned}$$

So in respect for time-of-flight:

$$dt_{of}/t_{of} = dl/l + (v - 1/2) dl/l$$

$$dt_{of}/t_{of} = (1/2 + v) dl/l$$

Or

$$dt_{of}/t_{of} = 0.5 dl/l + v dl/l$$

Appendix 3.1 (Differential wave equation and its solution)

Wave equation

The equation of motion [according to Kittel book: Introduction to solid state physics] of total force F_n applied on mass m_n for any system is equal to the amount of displacement caused. So the general equation of force would be

$$F_n = C \cdot (y_{n+1} + y_{n-1} - 2y_n) \quad (1)$$

Here C is the force constant as according to Hooks law (equation). Also y_{n+1} , y_{n-1} , and y_n are the relative displacements at positions $n+1$, $n-1$ and n respectively.

The force F_n can be represented by Newton's 2nd law of motion. So

$$F_n = m \cdot a \quad (2)$$

Where m is the mass and a is the acceleration. As acceleration can be written as the 2nd derivative of displacement y as following

$$F_n = m \cdot d^2 y_n / dt^2 \quad (3)$$

$$m \cdot d^2 y_n / dt^2 = C \cdot (y_{n+1} + y_{n-1} - 2y_n) \quad (4)$$

$$d^2 y_n / dt^2 = C/m \cdot (y_{n+1} + y_{n-1} - 2y_n) \quad (5)$$

$$d^2 y_n / dt^2 - C/m \cdot (y_{n+1} + y_{n-1} - 2y_n) = 0 \quad (6)$$

This is a second order differential equation.

Solution of the wave equation

We can have a time dependent solution of y_n with $\exp(-i\omega t)$. Such that

$$d^2 y_n / dt^2 = -\omega^2 y_n \quad (7)$$

Also for any (longitudinal or transversal) displacement y , the solution of this travelling wave would be of the form

$$y_{(n\pm 1)} = y \cdot \exp\{i(n\pm 1)ka\} \quad (8)$$

where k is the wave vector and a is the spacing between the planes. Using equations (7) and (8) in eq. (5), we get

$$-\omega^2 \cdot \{y \cdot \exp(inka)\} = C/m \cdot [y \cdot \exp\{i(n+1)ka\} + y \cdot \exp\{i(n-1)ka\} - 2y \cdot \exp\{i(n)ka\}]$$

$$-\omega^2 = C/m \cdot [\exp\{(+i)ka\} + \exp\{(-i)ka\} - 2]$$

$$-\omega^2 = C/m \cdot [\exp(ika) + \exp(-ika) - 2] \quad (9)$$

As we know from exponential identity

$$\exp(ib) + \exp(-ib) = 2\cos(b)$$

Then the equation (9) can be written as

$$-\omega^2 = C/m \cdot [2\cos(ka) - 2]$$

$$\omega^2 = 2 C/m \cdot [1 - \cos(ka)] \tag{10}$$

Also known from cosines' identity

$$1 - \cos(b) = 2\sin^2(b/2)$$

Then the equation (10) becomes

$$\begin{aligned} \omega^2 &= 4 C/m \cdot \{\sin^2(ka/2)\} \\ \omega &= 2 \cdot (C/m)^{1/2} \cdot \sin(ka/2) \end{aligned} \tag{11}$$

This is the solution (equation 11) and achieved dispersion relation for three atoms system. Here ω is the angular frequency of the system.

Appendix 3.2 (Differential wave equation and its solution for transverse vibrations)

Wave equation

The equation of motion of total force applied on mass m_n for this system is equal to the restoring rotating force (torque). So the general equation of rotational force would be

$$\begin{aligned} \rightarrow & \rightarrow \\ a \times F &= -G \cdot \alpha \end{aligned}$$

As the force vector is perpendicular to the force-arm, so we can write it in scalar multiplication form as

$$F \cdot a = -G \cdot \alpha \tag{12}$$

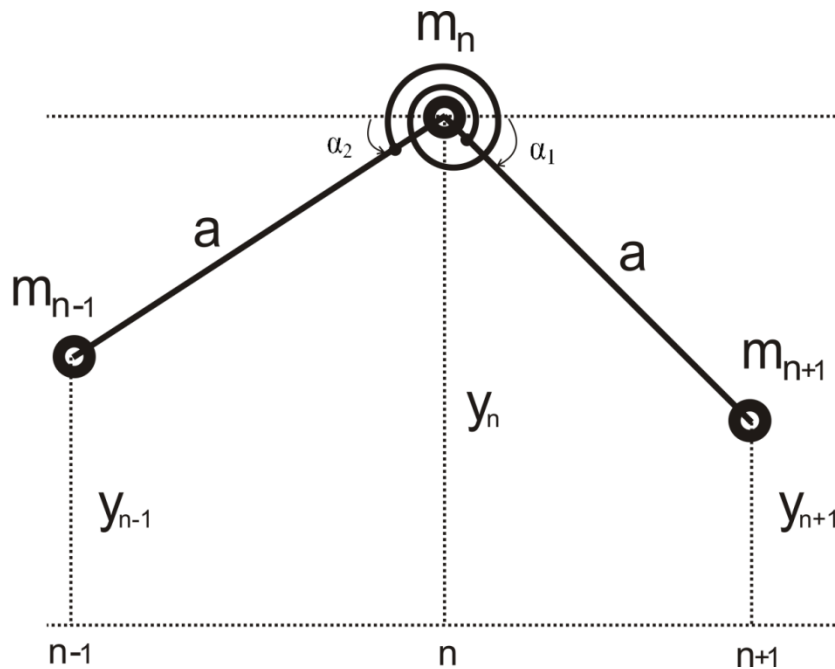


Figure 1: Mass spring coupling system for transversal or T-mode vibrations

Here G is the rotational stiffness, a is the length of rotating force arm and α is the total angle of deflection. Now for our case, this equation will be

$$F \cdot a = -G \cdot (\alpha_1 + \alpha_2) \quad (13)$$

$$F \cdot a = -G \cdot \{ (y_n - y_{n+1}) / a + (y_n - y_{n-1}) / a \}$$

Here

$$\alpha_1 = (y_n - y_{n+1}) / a \quad \text{and} \quad \alpha_2 = (y_n - y_{n-1}) / a$$

The reason is, we are taking small amplitude approximations, and for small angles

$$\sin(\alpha) \sim \alpha$$

$$F \cdot a = -G/a \cdot (y_n - y_{n+1} + y_n - y_{n-1})$$

$$F = G/a^2 \cdot (y_{n+1} + y_{n-1} - 2y_n) \quad (14)$$

Here force F is the linear component which can be represented by Newton's 2nd law of motion. Thus

$$m \cdot d^2 y_n / dt^2 = G/a^2 \cdot (y_{n+1} + y_{n-1} - 2y_n)$$

$$d^2 y_n / dt^2 = G/ma^2 \cdot (y_{n+1} + y_{n-1} - 2y_n) \quad (15)$$

$$d^2 y_n / dt^2 - G/ma^2 \cdot (y_{n+1} + y_{n-1} - 2y_n) = 0 \quad (16)$$

This is the required wave equation (equation 16) for our above elaborated case, which is a second order differential equation.

Solution of the wave equation

We can have a time dependent solution of y_n with $\exp(-i\omega t)$. Such that

$$d^2 y_n / dt^2 = -\omega^2 y_n \quad (17)$$

Also for a transversal displacement y , the solution of this travelling wave is of the form

$$y_{(n\pm 1)} = y \cdot \exp\{i(n\pm 1)ka\} \quad (18)$$

where k is the wave vector. Using equations (17) and (18) in eq. (15), we get

$$-\omega^2 \cdot \{y \cdot \exp(inka)\} = G/ma^2 \cdot [y \cdot \exp\{i(n+1)ka\} + y \cdot \exp\{i(n-1)ka\} - 2y \cdot \exp\{i(n)ka\}]$$

$$-\omega^2 = G/ma^2 \cdot [\exp\{(+i)ka\} + \exp\{(-i)ka\} - 2]$$

$$-\omega^2 = G/ma^2 \cdot [\exp(ika) + \exp(-ika) - 2] \quad (19)$$

As we know from exponential identity

$$\exp(ib) + \exp(-ib) = 2\cos(b)$$

Then the equation (8) can be written as

$$-\omega^2 = G / ma^2 \cdot [2\cos(ka) - 2]$$

$$\omega^2 = 2 G / ma^2 \cdot [1 - \cos(ka)] \quad (20)$$

Also known from cosines' identity

$$1 - \cos(b) = 2\sin^2(b/2)$$

Then the equation (9) becomes

$$\begin{aligned} \omega^2 &= 4 G/ma^2 \cdot \{\sin^2(ka/2)\} \\ \omega &= (2/a) \cdot (G/m)^{1/2} \cdot \sin(ka/2) \end{aligned} \quad (21)$$

This is the required dispersion relation (equation 21) for transversal mode. As G and m are assumed as constant values. Then the variable parameter here is a.

Appendix 3.3 (Transversely polarized lattice displacement function a_F)

For the determination of force dependent transversal displacement function, we treat only one side (as the angle's variation happens to be the same on both sides due to extensional stress) of this mass spring model which includes masses m_n and m_{n+1} . The following figure provides further explanation:

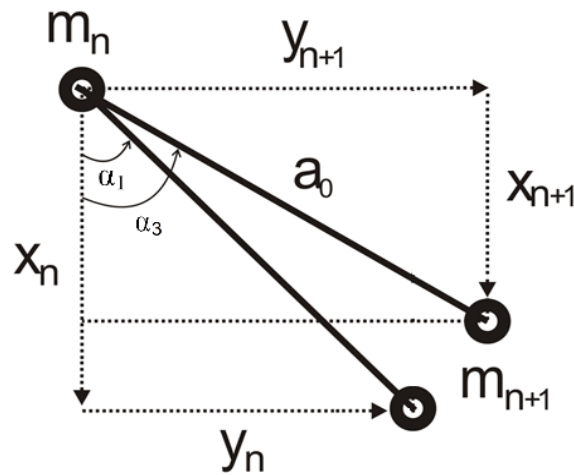


Figure 2: Single sided view of (figure 10, chapter 3) T-mode mass spring coupling system.

The deflection angle α_1 will increase from its previous position to α_3 due to external pull. The following will hold for the angles:

$$\alpha_3 \geq \alpha_1$$

With the definition of $\Delta\alpha$ being the increase (of angle) due external pull:

$$\Delta\alpha = \alpha_3 - \alpha_1$$

One can derive the effective transversal displacement function due to extensional force (from the above given figure) as following:

$$a_F = a_0 \cdot \cos(\alpha_3) \quad (22)$$

This is our required transversely polarized lattice displacement function (equation 22) depending on external pulling force.

Appendix 3.4 (Differential wave equation and its solution)

Wave equation

The equation of motion of total force F_n applied on mass m_n for any system is equal to the amount of displacement caused. So the general equation of force would be

$$F_n = C \cdot (y_{n+1} + y_{n-1} - 2y_n) \quad (23)$$

Here C is the force constant. Also y_{n+1} , y_{n-1} , and y_n are the relative displacements at positions $n+1$, $n-1$ and n respectively.

Now in our case the force constant is a generalized function equal to $[(G/a + F) / (a)]$ having lateral and transversal components. So equation (23) can be written as

$$F_n = [(G/a + F) / (a)] \cdot (y_{n+1} + y_{n-1} - 2y_n) \quad (24)$$

Here the force F_n can be represented by Newton's 2nd law of motion. So

$$F_n = m \cdot a \quad (25)$$

Where m is the mass and a is the acceleration. As acceleration can be written as the 2nd derivative of displacement y as following

$$F_n = m \cdot d^2y_n/dt^2 \quad (26)$$

Using the values of equation (26) in equation (24), we get

$$m \cdot d^2y_n/dt^2 = [(G/a + F) / (a)] \cdot (y_{n+1} + y_{n-1} - 2y_n) \quad (27)$$

$$d^2y_n/dt^2 - [(G/a + F) / (ma)] \cdot (y_{n+1} + y_{n-1} - 2y_n) = 0 \quad (28)$$

This is a second order differential equation (28).

Solution of the wave equation

We can have a time dependent solution of y_n with $\exp(-i\omega t)$. Such that

$$d^2y_n/dt^2 = -\omega^2 y_n \quad (29)$$

Also for any displacement y , the solution of this travelling wave would be of the form

$$y_{(n\pm 1)} = y \cdot \exp\{i(n\pm 1)ka\} \quad (30)$$

where k is the wave vector and a is the spacing between the planes. Using equations (29) and (30) in eq. (27), we get

$$-\omega^2 \cdot \{y \cdot \exp(inka)\} = [(G/a + F) / (ma)] \cdot [y \cdot \exp\{i(n+1)ka\} + y \cdot \exp\{i(n-1)ka\} - 2y \cdot \exp\{i(n)ka\}]$$

$$-\omega^2 = [(G/a + F) / (ma)] \cdot [\exp\{(+i)ka\} + \exp\{(-i)ka\} - 2]$$

$$-\omega^2 = [(G/a + F) / (ma)] \cdot [\exp(ika) + \exp(-ika) - 2] \quad (31)$$

As we know from exponential identity

$$\exp(ib) + \exp(-ib) = 2\cos(b)$$

Then the equation (31) can be written as

$$\begin{aligned} -\omega^2 &= [(G/a + F) / (ma)] \cdot [2\cos(ka) - 2] \\ \omega^2 &= 2 [(G/a + F) / (ma)] \cdot [1 - \cos(ka)] \end{aligned} \quad (32)$$

Also known from cosines' identity

$$1 - \cos(b) = 2\sin^2(b/2)$$

Then the equation (32) becomes

$$\omega^2 = 4 [(G/a + F) / (ma)] \cdot \{\sin^2(ka/2)\} \quad (33)$$

$$\omega = 2 \cdot [(G/a + F) / (ma)]^{1/2} \cdot \sin(ka/2) \quad (34)$$

This is the solution (equation 34) and achieved dispersion relation for three atoms system. Here ω is the angular frequency of the system.

Appendix 4.1

According to the Lennard-Jones formula, the interatomic binding potential $U_{LJ}(a)$ can be defined as following:

$$U_{LJ}(a) = 4\epsilon \cdot \left\{ \left(\frac{\sigma_{Al}}{a} \right)^{12} - \left(\frac{\sigma_{Al}}{a} \right)^6 \right\} \quad (1)$$

Differentiating equation (1) with respect to displacement 'a' will give us:

$$\begin{aligned} \frac{d}{da} [U_{LJ}(a)] &= \frac{d}{da} \left[4\epsilon \cdot \left\{ \left(\frac{\sigma_{Al}}{a} \right)^{12} - \left(\frac{\sigma_{Al}}{a} \right)^6 \right\} \right] \\ \frac{d}{da} [U_{LJ}(a)] &= 24\epsilon \cdot \left[2 \cdot \frac{(\sigma_{Al})^{12}}{(a)^{13}} - \frac{(\sigma_{Al})^6}{(a)^7} \right] \end{aligned}$$

As we know the derivative of potential is equal to force $F_{LJ}(a)$, then the above equation can be written as:

$$F_{LJ}(a) = 24\epsilon \cdot \left[2 \cdot \frac{(\sigma_{Al})^{12}}{(a)^{13}} - \frac{(\sigma_{Al})^6}{(a)^7} \right] \quad (2)$$

Further differentiating the force $F_{LJ}(a)$ will result in the following equation:

$$\frac{d}{da} [F_{LJ}(a)] = \frac{d}{da} \left[24\epsilon \cdot \left\{ 2 \cdot \frac{(\sigma_{Al})^{12}}{(a)^{13}} - \frac{(\sigma_{Al})^6}{(a)^7} \right\} \right]$$

$$\frac{d}{da} [F_{LJ}(a)] = 288\epsilon \cdot \left[2 \cdot \frac{(\sigma_{Al})^{12}}{(a)^{14}} - \frac{(\sigma_{Al})^6}{(a)^8} \right]$$

The derivative of this nonlinear variable force is represented here by $C_{LJ}(a)$,

$$C_{LJ}(a) = 288\epsilon \cdot \left[2 \cdot \frac{(\sigma_{Al})^{12}}{(a)^{14}} - \frac{(\sigma_{Al})^6}{(a)^8} \right] \quad (3)$$

This is the nonlinear interatomic force coefficient (simulating the spring constant in the mass-spring lattice model) acting within the lattice and has been derived from Lennard-Jones binding potential directly.

Appendix 4.2

If the equation of phase velocity v_{ph} is

$$v_{ph} = \omega \sqrt{\frac{2EI}{\sqrt{T^2 + 4(m) \cdot (EI) \cdot \omega^2} - T}} \quad (4)$$

As we know the phase velocity v_{ph} can also be written as

$$v_{ph} = \frac{\omega}{k} \quad (5)$$

So the above definition (equation 5) can be used (in equation 4) as following

$$\frac{\omega}{k} = \omega \sqrt{\frac{2EI}{\sqrt{T^2 + 4(m) \cdot (EI) \cdot \omega^2} - T}}$$

Here ω is the angular frequency and k is the wave number. So by squaring on both sides of the above equation

$$\left(\frac{\omega}{k}\right)^2 = (\omega)^2 \cdot \left\{ \frac{2EI}{\sqrt{T^2 + 4(m) \cdot (EI) \cdot \omega^2} - T} \right\}$$

$$\left(\sqrt{T^2 + 4(m) \cdot (EI) \cdot \omega^2} - T\right) = 2EI \cdot (k)^2$$

$$\sqrt{T^2 + 4(m) \cdot (EI) \cdot \omega^2} = T + 2EI \cdot (k)^2$$

Squaring on sides of the above equation again will give us

$$T^2 + 4(m) \cdot (EI) \cdot \omega^2 = T^2 + 4 \cdot (EI)^2 \cdot (k)^4 + 4T \cdot (EI) \cdot (k)^2$$

$$4(m) \cdot (EI) \cdot \omega^2 = 4 \cdot (EI)^2 \cdot (k)^4 + 4T \cdot (EI) \cdot (k)^2$$

$$(m) \cdot \omega^2 = (EI) \cdot (k)^4 + T \cdot (k)^2$$

$$\omega^2 = \frac{(EI) \cdot (k)^4 + T \cdot (k)^2}{(m)}$$

$$\omega^2 = \frac{T \cdot (k)^2 + (EI) \cdot (k)^4}{(m)}$$

$$\omega = \sqrt{\frac{T \cdot (k)^2 + (EI) \cdot (k)^4}{(m)}}$$

Or

$$\omega = \sqrt{\frac{Tk^2 + EIk^4}{m}} \quad (6)$$

This equation (6) is the angular frequency for (literature derived) continuum model.

Appendix 4.3

The angular frequency equation obtained after the implementation of the first three elements of suitable Taylor series is,

$$\omega = \sqrt{\frac{(2Pa + 6G) - (2Pa + 8G) \left\{ 1 - \frac{(ka)^2}{2} + \frac{(ka)^4}{24} \right\} + 2G \left\{ 1 - \frac{(2ka)^2}{2} + \frac{(2ka)^4}{24} \right\}}{ma^2}}$$

$$\omega = \sqrt{\frac{(2Pa + 6G) - (2Pa + 8G) \left\{ 1 - \frac{(ka)^2}{2} + \frac{(ka)^4}{24} \right\} + 2G \left\{ 1 - \frac{(2ka)^2}{2} + \frac{(2ka)^4}{24} \right\}}{ma^2}}$$

$$\omega = \sqrt{\frac{(2Pa + 6G) - (2Pa + 8G) + (2Pa + 8G)\frac{(ka)^2}{2} - (2Pa + 8G)\frac{(ka)^4}{24} + 2G - 8G\frac{(ka)^2}{2} + 4G\frac{(ka)^4}{3}}{ma^2}}$$

$$\omega = \sqrt{\frac{Pa(ka)^2 + 4G(ka)^2 - Pa\frac{(ka)^4}{12} - G\frac{(ka)^4}{3} - 4G(ka)^2 + 4G\frac{(ka)^4}{3}}{ma^2}}$$

$$\omega = \sqrt{\frac{Pa(ka)^2 - Pa\frac{(ka)^4}{12} + \left\{4G\frac{(ka)^4}{3} - G\frac{(ka)^4}{3}\right\}}{ma^2}}$$

$$\omega = \sqrt{\frac{Pa(ka)^2 - Pa\frac{(ka)^4}{12} + G(ka)^4}{ma^2}}$$

$$\omega = \sqrt{\frac{\left(Pk^2 - \frac{Pa^2}{12}k^4 + Gak^4\right)a^3}{ma^2}}$$

$$\omega = \sqrt{\frac{\left(Pk^2 - \frac{Pa^2}{12}k^4 + Gak^4\right)}{m/a}}$$

$$\omega = \sqrt{\frac{Pk^2 + \left(Ga - \frac{Pa^2}{12}\right)k^4}{m/a}}$$

(7)

This equation (7) is the angular frequency for (linear chain) discrete model.

Appendix 4.4

The comparison for both (models) frequency equations is done by equating them

$$\sqrt{\frac{Pk^2 + EI k^4}{m/a}} = \sqrt{\frac{Pk^2 + \left(Ga - \frac{Pa^2}{12}\right) k^4}{m/a}}$$

Squaring and solving on both sides of the above equation,

$$\frac{Pk^2 + EI k^4}{m/a} = \frac{Pk^2 + \left(Ga - \frac{Pa^2}{12}\right) k^4}{m/a}$$

$$Pk^2 + EI k^4 = Pk^2 + \left(Ga - \frac{Pa^2}{12}\right) k^4$$

$$EI k^4 = \left(Ga - \frac{Pa^2}{12}\right) k^4$$

$$EI = Ga - \frac{Pa^2}{12} \tag{8}$$

The equation (8) provides us elasticity modulus in terms of P, G and a.

Appendix 4.5

Here the group velocity by equation is

$$v_{gr} = \frac{d\omega}{dk} = \frac{d}{dk} \left\{ \sqrt{\frac{Pk^2 + EI k^4}{(m/a)}} \right\}$$

$$v_{gr} = \frac{d}{dk} \left\{ \left(\frac{Pk^2 + EI k^4}{(m/a)} \right)^{1/2} \right\}$$

$$v_{gr} = \frac{1}{2} \cdot \left\{ \left(\frac{Pk^2 + EI k^4}{(m/a)} \right)^{(1/2)-1} \right\} \cdot \frac{d}{dk} \left\{ \frac{Pk^2 + EI k^4}{(m/a)} \right\}$$

$$v_{gr} = \frac{1}{2} \cdot \left\{ \left(\frac{Pk^2 + EI k^4}{(m/a)} \right)^{-1/2} \right\} \cdot \frac{d}{dk} \left\{ \frac{Pk^2}{(m/a)} + \frac{EI k^4}{(m/a)} \right\}$$

$$v_{gr} = \frac{1}{2} \cdot \left\{ \left(\frac{Pk^2 + EI k^4}{(m/a)} \right)^{-1/2} \right\} \cdot \left\{ \frac{2kP}{(m/a)} + \frac{4k^3 EI}{(m/a)} \right\}$$

$$v_{gr} = \frac{2k}{2(m/a)} \cdot \left\{ \left(\frac{Pk^2 + EI k^4}{(m/a)} \right)^{-1/2} \right\} \cdot \{P + 2EI k^2\}$$

$$v_{gr} = \frac{k}{(m/a)} \cdot \left\{ \left(\frac{Pk^2 + EI k^4}{(m/a)} \right)^{-1/2} \right\} \cdot \{P + 2EI k^2\}$$

$$v_{gr} = \frac{k}{(m/a)} \cdot \left\{ \sqrt{\frac{(m/a)}{Pk^2 + EI k^4}} \right\} \cdot \{P + 2EI k^2\}$$

$$v_{gr} = \frac{1}{(m/a)} \cdot \left\{ \sqrt{\frac{k^2 \cdot (m/a)}{Pk^2 + EI k^4}} \right\} \cdot \{P + 2EI k^2\}$$

$$v_{gr} = \frac{1}{(m/a)} \cdot \left\{ \sqrt{\frac{k^2 \cdot (m/a)}{k^2 \cdot (P + EI k^2)}} \right\} \cdot \{P + 2EI k^2\}$$

$$v_{gr} = \left\{ \sqrt{\frac{(m/a)}{(m/a)^2 \cdot (P + EI k^2)}} \right\} \cdot \{P + 2EI k^2\}$$

$$v_{gr} = \left\{ \sqrt{\frac{1}{(m/a) \cdot (P + EI k^2)}} \right\} \cdot \{P + 2EI k^2\}$$

(9)

Appendix 4.6

Here the group velocity by equation is

$$v_{gr} = \frac{d\omega}{dk} = \frac{d}{dk} \left\{ \sqrt{\frac{Pk^2 + \left(Ga - \frac{Pa^2}{12}\right)k^4}{(m/a)}} \right\}$$

$$v_{gr} = \frac{d}{dk} \left\{ \sqrt{\frac{Pk^2 + \left(Ga - \frac{Pa^2}{12}\right)k^4}{(m/a)}} \right\}$$

$$v_{gr} = \frac{d}{dk} \left\{ \left(\frac{Pk^2 + \left(Ga - \frac{Pa^2}{12}\right)k^4}{(m/a)} \right)^{1/2} \right\}$$

$$v_{gr} = \frac{1}{2} \cdot \left\{ \left(\frac{Pk^2 + \left(Ga - \frac{Pa^2}{12}\right)k^4}{(m/a)} \right)^{(1/2)-1} \right\} \cdot \frac{d}{dk} \left\{ \frac{Pk^2 + \left(Ga - \frac{Pa^2}{12}\right)k^4}{(m/a)} \right\}$$

$$v_{gr} = \frac{1}{2} \cdot \left\{ \left(\frac{Pk^2 + \left(Ga - \frac{Pa^2}{12}\right)k^4}{(m/a)} \right)^{-(1/2)} \right\} \cdot \frac{d}{dk} \left\{ \frac{Pk^2}{(m/a)} + \frac{\left(Ga - \frac{Pa^2}{12}\right)k^4}{(m/a)} \right\}$$

$$v_{gr} = \frac{1}{2} \cdot \left\{ \frac{\left(Pk^2 + \left(Ga - \frac{Pa^2}{12} \right) k^4 \right)^{-(1/2)}}{(m/a)} \right\} \cdot \left\{ \frac{2kP}{(m/a)} + \frac{4 \left(Ga - \frac{Pa^2}{12} \right) k^3}{(m/a)} \right\}$$

$$v_{gr} = \frac{1}{2} \cdot \left\{ \frac{\left(Pk^2 + \left(Ga - \frac{Pa^2}{12} \right) k^4 \right)^{-(1/2)}}{(m/a)} \right\} \cdot \frac{2k}{(m/a)} \cdot \left\{ P + 2 \left(Ga - \frac{Pa^2}{12} \right) k^2 \right\}$$

$$v_{gr} = \frac{2k}{2(m/a)} \cdot \left\{ \frac{\left(Pk^2 + \left(Ga - \frac{Pa^2}{12} \right) k^4 \right)^{-(1/2)}}{(m/a)} \right\} \cdot \left\{ P + 2 \left(Ga - \frac{Pa^2}{12} \right) k^2 \right\}$$

$$v_{gr} = \frac{k}{(m/a)} \cdot \left\{ \frac{\sqrt{(m/a)}}{\sqrt{Pk^2 + \left(Ga - \frac{Pa^2}{12} \right) k^4}} \right\} \cdot \left\{ P + 2 \left(Ga - \frac{Pa^2}{12} \right) k^2 \right\}$$

$$v_{gr} = \frac{1}{(m/a)} \cdot \left\{ \frac{\sqrt{k^2 \cdot (m/a)}}{\sqrt{Pk^2 + \left(Ga - \frac{Pa^2}{12} \right) k^4}} \right\} \cdot \left\{ P + 2 \left(Ga - \frac{Pa^2}{12} \right) k^2 \right\}$$

$$v_{gr} = \frac{1}{(m/a)} \cdot \left\{ \frac{\sqrt{k^2 \cdot (m/a)}}{\sqrt{k^2 \cdot \left\{ P + \left(Ga - \frac{Pa^2}{12} \right) k^2 \right\}}} \right\} \cdot \left\{ P + 2 \left(Ga - \frac{Pa^2}{12} \right) k^2 \right\}$$

$$v_{gr} = \frac{1}{(m/a)} \cdot \left\{ \frac{\sqrt{\frac{(m/a)}{\left\{ P + \left(Ga - \frac{Pa^2}{12} \right) k^2 \right\}}}}{\left\{ P + 2 \left(Ga - \frac{Pa^2}{12} \right) k^2 \right\}} \right\}$$

$$v_{gr} = \left\{ \frac{\sqrt{\frac{(m/a)}{\left\{ (m/a)^2 \cdot \left\{ P + \left(Ga - \frac{Pa^2}{12} \right) k^2 \right\} \right\}}}}{\left\{ P + 2 \left(Ga - \frac{Pa^2}{12} \right) k^2 \right\}} \right\}$$

$$v_{gr} = \left\{ \frac{\sqrt{\frac{1}{\left\{ (m/a) \cdot \left\{ P + \left(Ga - \frac{Pa^2}{12} \right) k^2 \right\} \right\}}}}{\left\{ P + 2 \left(Ga - \frac{Pa^2}{12} \right) k^2 \right\}} \right\} \tag{10}$$

Appendix 4.7 (Viscoelastic case)

One of the basic viscoelastic models, namely Kelvin-Voigt viscoelastic model has been chosen here to represent the basic viscoelastic effects present in the material including extensional stress.

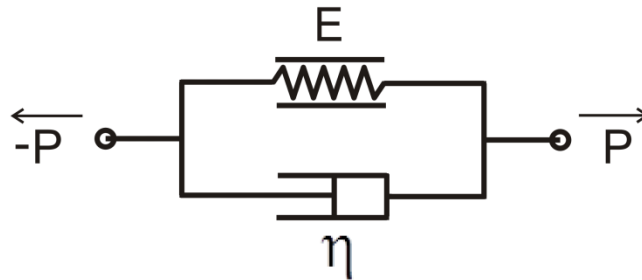


Figure 1: Schematic diagram of Kelvin–Voigt model

The Kelvin-Voigt model is given priority over Maxwell’s model due to its better explanation (i.e. asymptotic) of creep behaviour in the material due to extensional stress. The standard equation for this model is

$$\sigma(t) = E\varepsilon(t) + \eta \frac{d\varepsilon(t)}{dt} \quad (11)$$

Where E is the modulus of elasticity (young's modulus), σ the applied stress, ε resultant strain in the material, depending on time t , and η is the viscosity factor.

For the condition applied in our case, a constantly applied stress σ_0 , the differential equation (11) can be solved for total strain as following

$$\frac{\sigma_0}{\eta} = \frac{E}{\eta} \varepsilon(t) + \frac{d\varepsilon(t)}{dt}$$

$$\frac{d\varepsilon(t)}{dt} = \frac{\sigma_0}{\eta} - \frac{E}{\eta} \varepsilon(t) \quad (12)$$

By applying integration on this above equation (12), will provide us

$$\varepsilon(t) = \frac{\sigma_0}{E} + C_1 e^{-\frac{E}{\eta}t} \quad (13)$$

Here C_1 is the constant of integration and can be found by using initial condition in which the stress is happening instantaneously i.e. $t = 0$ in equation (13). The strain $\varepsilon(t)$ in this case will also be zero because there was no strain in the material at the start. So

$$0 = \frac{\sigma_0}{E} + C_1 e^0$$

As we know the value of $e^0 = 1$, then

$$C_1 = -\frac{\sigma_0}{E} \quad (14)$$

Using the above value (equation 14) of C_1 in equation (13), the total strain would be

$$\varepsilon(t) = \frac{\sigma_0}{E} - \frac{\sigma_0}{E} e^{-\frac{E}{\eta}t}$$

$$\varepsilon(t) = \frac{\sigma_0}{E} \left(1 - e^{-\frac{E}{\eta}t} \right) \quad (15)$$

The exponential term in equation (15) can be solved by using Maclaurin series as following

$$e^x = 1 + x + \frac{x^2}{2!} + \frac{x^3}{3!} \quad \text{and so on} \quad \text{for all } x$$

We will only use first two terms of the above series as the value of each increasing term has a very minimum effect on the overall result of the series. So in our case the following equation can be used

$$e^x = 1 + x \tag{16}$$

Using the definition of equation (16) in equation (15), we will get

$$\varepsilon(t) = \frac{\sigma_0}{E} \left\{ 1 - \left(1 - \frac{E}{\eta} t \right) \right\}$$
$$\varepsilon(t) = \frac{\sigma_0}{\eta} t \tag{17}$$

In terms of stress σ_0 , the equation (17) can be written as

$$\sigma_0 = \frac{\eta}{t} \varepsilon(t) \tag{18}$$

The stress equation (18) deduced from Kelvin-Voigt model can represent a simple viscoelastic case (in which the Hooke's springs and dampers are connected in parallel representing the viscoelasticity of the material), where the extensional pulling force P can be written as

$$P = \sigma_0 = \frac{\eta}{t} \varepsilon(t) \tag{19}$$

Here $\varepsilon(t)$ is the strain in the material, depending on time t, and if we exclude in our following notation the (time dependence) sign t in equation (19), the extensional stress P can be denoted as

$$P = \frac{\eta}{t} \varepsilon \quad (20)$$

Where η is the viscosity factor, and t is the time. Here the function $\frac{\eta}{t}$ is equivalent to E in the Hooke's definition of linear elasticity.

Appendix 4.8

To find the frequency value at zero E_{CF} (elastic coupling function), the function can be obtained by solving the following equation:

$$E_{CF} = \frac{1}{\left[\frac{L.P}{a_0 \cdot d} \right]} \cdot [TOF] \quad (21)$$

All of the symbols including the TOF are defined in the fourth chapter text (see 4.3 Analytical treatment). As according to the given condition the value of E_{CF} is zero, so the above equation (21) can be written as:

$$0 = \frac{1}{\left[\frac{L.P}{a_0 \cdot d} \right]} \cdot [TOF]$$

This means

$$0 = [TOF]$$

Equating the TOF (i.e. equation 74 in chapter 4) equals to zero. The following equation will arise:

$$0 = \frac{\sqrt{ma^2}}{[(Pa + 4G) \cdot \sin(ka) - 2G \cdot \sin(2ka)]} \left[\sqrt{(2Pa + 6G) - (2Pa + 8G) \cdot \cos(ka) + 2G \cdot \cos(2ka)} \right]$$

$$0 = \left[\sqrt{(2Pa + 6G) - (2Pa + 8G) \cdot \cos(ka) + 2G \cdot \cos(2ka)} \right] \quad (22)$$

Squaring on both sides of equation (22), we get

$$\begin{aligned} 0 &= (2Pa + 6G) - (2Pa + 8G) \cdot \cos(ka) + 2G \cdot \cos(2ka) \\ (2Pa + 6G) - (2Pa + 8G) \cdot \cos(ka) + 2G \cdot \cos(2ka) &= 0 \end{aligned} \quad (23)$$

As according to cosine trigonometric identity,

$$\cos(2x) = 2\cos^2(x) - 1 \quad (24)$$

Using the trigonometric identity of equation (24) in equation (23), we get

$$\begin{aligned} (2Pa + 6G) - (2Pa + 8G) \cdot \cos(ka) + 2G \cdot \{2\cos^2(ka) - 1\} &= 0 \\ (2Pa + 6G) - (2Pa + 8G) \cdot \cos(ka) + 4G \cdot \cos^2(ka) - 2G &= 0 \\ (2Pa + 8G) \cdot \cos(ka) - 4G \cdot \cos^2(ka) &= (2Pa + 6G) - 2G \\ (2Pa + 8G) \cdot \cos(ka) - 4G \cdot \cos^2(ka) &= (2Pa + 4G) \end{aligned} \quad (25)$$

Using logarithmic transformations in equation (25) and by solving it, we will arrive at:

$$\ln[\operatorname{cosec}(ka)] = \ln \left[\frac{(2Pa + 4G) \cdot (4G)}{(2Pa + 8G)} \right] \quad (26)$$

Applying antilogarithm on both sides of equation (26), we get

$$\operatorname{cosec}(ka) = \left[\frac{(2Pa + 4G) \cdot (4G)}{(2Pa + 8G)} \right] \quad (27)$$

Applying $\operatorname{cosec}^{-1}$ on both sides of equation (27), we get

$$(ka) = \operatorname{cosec}^{-1} \left[\frac{(2Pa + 4G) \cdot (4G)}{(2Pa + 8G)} \right] \quad (28)$$

Also we know $\operatorname{cosec}^{-1} = \operatorname{cose}$,

Thus the equation (28) will become

$$(ka) = \operatorname{cose} \left[\frac{(2Pa + 4G) \cdot (4G)}{(2Pa + 8G)} \right] \quad (29)$$

This equation (29) gives us a zone boundary wave function (ka) in terms G, P, and a to evaluate frequency at minimum value of elastic coupling function (i.e. at zero E_{CF}).

Appendix 4.9

To find the horizontal asymptote with frequency approaching infinity, we start with the equation of elastic coupling function as following:

$$E_{CF} = \frac{1}{\left[\frac{L \cdot P}{a_0 \cdot d} \right]} \cdot [\operatorname{TOF}] \quad (30)$$

Substituting the value of TOF (equation 74, chapter 4) in the above equation (30),

$$E_{CF} = \left[\frac{L.P}{a_0.d} \right] \left[\frac{\sqrt{ma^2}}{\{(Pa + 4G).sin(ka) - 2G.sin(2ka)\}} \sqrt{\{(2Pa + 6G) - (2Pa + 8G).cos(ka) + 2G.cos(2ka)\}} \right] \quad (31)$$

Here the equation (31) can only be solved for $ka = 0 \rightarrow \infty$, if we expand the trigonometric functions by Taylor series:

$$\sin(x) = (x) - \frac{(x)^3}{3!} \quad \text{and} \quad \cos(x) = 1 - \frac{(x)^2}{2!} \quad (32)$$

The higher degrees of Taylor series are neglected due to negligible effect on the overall value of the expansion. By substituting the above equation (32) in equation (31) and by solving it, we will arrive at:

$$E_{CF} = \left[\frac{L.P}{a.d} \right] \left[\frac{\sqrt{maP}}{\left\{ P - \frac{P}{6} (ka)^2 + \frac{2G}{a} (ka)^2 \right\}} \right]$$

$$E_{CF} = \frac{1}{\left[\left\{ \frac{L.P}{a_0.d} \right\} \cdot \frac{\left\{ P - \frac{P}{6} (ka)^2 + \frac{2G}{a} (ka)^2 \right\}}{\sqrt{maP}} \right]} \quad (33)$$

The equation (33) is now in the function form of 'ka' and can also be written as following:

$$E_{CF} = \frac{1}{\text{function}(ka)} \quad (34)$$

Here the function(k a) comparing with equation (33) can be written as following:

$$\text{function}(ka) = \left\{ \frac{L.P}{a_0.d} \right\} \cdot \frac{\left\{ P - \frac{P}{6} (ka)^2 + \frac{2G}{a} (ka)^2 \right\}}{\sqrt{maP}} \quad (35)$$

We know the condition for frequency $\rightarrow \infty$ corresponds to the horizontal asymptote for which the condition of elastic coupling function will be

$$E_{CF} = 0 \quad (36)$$

Or

$$\text{function}(k a) = \infty \quad (37)$$

This means (comparing equations 35 and 37)

$$\left\{ \frac{L.P}{a_0.d} \right\} \cdot \frac{\left\{ P - \frac{P}{6}(ka)^2 + \frac{2G}{a}(ka)^2 \right\}}{\sqrt{maP}} = \infty \quad (38)$$

$$\left\{ \frac{L.P}{a_0.d} \right\} \cdot \frac{\left\{ P - \frac{P}{6}(ka)^2 + \frac{2G}{a}(ka)^2 \right\}}{\sqrt{maP}} = \frac{1}{0}$$

$$\frac{1}{\left\{ P - \frac{P}{6}(ka)^2 + \frac{2G}{a}(ka)^2 \right\}} = 0$$

$$\left\{ P - \frac{P}{6}(ka)^2 + \frac{2G}{a}(ka)^2 \right\}^{-1} = 0$$

$$\left\{ P + \frac{2G}{a}(ka)^2 - \frac{P}{6}(ka)^2 \right\}^{-1} = 0$$

$$\left[P + \left\{ \frac{2G}{a}(ka)^2 - \frac{P}{6}(ka)^2 \right\} \right]^{-1} = 0 \quad (39)$$

The equation (39) can be expanded by binomial theorem (suitable for -ve power integers) according to the following formula:

$$(a + b)^n = (a)^n \cdot (1 + b/a)^n \quad (40)$$

Where

$$n = \text{-ve integer} \quad \text{and} \quad -1 < b/a < +1$$

$$(a + b)^n = (a)^n \cdot \left\{ 1 + n(b/a) + \frac{n(n-1)}{2!} (b/a)^2 + \frac{n(n-1)(n-2)}{3!} (b/a)^3 + \dots \right\} \quad (41)$$

Here the equation (41) is an infinite series but we can limit up to first degree as $(b/a)^2$, $(b/a)^3$, $(b/a)^4$, ..., are becoming increasingly very small values as compared to rest of the series and have very negligible effect on the value of whole series. So it can be written (and shortened) as

$$(a + b)^n = (a)^n \cdot \{1 + n(b/a)\} \quad (42)$$

Thus the equation (39) can be written in the form of equation (42) as following:

$$(P)^{-1} \cdot \left[1 - \left\{ \frac{\frac{2G}{a}(ka)^2 - \frac{P}{6}(ka)^2}{P} \right\} \right] = 0 \quad (43)$$

Where $-1 < \left\{ \frac{\frac{2G}{a}(ka)^2 - \frac{P}{6}(ka)^2}{P} \right\} < +1$

By solving equation (43), we get

$$\frac{1}{P} - \frac{2G}{P^2 a} (ka)^2 - \frac{1}{6P} (ka)^2 = 0$$

By further solving the above equation, we will arrive at:

$$(ka) = \sqrt{\frac{6aP}{(12G - aP)}} \quad (44)$$

This equation (44) gives us a zone boundary wave function (ka) in terms G , P , and a related to the horizontal asymptote.

Appendix 4.10

To find the vertical asymptote with frequency approaching zero, we start with the equation of elastic coupling function as following:

$$E_{CF} = \frac{1}{\left[\frac{L.P}{a_0.d} \right]} \cdot [TOF] \quad (45)$$

By substituting the value of TOF (equation 74, in chapter 4) in the above equation (45),

$$E_{CF} = \frac{1}{\left[\frac{L.P}{a_0.d} \right]} \left[\frac{\sqrt{ma^2}}{\{(Pa + 4G).sin(ka) - 2G.sin(2ka)\} \sqrt{(2Pa + 6G) - (2Pa + 8G).cos(ka) + 2G.cos(2ka)}} \right] \quad (46)$$

Here this equation (46) can only be solved for $ka = 0 \rightarrow \infty$, if we expand the trigonometric functions by Taylor series:

$$\sin(x) = (x) - \frac{(x)^3}{3!} \quad \text{and} \quad \cos(x) = 1 - \frac{(x)^2}{2!} \quad (47)$$

The higher degrees of Taylor series are neglected due to negligible effect on the overall value of the expansion. By substituting the above equation (47) in equation (46) and by solving it, we will arrive at:

$$E_{CF} = \frac{1}{\left[\frac{L.P}{a_0.d} \right]} \cdot \left[\frac{\sqrt{maP}}{\left\{ P - \frac{P}{6} (ka)^2 + \frac{2G}{a} (ka)^2 \right\}} \right]$$

$$E_{CF} = \frac{1}{\left[\left\{ \frac{L.P}{a_0.d} \right\} \cdot \frac{\left\{ P - \frac{P}{6}(ka)^2 + \frac{2G}{a}(ka)^2 \right\}}{\sqrt{maP}} \right]} \quad (48)$$

The equation (48) is now in the function form of 'ka' and can be denoted as following:

$$E_{CF} = \frac{1}{\text{function}(ka)} \quad (49)$$

Here the function(k a) comparing with equation (48) can be written as:

$$\text{function}(ka) = \left\{ \frac{L.P}{a_0.d} \right\} \cdot \frac{\left\{ P - \frac{P}{6}(ka)^2 + \frac{2G}{a}(ka)^2 \right\}}{\sqrt{maP}} \quad (50)$$

We know the condition for frequency $\rightarrow 0$ corresponds to the vertical asymptote for which the condition of elastic coupling function will be

$$E_{CF} = \infty \quad \text{or} \quad E_{CF} = \frac{1}{0} \quad (51)$$

Also we know that

$$E_{CF} = \frac{1}{\text{function}(ka)} \quad (52)$$

This means by comparing equations (50, 51 and 52), we will get

$$\text{function}(k a) = 0 \quad (53)$$

Substituting the value of 'function(ka)' from equation (50) in equation (53), we get

$$0 = \left\{ \frac{L.P}{a_0.d} \right\} \cdot \frac{\left\{ P - \frac{P}{6}(ka)^2 + \frac{2G}{a}(ka)^2 \right\}}{\sqrt{maP}}$$

Or

$$\left\{ P - \frac{P}{6}(ka)^2 + \frac{2G}{a}(ka)^2 \right\} = 0 \tag{54}$$

Further solving the above equation (54), we will arrive at:

$$(ka) = \sqrt{\frac{P}{\left(\frac{P}{6} - \frac{2G}{a} \right)}} \tag{55}$$

This equation (55) gives us a zone boundary wave function (ka) in terms G, P, and a related to the vertical asymptote.

10. The publications and results used in the dissertation:

- [1] A differential method for the determination of the time-of-flight for ultrasound under pulsed wide band excitation including chirped signals, **K. S. Tarar**, R. Meier, E. Twerdowski, R. Wannemacher, and W. Grill, Proc. SPIE 693519, (2008)
- [2] Stress detection with guided acoustic ultrasonic waves by nonlinear elastic and geometric effects, **K. S. Tarar**, R. Meier, U. Amjad, and W. Grill, Proc. SPIE 729518, (2009)
- [3] Lumped circuit mechanical models and lattice dynamics approach to the dependence of the time-of-flight of bulk and guided acoustical modes on elongation, **K. S. Tarar**, U. Amjad, and W. Grill, Proc. SPIE 76500I, (2010)
- [4] Mode selective excitation and detection of Lamb waves, K. Hahn, U. Amjad, **K. S. Tarar**, D. Jha, and W. Grill, Proc. SPIE 76500D, (2010)
- [5] Lattice dynamics approach to determine the dependence of the time-of-flight of transversal polarized acoustic waves on external stress, **K. S. Tarar**, M. Pluta, U. Amjad, W. Grill, Proc. SPIE 79842R, (2011)
- [6] Dispersion relations and stress dependencies of acoustic waves travelling on a chain of point masses connected by linear and torsional springs, M. Pluta, U. Amjad, H. Klinghammer, D. Jha, **K. S. Tarar**, W. Grill, Acoustical Imaging, Volume 31, pp. 253-265, (2012)
- [7] Linear chain lattice dynamics approach to the dependence of the time-of-flight of acoustical modes on stress and strain, **K. S. Tarar**, M. Pluta, and W. Grill, (Article in preparation for publication)
- [8] Movable EMATs scanning and inductive testing of the slat tracks, **K. S. Tarar**, U. Amjad, and W. Grill, (Article in preparation for publication)
- [9] Progressive ablation of 5 mm thick aluminum plates using mode selective excitation and detection of ultrasonic guided waves, **K. S. Tarar**, U. Amjad, and W. Grill, (Article in preparation for publication)

Author's statement of independence

I hereby certify that I have prepared this PhD dissertation independently, and that only those sources, aids and advisors have been used / consulted which are noted down in this thesis book and / or provided in the "author statement of contributions".

Signature

Dated

Declaration for the library:

I herewith agree that a copy of this thesis book can be used by the Physics library of the University of Leipzig.

Signature

Dated

Curriculum Vitae

Personal Information

First name	Khurram Shahzad
Family name	Tarar
Nationality	Pakistani, Canadian
Date and place of birth	December 15th 1977, (Pakistan)
Contact information	Toronto, Ontario Canada
E-mail addresses	khurram@physik.uni-leipzig.de khurram_12345_pk@yahoo.com
Marital status	Married
Language skills	Fluent in English, Urdu, Punjabi, and Basic proficiency in German, Arabic

Education

1996 - 1998	Bachelor of Science (Physics, Mathematics) University of the Punjab, Lahore, Pakistan
1998 - 2000	Master of Science (Physics) University of the Punjab, Lahore, Pakistan
2000 - 2001	Post Graduate Diploma (Computer Science) Government College of Science, Lahore, Pakistan
2003 - 2006	Master of Science (Physics) University of Leipzig, Germany
2009 - Present	Candidate of Ph.D. (Physics) (Specialized in Solid State Physics and Acoustics) University of Leipzig, Germany